공학박사학위논문

A Structural Model Updating Method of Finite Element Models Enhanced by the System Reduction and Neural Networks

구조 축소 기법과 인공신경 회로망을 이용한 유한요소 구조물의 모델 갱신 기법

2020년 8월

서울대학교 대학원

기계항공공학부

성 희 준

Abstract

Model updating methods for structural systems have been introduced in various numerical processes. To improve the updating method, the process must require an accurate analysis and minimized experimental uncertainties. Finite element model was employed to describe structural system. Structural vibration behavior of a plate model is expressed as a combination of the initial state behavior of the structure and its associated perturbations. The dynamic behavior obtained from a limited number of accessible nodes and their associated degrees of freedom is employed to detect structural changes that are consistent with the perturbations. The equilibrium model is described in terms of the measured and unmeasured modal data. Unmeasured information is estimated using an iterated improved reduction scheme. Because the identification problem depends on the measured information, the quality of the measured data determines the accuracy of the identified model and the convergence of the identification problem. The accuracy of the identification depends on the measurement/sensor location. We propose a more accurate identification method using the optimal sensor location selection method. Experimental examples are adopted to examine the convergence and accuracy of the proposed method applied to an inverse problem of system identification. Model updating methods for structural systems have been introduced in various fields. Model updating processes are important for improving a model's accuracy by considering experimental data. Structural system identification was achieved here by applying the degree of freedom-based

reduction method and the inverse perturbation method. Experimental data were obtained using the specific sensor location selection method. Experimental vibration data were restored to a full finite element model using the reduction method to compare and update the numerical model. Applied iteratively, the improved reduced system method boosts model accuracy during full model restoration; however, iterative processes are time-consuming. The calculation efficiency was improved using the system equivalent reduction-expansion process in concert with the proper orthogonal decomposition. A convolutional neural network was trained and applied to the updating process. We propose the use of an efficient model updating method using a convolutional neural network to reduce calculation time. Experimental and numerical examples were adopted to examine the efficiency and accuracy of the model updating method using a convolutional neural network. A more complex model is applied for model updating method and validated with proposed methods. A bolt assembly modeling is introduced and simplified with verified methodologies.

Keywords : *Model updating method, Degree of freedom-based reduction method, System identification, Sensor location selection method, Neural networks*

Student Number : 2014-21558

Contents

List of figures

List of tables

Chapter 1.

Introduction

1.1 Frequency model updating method

Numerical analysis techniques and functions of digital computers have been greatly improved and at the same time the analysis models also have become diverse and complex. The finite element method (FEM) is used to construct a sophisticated numerical model. FEM, the most widely used method in the engineering design process, has made the numerical model more sophisticated. On the other hand, the difference in the physical identity of the computational model compared to the actual model has reduced the reliability of its own computation. To integrate a computational analysis, the difference between the computational model and the real model must be minimized, which means that the dynamic response of both models should be similar. The structural system identification method matches the calculated model with the actual model by an experimental response. The identification process has been applied to aerospace truss structures or simple beam

problems due to the appropriate conditions **[1-4]**. The truss structure or beam structure has a reasonable number of parameters to solve the identification problem. In the case of a continuum structure, however, it explains itself by dramatically increasing the number of parameters. Delicate processing of the number of parameters is important to apply structural system identification to the continuum model. The reduction methods and inverse problems **[5-10]** are applied to minimize the identification problem and reduce the number of parameters for continuum models. Improving the accuracy of the finite element model, the number of parameters increases. Therefore, by dividing the elements by a reasonable number, the accuracy of the finite element model can be maintained. While at the same time, by a reduction method based on the degrees of freedom, the number of the parameters can be decreased **[8-10]**.

Plenty of methodologies for structural system identification have been introduced and utilized **[1-4]**. As mentioned before, the usage of applied methods was limited to typical situations with comparing eigenvalues between simplified models and experiments, since structural differences appear in the change of eigenvalue and it can be traced easily **[2-4]**. In continuum model, however, structures are more complicated and have variety of mode shapes. Changes of structure brings up changes of not only eigenvalue but also eigenvector. Eigenvector comparison became more significant in structural system identification on continuum model. Eigenvector of different models have been compared with IPM (Inverse Perturbation Method) **[5-7]**. Impact vibration test has been applied to gain dynamic information of the real model. Much more delicate approach is necessary when considering eigenvector data. A variety of numerical structural system identification methods have been studied in our research group **[11-24]**.

Sensor location prediction is one of the critical skills which is necessary for this study **[24]**. By implementing the sensors on each node, every data regarding all degree of freedom can be achieved, but it is impossible in continuum models due to experimental efficiency. The solutions for the limitations will be introduced and the methodologies and experimental examples will be followed.

1.2. Reduction method

1.2.1. Degree of freedom-based reduction method

The concept of reducing matrices was first introduced by Guyan **[8]**. Eigen analysis is time-consuming, and the reduction method **[8]** can save the calculation time while retaining the accuracy of the solution. This method has been widely employed to reduce the number of DOFs in the FE method, However, problems in accuracy have been encountered in some cases. O'Callaghan **[9]** proposed an improved reduced system (IRS) method, and Friswell et al. **[10]** proposed an iterated IRS method (IIRS). An undamped mass–stiffness FE method can be decomposed into primary and secondary sets, which constitute the primary DOFs (PDOFs) and secondary DOFs (SDOFs), respectively, as

$$\begin{bmatrix} \mathbf{M}_{pp} & \mathbf{M}_{ps} \\ \mathbf{M}_{sp} & \mathbf{M}_{ss} \end{bmatrix} \begin{Bmatrix} \ddot{\mathbf{u}}_p \\ \ddot{\mathbf{u}}_s \end{Bmatrix} + \begin{bmatrix} \mathbf{K}_{pp} & \mathbf{K}_{ps} \\ \mathbf{K}_{sp} & \mathbf{K}_{ss} \end{bmatrix} \begin{Bmatrix} \mathbf{u}_p \\ \mathbf{u}_s \end{Bmatrix} = \begin{Bmatrix} \mathbf{f}_p \\ \mathbf{f}_s \end{Bmatrix}, \tag{1.1}$$

where the subscript p indicates a primary DOF and the subscript s indicates a secondary DOF for each mass $(\mathbf{M})$, stiffness $(\mathbf{K})$, and force matrix $(\mathbf{f})$. The stiffness matrix, $\mathbf{K}$, can be divided into a primary part and secondary part as in following equations:

$$\mathbf{K}_{sp}\mathbf{u}_p + \mathbf{K}_{ss}\mathbf{u}_s = 0, \tag{1.2}$$

$$\mathbf{u} = \begin{Bmatrix} \mathbf{u}_p \\ \mathbf{u}_s \end{Bmatrix} = \begin{bmatrix} \mathbf{I} \\ -\mathbf{K}_{ss}^{-1}\mathbf{K}_{sp} \end{bmatrix} \{\mathbf{u}_p\} = \begin{bmatrix} \mathbf{I} \\ \mathbf{t}_G \end{bmatrix} \{\mathbf{u}_p\} = \mathbf{T}_G\mathbf{u}_p. \tag{1.3}$$

The development of the reduction method began by using the Guyan transformation matrix $\mathbf{T}_G$ in Eq. (1.3) under the hypothesis that the influence of the dynamic term is insignificant **[8]**. If becomes zero, then the second row of Eq. (1.1) is reorganized to yield Eq. (1.2). The full displacement matrix in Eq. (1.3) may be expressed using the PDOF matrix and the corresponding parts of Matrices with only PDOFs are used in most reduction problems. However, PDOFs are applied to sensor locations, and vibrational data are gathered by locating the sensors at the nodes aligned with the PDOFs.

$$\mathbf{K}_{sp}\mathbf{u}_p + \mathbf{K}_{ss}\mathbf{u}_s - (\mathbf{M}_{sp}\ddot{\mathbf{u}}_p + \mathbf{M}_{ss}\ddot{\mathbf{u}}_s) = 0, \tag{1.4}$$

$$\mathbf{u} = \begin{Bmatrix} \mathbf{u}_p \\ \mathbf{u}_s \end{Bmatrix} = \begin{bmatrix} \mathbf{I} \\ -(\mathbf{K}_{ss} - \lambda\mathbf{M}_{ss})^{-1}(\mathbf{K}_{sp} - \lambda\mathbf{M}_{sp}) \end{bmatrix} \{\mathbf{u}_p\} = \begin{bmatrix} \mathbf{I} \\ \mathbf{t}_G \end{bmatrix} \{\mathbf{u}_p\} = \mathbf{T}_G\mathbf{u}_p. \tag{1.5}$$

$$\mathbf{t}(\lambda) = -(\mathbf{K}_{ss} - \lambda\mathbf{M}_{ss})^{-1}(\mathbf{K}_{sp} - \lambda\mathbf{M}_{sp}). \tag{1.6}$$

1.2.2. Iterated improved reduced system

Because the reduction method is constructed from a static perspective, the accuracy becomes more difficult to ensure as the frequency increases. In Eqs. (1.4) and (1.5), the mass matrix was incorporated when constructing the Guyan transformation

matrix. As the width of the application range increases, the reduction in Eq. (1.6) becomes an issue, and the need for an accurate transformation matrix construction becomes critical. Attempts have been made to construct a transformation matrix, but only up to a certain frequency range **[10]**.

$$\begin{aligned}\mathbf{t}(\lambda) = &-\mathbf{K}_{ss}^{-1}\mathbf{K}_{sp} + \mathbf{K}_{ss}^{-1}(\mathbf{M}_{sp} - \mathbf{M}_{ss}\mathbf{K}_{ss}^{-1}\mathbf{K}_{sp})\lambda \\ &+ \mathbf{K}_{ss}^{-1}\mathbf{M}_{ss}\left\{\mathbf{K}_{ss}^{-1}(\mathbf{M}_{sp} - \mathbf{M}_{ss}\mathbf{K}_{ss}^{-1}\mathbf{K}_{sp})\right\}\lambda^2 + O(\lambda^3),\end{aligned} \tag{1.7}$$

$$\mathbf{t}_{IRS} = \mathbf{t}_{IIRS}^{(1)} = -\mathbf{K}_{ss}^{-1}\mathbf{K}_{sp} + \mathbf{K}_{ss}^{-1}(\mathbf{M}_{sp} - \mathbf{M}_{ss}\mathbf{K}_{ss}^{-1}\mathbf{K}_{sp})\mathbf{M}_G^{-1}\mathbf{K}_G, \tag{1.8}$$

$$\mathbf{t}_{IIRS}^{(i)} = \mathbf{t}_G + \mathbf{K}_{ss}^{-1}\left(\mathbf{M}_{sp} + \mathbf{M}_{ss}\mathbf{t}_{IIRS}^{(i-1)}\right)\left(\mathbf{M}_{IIRS}^{(i-1)}\right)^{-1}\mathbf{K}_{IIRS}^{(i-1)}. \tag{1.9}$$

The IRS method has been proposed as a more fundamental approach, based on a Taylor series expansion of Eq. (1.7), as defined in Eq. (1.8). This method predicts a natural frequency from $\mathbf{K}\boldsymbol{\varphi} = \lambda\mathbf{M}\boldsymbol{\varphi}$, and the first and second terms of the Taylor series expansion are used to construct the transformation matrix. $\mathbf{M}_G$ and $\mathbf{K}_G$ are the reduced mass and stiffness matrices constructed by the Guyan reduction method. The IRS transformation matrix in Eq. (1.8) turns out to be the first step of the IIRS transformation matrix, by updating as in Eq. (1.10) and Eq. (1.11).

$$\mathbf{K}_{IIRS}^{(i)} = \mathbf{K}_{pp} + \mathbf{K}_{ps}\mathbf{t}_{IIRS}^{(i-1)} + (\mathbf{t}_{IIRS}^{(i-1)})^T\mathbf{K}_{sp} + (\mathbf{t}_{IIRS}^{(i-1)})^T\mathbf{K}_{ss}\mathbf{t}_{IIRS}^{(i-1)}, \tag{1.10}$$

$$\mathbf{M}_{IIRS}^{(i)} = \mathbf{M}_{pp} + \mathbf{M}_{ps}\mathbf{t}_{IIRS}^{(i-1)} + (\mathbf{t}_{IIRS}^{(i-1)})^T\mathbf{M}_{sp} + (\mathbf{t}_{IIRS}^{(i-1)})^T\mathbf{M}_{ss}\mathbf{t}_{IIRS}^{(i-1)}. \tag{1.11}$$

To improve the accuracy of the restored matrices, an IIRS was introduced in Eq. (1.9) to construct the nonlinear transformation matrices through iteration. The reduced stiffness and mass matrices are shown in Eq. (1.10) and Eq. (1.11),

respectively. In this study, more than 15 iterations were performed, to ensure the accuracy. The experimental data were applied to the equations, and the values obtained in the experiments were applied to the corresponding DOFs to form the PDOFs. Previous system identification studies have compared the eigenvalues or simple parameters to determine the model perturbations. However, in a continuum model a full matrix of eigenvectors should be compared, to reflect the complexity of the mode shapes. The reduction method introduced here reduces the number of parameters and enables the application of the identification process to a continuum model. The accuracy of the present simulation was verified by comparing each mode shape with the commercial ABAQUS solution for four-node deformable shells. This guaranteed the accuracy of the present simulation. The eigenvalues of the reference and perturbed models are listed in Table 1.1.

Table 1.1 The comparison of the eigenvalues of the reference model and the numerical perturbed model.

Mode	Reference (λ)	Perturbed (λ')	Error ($(\lambda'-\lambda)/\lambda$)
1	329.55	332.13	+0.78%
2	457.95	465.53	+1.66%
3	911.74	929.49	+1.95%
4	988.32	1017.66	+2.97%
5	1665.10	1692.10	+1.62%

1.2.3 Proper orthogonal decomposition (POD)

The main idea of the proper orthogonal decomposition (POD) is to find a set of ordered orthonormal basis vectors in a subspace (without loss of generality, denoting the subspace as R^m) where a random vector takes its values, such that the samples in the sample space can be expressed optimally using the selected first *l* basis vectors. The mean square error can be used as a measure for the optimal problem, i.e.,

$$E\left\{\left\|x-x(l)\right\|^2\right\} \le E\left\{\left\|x-\hat{x}(l)\right\|^2\right\}, \tag{1.12}$$

where *x*(*l*) is the approximate expression of a random vector *x* using the first *l* basis vectors of the undetermined set of orthonormal basis vectors, and $\hat{x}(l)$ is the approximate expression of *x* using arbitrary *l* basis vectors in R^m. The problem can be stated as follows. Assume that $x \in R^m$ is a random vector and $\{\phi_i\}_{i=1}^m$ is a set of arbitrary orthonormal basis vectors: then *x* can be expressed as

$$x = \sum_{i=1}^{m} y_i \phi_i = \Phi y, \tag{1.13}$$

where

$$y_i = \phi_i^T x \quad (i = 1, 2, \ldots, m),$$
$$y = (y_1, y_2, \ldots, y_m)^T, \quad \Phi = [\phi_1, \phi_2, \ldots, \phi_m].$$

The objective of the POD is to find a set of basis vector that satisfies the following extreme value problem:

$$\min_{\phi_i} \varepsilon^2(l) = E\left\{\left\|x - x(l)\right\|^2\right\}$$
$$\text{s.t.}\, \phi_i^T \phi_j = \delta_{ij} \qquad i, j = 1, 2, \ldots, m, \tag{1.14}$$

where $x(l) = \sum_{i=1}^{l} y_i \phi_i \; (l \le m).$ In order to obtain the same form of expressions for the mean-square errors by using the three different POD methods, the centralization on the processing data is assumed, i.e., the expectation of the random vector *x* is zero.

1.2.4 System equivalent reduction-expansion process (SEREP)

By assuming the equation of motion of mass, damper and stiffness matrix formation, $\mathbf{M}\ddot{x} + \mathbf{C}\dot{x} + \mathbf{K}x = \mathbf{F}.$ To reduce the size of the system to a smaller size with *p* modes or the *m* degrees of freedom, where *p* is defined based on the expected bandwidth of the excitation and *m* is defined based on the number of degrees of freedom that are acted upon by an external load, the number of retained coordinates is constrained to be equal to the number of retained modes, and is chosen to be the larger of *p* or *m*. Then the coordinate vector can be partitioned into two parts, x_r and x_t, the retained and truncated coordinates, and reorganize the equation of undamped motion in the following equation:

$$\begin{bmatrix} M_{rr} & M_{rt} \\ M_{tr} & M_{tt} \end{bmatrix} \begin{bmatrix} \ddot{\mathbf{x}}_r \\ \ddot{\mathbf{x}}_t \end{bmatrix} + \begin{bmatrix} K_{rr} & K_{rt} \\ K_{tr} & K_{tt} \end{bmatrix} \begin{bmatrix} \mathbf{x}_r \\ \mathbf{x}_t \end{bmatrix} = \begin{bmatrix} \mathbf{F}_r \\ 0 \end{bmatrix}. \tag{1.15}$$

When considering the eigensolution for the mass normalized eigenvectors, $\Phi = [\Phi_{ar} \quad \Phi_{at}]$ where *r* and *t* stands for retained and truncated, and a represents that all coordinates are retained in the vector. The modes to be retained, Φ_{at}, is an

$n \times (n-m)$ matrix.

$$\mathbf{x} = \begin{bmatrix} \mathbf{x}_r \\ \mathbf{x}_t \end{bmatrix} = \mathbf{\Phi r} = \begin{bmatrix} \Phi_{ar} & \Phi_{at} \end{bmatrix} \begin{bmatrix} \mathbf{r}_r \\ \mathbf{r}_t \end{bmatrix} = \begin{bmatrix} \Phi_{rr} & \Phi_{rt} \\ \Phi_{tr} & \Phi_{tt} \end{bmatrix} \begin{bmatrix} \mathbf{r}_r \\ \mathbf{r}_t \end{bmatrix}, \tag{1.16}$$

$$\Phi^T = \begin{bmatrix} \Phi_{ar} & \Phi_{at} \end{bmatrix}^T, \tag{1.17}$$

$$I\ddot{\mathbf{r}} + \lambda \mathbf{r} = \Phi^T \mathbf{F}, \tag{1.18}$$

$$\begin{bmatrix} \Phi_{ar}^T \\ \Phi_{at}^T \end{bmatrix} \begin{bmatrix} M_{rr} & M_{rt} \\ M_{tr} & M_{tt} \end{bmatrix} \begin{bmatrix} \Phi_{ar} & \Phi_{at} \end{bmatrix} = \begin{bmatrix} \Phi_{ar}^T M \Phi_{ar} & \Phi_{ar}^T M \Phi_{at} \\ \Phi_{at}^T M \Phi_{ar} & \Phi_{at}^T M \Phi_{at} \end{bmatrix} = \begin{bmatrix} I_r & \\ & I_t \end{bmatrix}, \tag{1.19}$$

$$\begin{bmatrix} \Phi_{ar}^T \\ \Phi_{at}^T \end{bmatrix} \begin{bmatrix} K_{rr} & K_{rt} \\ K_{tr} & K_{tt} \end{bmatrix} \begin{bmatrix} \Phi_{ar} & \Phi_{at} \end{bmatrix} = \begin{bmatrix} \Phi_{ar}^T K \Phi_{ar} & \Phi_{ar}^T K \Phi_{at} \\ \Phi_{at}^T K \Phi_{ar} & \Phi_{at}^T K \Phi_{at} \end{bmatrix} = \begin{bmatrix} \Lambda_r & \\ & \Lambda_t \end{bmatrix}, \tag{1.20}$$

$$\Phi_{rr}^{-1^T} \Phi_{ar}^T M \Phi_{ar} \Phi_{rr}^{-1} \ddot{\mathbf{x}}_r + \Phi_{rr}^{-1^T} \Phi_{ar}^T K \Phi_{ar} \Phi_{rr}^{-1} \mathbf{x}_r = \Phi_{rr}^{-1^T} \Phi_{ar}^T \mathbf{F}, \tag{1.21}$$

$$T = \Phi_{ar} \Phi_{rr}^{-1} = \begin{bmatrix} \Phi_{rr} \\ \Phi_{tr} \end{bmatrix} \Phi_{rr}^{-1} = \begin{bmatrix} I \\ \Phi_{tr} \Phi_{rr}^{-1} \end{bmatrix}, \tag{1.22}$$

$$\tilde{\mathbf{M}} \ddot{x}_r + \tilde{\mathbf{C}} \dot{x}_r + \tilde{\mathbf{K}} x_r = \tilde{\mathbf{F}}, \tag{1.23}$$

where $\tilde{\mathbf{M}} = \mathbf{T}^T \mathbf{M} \mathbf{T}, \tilde{\mathbf{C}} = \mathbf{T}^T \mathbf{C} \mathbf{T}, \tilde{\mathbf{K}} = \mathbf{T}^T \mathbf{K} \mathbf{T}$ and $\tilde{\mathbf{F}} = \mathbf{T}^T \mathbf{F}$. As in Eq. (1.22), the transformation matrix constructed through SEREP can be expressed with eigenvectors of the selected DOFs. The transformation matrix construction using SEREP will be applied in advanced system identification process to improve the calculation efficiency in Chapter 4.3.

1.3 Structural system identification

Structural system identification methods have been applied in areas such as health monitoring and damage detection **[1-4, 25-34]**. For safety reasons, it is important to examine the states of aging complex engineering structures or machines that require precise machining. The potential presence of structural defects can be diagnosed using periodic measurements and tests. Structural defects can assume a variety of forms and evolve through various routes, including corrosion and aging. Minute structural changes must be detected, because the reliability and accuracy of an entire structure depends on the detection of structural changes. Therefore, it is critical to accurately detect structural changes using accurate measurements. Many studies have attempted to improve the accuracy and efficiency of system identification approaches.

One example of a system identification method is the model update method. In this approach, a reference structure is updated using a system with the dynamic characteristics of the actual structure, by using the values obtained from an experimentally measured perturbation model. The updated structural model can be employed for structural defect analysis and diagnosis. A variety of methods have been developed to improve the accuracy of the model update method, and these have been applied, for example, to H-frames and F-frames **[2, 25-30]**, truss structures **[3, 31-33]**, cantilever beams, and cantilever plates **[4, 34]**. Most identification methods minimize the identification indices, which represent the differences between the behaviors of the reference and perturbation models. The accuracy and efficiency of an identification method depends on the selection of the

identification indicators. Simple identification indicators, such as displacements, natural frequencies, and mode shapes have been selected in such methods using a conventional identification process. The residual errors in the corresponding balance equation are then minimized. The inverse perturbation method (IPM), which employs the residual energy-based eigenvalue balance equation as an indicator, has also been described **[5-7]**. The application of the eigenvalue balance equation for system identification was considered to be physically reasonable. The convergence of the residual error minimization could be improved by applying more advanced methods **[7]**.

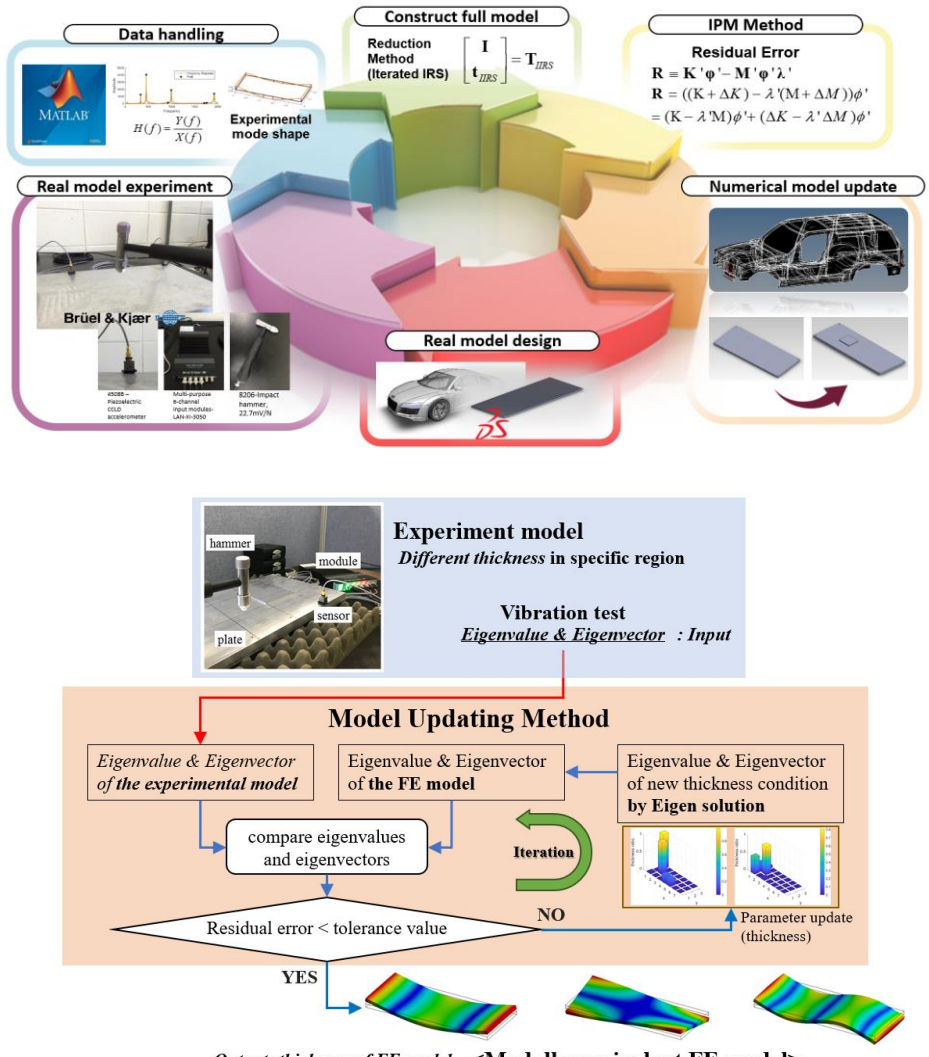

Figure 1.1 Proposed model update method using degree of freedom-based reduction method.

Although the eigenvalue balance equation is physically appropriate, the obtained response should account for all degrees of freedom (DOFs) of the FE (finite element) model. It is impossible to measure the individual responses across all DOFs, owing to an insufficient number of sensors and the simplifications required to model a real system. In the conventional IPM, the responses of DOFs not obtained from measurements become additional system parameters. These additional system parameters significantly reduce the identification efficiency as the scale of the problem increases. A system reduction method, which calculates the transformation matrix with a high accuracy and overcomes the inefficiencies resulting from the large number of system parameters, has been developed **[8-10]**. Several studies of system identification have been conducted using the balance equation and reduction method **[11-23]**. Rather than adding additional system parameters to obtain the unspecified responses of the DOFs, in the system reduction method the responses of the measured DOFs are projected to determine the responses of the unmeasured DOFs **[17-18]**. However, the errors from the measured DOFs produce a transformation error in the estimation of the unmeasured DOF responses. In the inverse problem, a minor error in the transformation process can significantly influence convergence during iterative calculations. The accuracy and convergence of the reduction method are also influenced by the selection of the measured DOFs. It is necessary to select appropriate sensor locations in order to accurately calculate the transformation matrix. In this study, a sensor location selection method for accurate system identification is proposed and verified numerically and experimentally.

Here, the IPM is employed to compare the reference model (simulation) with the perturbed model (experiment), and the balance equation is presented. The

eigenvectors and eigenvalues become indicators of the differences between the two models, using the system reduction method. A DOF-based reduction method is applied to construct a full model based on a limited test data set. Because the identification problem depends on the measured information, a sensor location selection method is introduced. The quality of the measured data determines the accuracy of the identified model and the convergence of the identification problem. A three-dimensional (3D) aluminum plate was selected for the structural system identification process. Numerical examples were produced, and these were compared with the experimental model to validate the identification process. The parameters that represent the numerical model were updated by comparing their 3D mode shapes to the experimental data from the proposed sensor locations. The mode shape comparison was calculated by minimizing the residual error. Through the proposed identification method, we were able to identify changes in the actual aluminum models.

1.3.1 Balance equation for system identification

Vibrational responses are only attainable at a limited number of DOFs, owing to limitations on the positioning of sensors in the experiment. Because sensors can only be located at specific nodes, determining their placement is important. Therefore, the use of the reduction method with specific nodes during structural system identification can be powerful, especially when using a complex finite element model. One reduction method involves expressing a full model using only specific DOFs. In general, the analysis of a half meter-sized plate model requires at least over 1,000 nodes to express the dynamic mode shapes. This means that more than 1,000 vibrational data points are required for comparison with the numerical

analysis model. It is almost impossible to measure the response at every vibrational data point, and so making decisions on where to measure and how to restore the full model is key for data mining. A system reduction method could be applied at this point **[8-10]**. Because DOF-based reduction methods employ specific DOFs to rapidly calculate the full model while maintaining the model's accuracy, this method could be applied reversely to structural system identification problems using a continuum model with many DOFs.

1.3.2 The inverse perturbation method

To apply the reduction method to system identification, an identification equation should be initially determined. A schematic diagram of the reference and perturbed models is presented in Fig. 1.2. The reference model features a uniform thickness across all elements. The perturbed model features a uniform thickness across most elements, but the thickness differs at specific elements. The eigenvalue problem equations are

$$\mathbf{K}\boldsymbol{\varphi} = \lambda\mathbf{M}\boldsymbol{\varphi}, \tag{1.24}$$

$$\mathbf{K}'\boldsymbol{\varphi}' = \lambda'\mathbf{M}'\boldsymbol{\varphi}'. \tag{1.25}$$

The reference and perturbed models may be expressed as $\mathbf{K},\mathbf{M}$, and $\mathbf{K}',\mathbf{M}'$, respectively. A perturbation at a specific section is introduced by adding components to the stiffness matrix $(\mathbf{K}')$ and mass matrix $(\mathbf{M}')$.

The eigenvalues and eigenvectors of the reference and perturbed models may be expressed as $\lambda,\boldsymbol{\varphi}$, and $\lambda',\boldsymbol{\varphi}'$, respectively. The perturbations of the model

were achieved by applying the IPM and minimizing the residual error $(\mathbf{R})$ **[5-7]**,

$$\mathbf{R} = \mathbf{K}'\boldsymbol{\varphi}' - \lambda'\mathbf{M}'\boldsymbol{\varphi}'. \tag{1.26}$$

Perturbations were added to the model by introducing additional matrices, and the eigenvalues and eigenvectors of the perturbed model were calculated. The perturbed stiffness matrix can be divided into the reference stiffness $(\mathbf{K})$ and the variation amount of the perturbed stiffness $(\Delta\mathbf{K})$, and the perturbed mass matrix can be divided into the reference mass $(\mathbf{M})$ and the variation amount of the perturbed mass $(\Delta\mathbf{M})$,

$$\mathbf{R} = (\mathbf{K} + \Delta\mathbf{K})\boldsymbol{\varphi}' - \lambda'(\mathbf{M} + \Delta\mathbf{M})\boldsymbol{\varphi}'. \tag{1.27}$$

The parameters of numerical model, $\Delta\mathbf{K}$ and $\Delta\mathbf{M}$ will be identified by checking whether the residual error equation is minimized. The parameters can consist of any variables that can be expressed by the mass–stiffness equation. The parameters will be changed during the iteration to find the numerical model that matches with the eigenvalues and eigenvectors of the perturbed model.

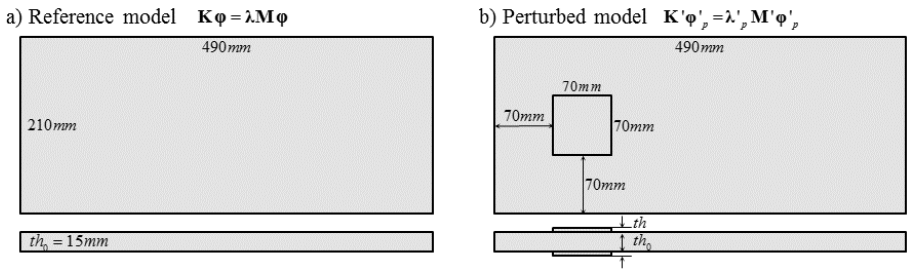

Figure 1.2 (a) The reference model, and (b) perturbed model (at the ninth section). The reference thickness (th_0) and the perturbed thickness (th) are illustrated in the bottom.

The IPM was applied to identify the differences between the parameters of the reference and perturbed models. The exact eigenvalues were used to improve the accuracy of the first-order equation. By changing the parameters during each iteration, Eq. (4) identified the minimum residual error that agreed with the eigenvalues and eigenvectors in the perturbed model. At the minimum residual error point, $\Delta\mathbf{K}$ and $\Delta\mathbf{M}$ represent the solution to the perturbation problem, and the obtained parameters can be applied when updating the reference model (Fig. 1.2). As a summary, a flow chart algorithm describing the structural system identification method is presented in Fig. 1.3. The eigenvalues and eigenvectors of the experimental data in the specific sensor locations are expressed as λ_p and $\boldsymbol{\varphi}_p$, respectively, with the subscript p identifying the primary DOFs. The parameters for the identification problem will be updated until the residual error satisfies the tolerance value. A detailed explanation of each part will be provided throughout following sections.

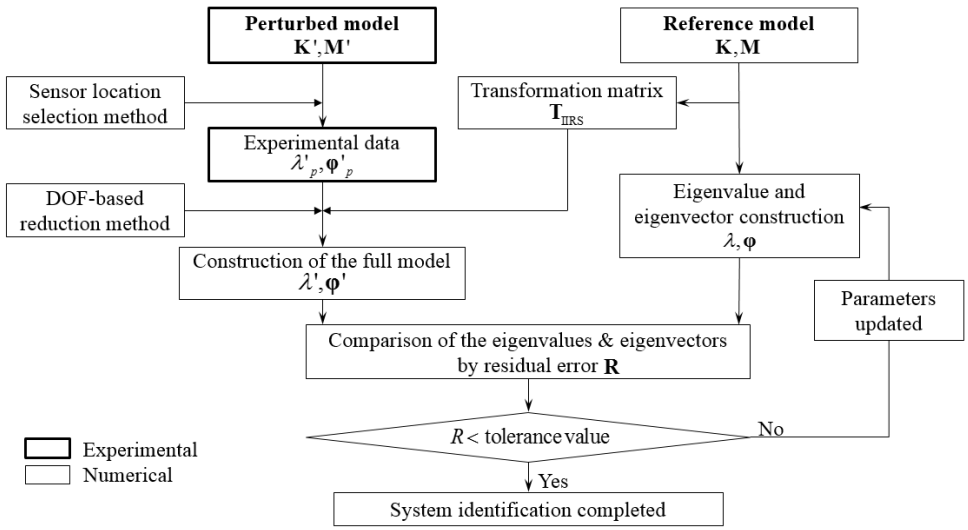

Figure 1.3 Structural system identification algorithm.

1.4. Machine learning in identification process

The identification method was introduced through previous sections. The time-consuming part of the given process is the eigen solution part and transformation matrix construction part in each iteration of the identification process. The new eigen solution and transformation matrix construction using neural network will be introduced. Through employing the training set to the identification method, the time-consuming calculation part have been handled and decreased the calculation time. The eigen solutions were constructed in different perturbation conditions before the identification process and trained by neural network system. The transformation matrices were restored by the constructed eigen solution via system equivalent reduction expansion process (SEREP).

Chapter 2.

Sensor location selection method

2.1 Vibration test setup

2.1.1 Vibration test setup for system identification

A vibration test was performed to obtain the eigenvalues and eigenvectors for the perturbed model. A reference aluminum plate model is presented in Fig. 2.1(a). The experimental perturbed model shown in Fig. 2.1(b) was fabricated using A6061-T6 aluminum. The identification was explored using 21 sections to describe same-sized square sections, as shown in Fig. 2.1(a). Each section was characterized by its own thickness parameter. Figure 2.1(b) shows an accelerometer positioned on the plate model, and an impact hammer was employed to create vibrations. A photo of the impact vibration test is presented in Fig. 2.1(b).

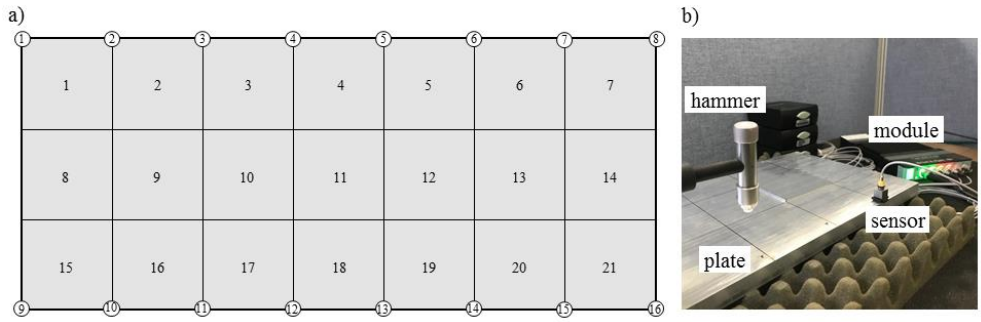

Figure 2.1 (a) Aluminum plate (A6061-T6) divided into 21 sections. Each section had a different thickness. (b) Piezoelectric accelerometer (4508B), multi-purpose four-channel input modules (LAN-XI-3050), and 8206-impact hammer (8206).

The thickness of the perturbed model varied across different sections. The thicknesses of the elements in the FE method constitute the parameters used to describe this problem. The identification problem described in this study involves the determination of the element thickness, and the identification proceeded using a thickness ratio (th / th_0) in the range of 1.0 to 1.35, considering a realistic perturbation. Furthermore, the parameters used in the identification process can consist of any variable that can be expressed by the mass–stiffness equation. The perturbed model was constructed using the experimental data, and compared with the reference model. In the following section, a methodology for improving the accuracy of the experiment will be introduced. The identification results combined with the experimental data will be shown in the results and discussion section.

2.1.2 Vibration data rebuilt for in-house code

Structural system identification method matches computational model and real model by experimental responses. Since the matching is critical object for this study, delicate experimental skills are necessary. Unfortunately, matching process without experiment, the significance of this kind of study decreases.

Eigenvalue and eigenvector can be measured from vibration test equipment. Figure 2.1 shows the sensor(accelerometer), impact hammer and multi-purpose 6-channel input module that are used for this vibration test. Frequency response function is measured from each sensor and shows different eigenvector from each location, but shows the same eigenvalue through the same model. Coherence from each point gives reliability of the experiment throughout impacting more than three times each. Frequency response function is calculated by dividing the output of frequency domain and the input frequency domain from impact hammer so that effectiveness of hammer decreases. Mode shape of the model can be constructed by the data from vibration test using degree of freedom-reduction method.

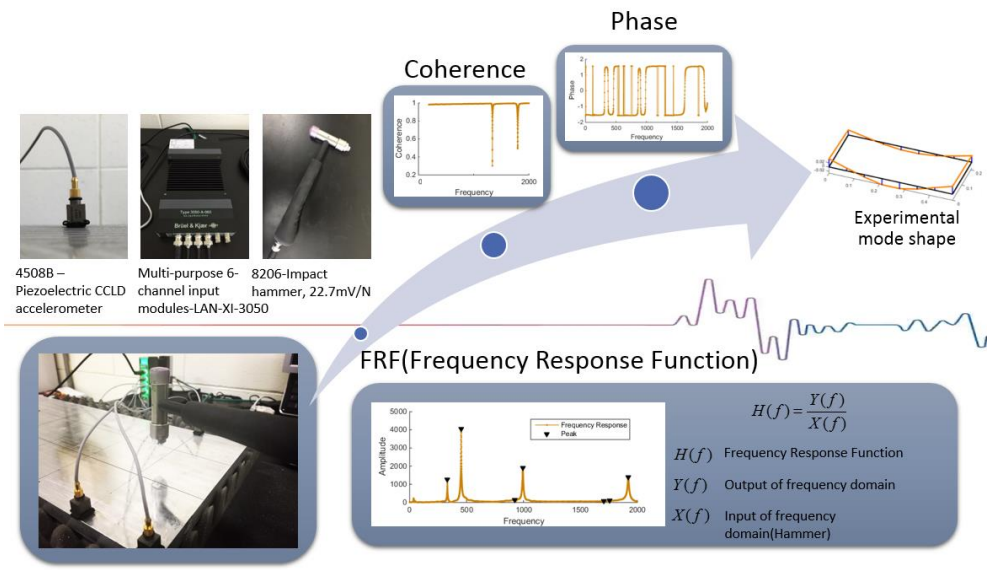

Figure 2.2 Vibration test equipment and functions measured from impact vibration test.

Measured peaks are detected and calculated as eigenvector of each point on each mode shapes, and constructs mode shapes by restoration process. Fig. 2.3(c) shows the blind spot when eigenvector of relevant point is zero. When the peak value does not seem to detect, then the order of the post mode shapes starts to be disturbed. These points disturb the information of the data from vibration test, thus these points are considered as nodal point and conferred as critical point during the process. Considering of nodal point became issue when selecting sensor location on vibration test. Since gathered data from vibration test is only from the selected location, reliable of unmeasured data depends on measured data. Error of measurement influences to the full model matrices when restoring, and can be easily validated by simple one-dimensional numerical bar problem.

Low frequency modes, which have more energy than others, are considered from the simple bar problem. Fig. 2.5 and 2.6 shows the calculated mode shape from common point and nodal point. The first case is the mode shape restored from the point which is not nodal point and the same mode shape with exact mode shape appears. On the other hand, in case number 2, is the restored mode shape from nodal point. Mode shape on 2nd case seems to fluctuate besides the region of the measured point itself. Nodal point itself didn't seem to have large error, but its influence increased during the restoration process.

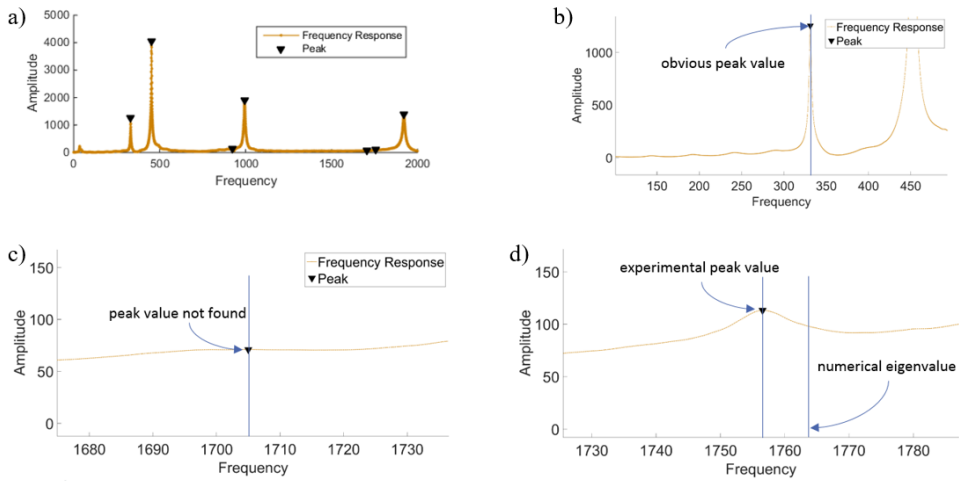

Figure 2.3 Peak detecting process from a sensor point. (a) frequency response function from a sensor (b) eigenvector detected (c) peak value not found (d) miss targeted eigenvector.

2.2 Nodal point consideration

2.2.1 Sequential elimination method

As mentioned above, the accuracy in the degree of freedom-based reduction depends on which degree of freedom is selected as the main freedom. Therefore, research on the selection of the degree of freedom has been actively conducted. The main degree of freedom selection technique introduced in this section is applied in Chapter 2.3 as a sensor positioning technique for system identification. The sequential elimination method **[37]** is one of the commonly used methods of selecting the main degree of freedom. The process of selecting the degree of freedom for this technique is as follows.

Step 1. Find the ratio of the diagonal terms ($\mathbf{K}_{ii} / \mathbf{M}_{ii}$) of the stiffness matrix to the mass matrix. The degree of freedom with the largest value is determined as the degree of freedom.

Step 2. Perform static reduction method in the form of eliminating the fixed independence.

Step 3. Repeat steps 1 and 2 until the ratio of the diagonal term reaches the cutting frequency or the number of free degrees of freedom.

In the second stage of reduction, other reduction techniques described in Section 1.2.1 can be applied in addition to the static reduction (Guyan technique) **[8]**. The Guyan technique is only advantageous in terms of calculations.

Sequential elimination has the advantage of relatively simple calculation and high reliability. However, since the single degree of freedom is removed at each stage, the main freedom degree selection time increases exponentially in large structures.

2.2.2 Energy method

In order to overcome the drawbacks in the computational time of sequential elimination, Kim and Choi proposed a method to select the degree of freedom by evaluating the energy for each degree of freedom **[38]**. By calculating the energy of each degree of freedom and selecting the desired number of free degrees at once, there is no repetitive process such as the sequential elimination method, so that the effect on the calculation time can be obtained.

The energy of each degree of freedom is expressed as

$$Energy = \sum_{i=1}^{n} \sum_{k=i}^{n} \phi_{ij} M_{ik} \phi_{kj}. \tag{2.1}$$

The is the Ritz vector value (ϕ_{ij}) of the first row and the column, and the first row and the column of the mass matrix. *n* is the number of modes considered, and considering 1 mode as the total number of degrees of freedom (N) in the above equation, the summation becomes 1 as shown in the following equation.

$$\sum_{i=1}^{N} \sum_{k=i}^{N} \phi_{ij} M_{ik} \phi_{kj} = 1. \tag{2.2}$$

Krammer **[39]** proposed that a relatively accurate result can be expected when the sum of energy considering n modes corresponding to a desired frequency band is about 0.4 to 0.5.

Such energy prediction techniques often reflect lower order modes or show different selection trends depending on the element size. To compensate for this

drawback, some weights are given below.

$$Energy = \sum_{i=1}^{n} \sum_{k=i}^{n} \phi_{ij} M_{ik} \phi_{kj} \left(1 - \frac{\lambda_j}{\lambda_{n-1}} \right). \tag{2.3}$$

2.2.3 Nodal point consideration

The experimentally measured peaks in the frequency data were detected, and determined as the eigenvectors of each point in the model. The mode shapes were constructed using the restoration process. However, at certain exceptional points blind spots occurred, in which the eigenvector of the relevant point approached zero. If the peak values were not detected, then the order of the upcoming eigenvectors was disturbed. These exceptional points degraded the experimental information. Thus, these points were managed differently during the process, and were considered to be nodal points. Consideration of the FE nodes at the nodal points is an issue associated with the positioning of sensors on the experimental plate model. Because the data gathered from the experiments were only collected from selected locations, the reliability of the full restored model depended on the measured data. The errors in the measurements influenced the full model matrices during restoration.

2.2.4 Numerical examples

The influence of the errors from the nodes at the nodal points was examined by considering a 1D bar problem. A 1D bar with five FE nodes is illustrated in Fig. 2.4, and the stiffness and mass matrices can be constructed using the FE method. The example was simplified by considering only the second mode shape. The

second and fourth FE nodes were located at the nodal points. The first, second, and fourth FE nodes were selected as the PDOFs, and errors of equal magnitude were added. The PDOF and the SDOF were divided and calculated separately.

$$\mathbf{K}_{ss} = \begin{bmatrix} 2 & 0 \\ 0 & 1 \end{bmatrix}, \mathbf{K}_{sp} = \begin{bmatrix} 0 & -1 & -1 \\ 0 & 0 & -1 \end{bmatrix}, \mathbf{M}_{ss} = \begin{bmatrix} 2 & 0 \\ 0 & 1 \end{bmatrix}, \mathbf{M}_{sp} = \begin{bmatrix} 0 & 0 & 0 \\ 0 & 0 & 0 \end{bmatrix}, \quad (2.4)$$

$$\mathbf{t}_G = -\begin{bmatrix} 2 & 0 \\ 0 & 1 \end{bmatrix}^{-1} \begin{bmatrix} 0 & -1 & -1 \\ 0 & 0 & -1 \end{bmatrix} = \begin{bmatrix} 0 & 1/2 & 1/2 \\ 0 & 0 & 1 \end{bmatrix}. \quad (2.5)$$

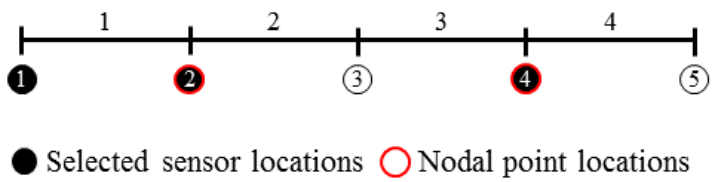

Figure 2.4 1D numerical bar problem. Red circles denote the additions of errors at the nodes at nodal points.

Each PDOF and SDOF could be decomposed using the constructed stiffness and mass matrices, as shown in Eq. (2.4). Each decomposed matrix was used in the reduction method. Equation (2.5) shows the construction of the Guyan transformation matrix $\mathbf{t}_G$, and the IIRS transformation matrix could be constructed as

$$\mathbf{t}_{IIRS} = \begin{bmatrix} -1 & 1+\sqrt{\frac{1}{2}} & 1-\sqrt{\frac{1}{2}} \\ 1 & -\sqrt{2} & \sqrt{2} \end{bmatrix}. \tag{2.6}$$

The Guyan transformation matrix was applied during the first stage of the IIRS reduction method, and then updated during each iteration step. As shown in Fig. 2.5, it is necessary to calculate at least 15 iterations to obtain an accurate transformation matrix.

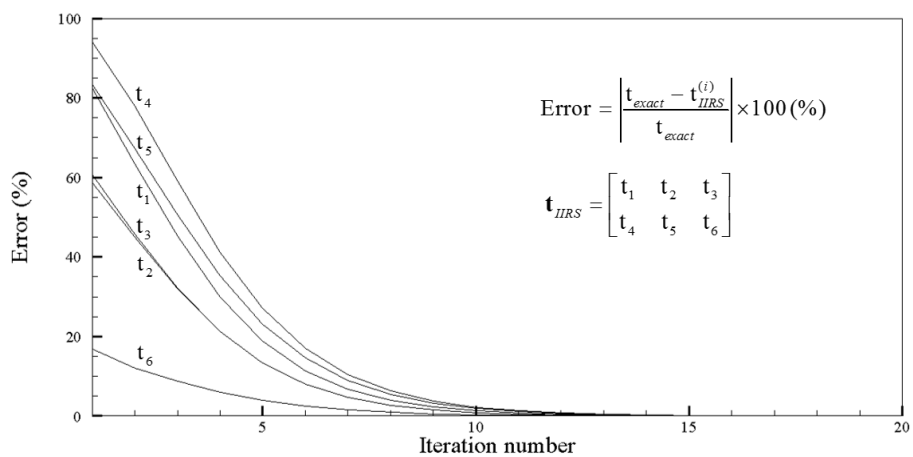

Fig. 2.5 Error convergence of the transformation matrix component.

The transformation matrix $\mathbf{t}_{IIRS}$ was employed in the DOF-based reduction method to express the full model in terms of the PDOF in Eq. (1.9). The full eigenvector of the 1D bar was restored using $\mathbf{t}_{IIRS}$. The measurement error was examined for the normal and nodal points of the PDOFs. The eigenvector for the first, second, and fourth DOFs in the second mode shape was expressed as $[-0.5,\ 0,\ 0]$. The second and fourth FE nodes were located at the nodal points, and their amplitudes for the eigenvector were zero. The eigenvectors of the restored full model are shown below:

$$\boldsymbol{\varphi}_{original} = 0.5\begin{bmatrix}-1\\0\\1\\0\\-1\end{bmatrix}, \boldsymbol{\varphi}_{normal\ error} = (0.5-\alpha)\begin{bmatrix}-1\\0\\1\\0\\-1\end{bmatrix}, \boldsymbol{\varphi}_{nodal\ error} = \begin{bmatrix}-0.5\\\alpha\\0.5+\left(1+\sqrt{2}\right)\alpha\\0\\-0.5-\sqrt{2}\alpha\end{bmatrix}. \tag{2.7}$$

The virtual measurement error α has been added to show the difference in the influence of the measurement error. The influence of the error α on the nodal points was verified by adding α to the FE nodes at the nodal points and comparing with those obtained by the addition of the same error to the nodes at the normal points. The case in which the error was added at the normal points yielded the same eigenvector, without exhibiting any errors. On the other hand, the case in which the error was added at the nodal points led to a distorted eigenvector. These results revealed a significant error propagation in the eigenvectors of the global domain. This simple 1D bar problem illustrated that the error at the FE nodes at the nodal points influenced the results obtained when restoring the full model using the

measured data. Therefore, when selecting the sensor locations, the FE nodes at the nodal points should be avoided.

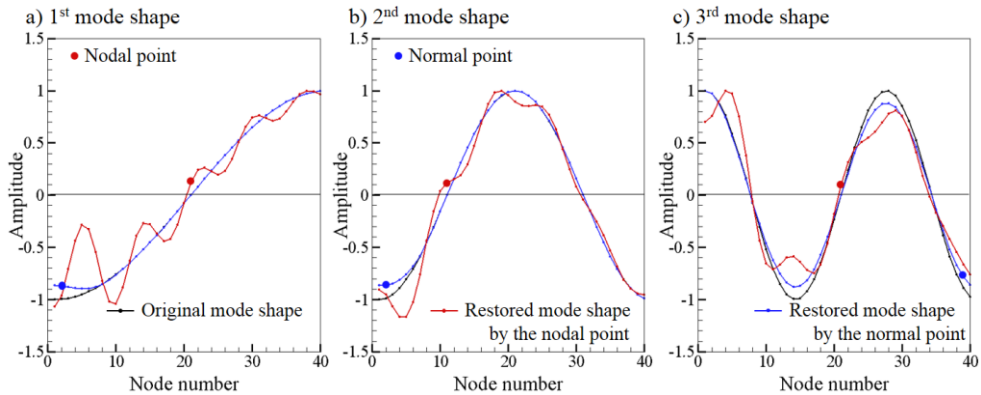

Figure 2.6 The first three restored mode shapes by the normal and nodal points. (a) The first mode shape obtained by adding a 1% error on the 2nd and 21st nodes. (b) The second mode shape on the 2nd and 11th nodes. (c) The third mode shape on the 40th and 21st nodes.

For further validation, the first three mode shapes of the same 1D bar with 40 elements were applied in Fig. 2.6. Each mode shape was calculated by adding a 1% error to the normal and nodal points, and then compared with the original mode shape. For the first mode shape in Fig. 2.6(a), the blue-colored mode shape is restored with the error added in the normal point (second node), and the red-colored shape is restored at the nodal point (21st node). For comparison, the second and third mode shapes are presented in Figs. 2.6(b) and (c). We found that the error added in the nodal points influenced the restoration and distorted the mode shapes.

2.3 Sensor location selection method

The influence of an error term at the nodal points revealed the risks associated with locating sensors at the nodal points. The nodal points were selected from each

mode shape, and therefore the mode shapes must be pre-selected to determine the critical nodal points for each process.

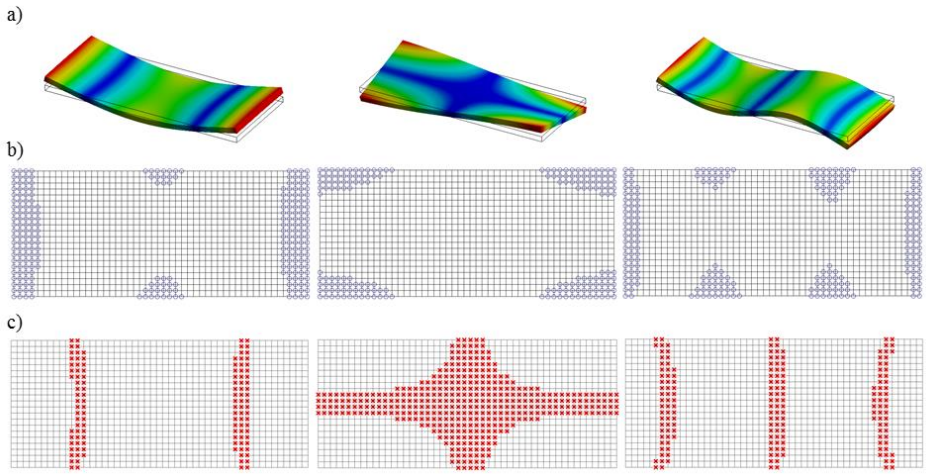

Figure 2.7 Sensor location selection method for the structural system identification problem. (a) The first three mode shapes of the plate model. (b) High kinetic energy DOFs of the selected mode shapes. (c) Vibrational nodal points determined from the first three mode shapes using the sensor location selection method.

The first step in Fig. 2.7 shows the first three mode shapes of the plate model, and the third step shows the nodal points evaluated from the first three mode shapes. As shown in Fig. 2.7, the nodal points appeared in the minimum displacement location of each mode shape. To select certain points to obtain high-quality data, three steps were followed:

Step 1. Regardless of the structural problem type, the correct mode shape must first be selected. As shown in Fig. 2.7(a), the lower frequency modes, which had large energies, were generally selected.

Step 2. The PDOFs were selected from the largest kinetic energy by calculating the Rayleigh quotient (R_e^i) based on the mode shapes of interest:

$$R_e^i = \frac{\left\{\boldsymbol{\varphi}^{(i)}\right\}^T \left[\mathbf{K}_e\right] \left\{\boldsymbol{\varphi}^{(i)}\right\}}{\left\{\boldsymbol{\varphi}^{(i)}\right\}^T \left[\mathbf{M}_e\right] \left\{\boldsymbol{\varphi}^{(i)}\right\}}, \tag{2.7}$$

where $\mathbf{M}_e$ and $\mathbf{K}_e$ are the mass and stiffness matrices constructed in each element. Critical points of the chosen specific mode shapes were selected as the sensor locations for the first step in Fig. 2.7(b), without considering the nodal points at this stage.

Step 3. Vibrational nodal points could be detected by calculating the Rayleigh quotient, although the minimum kinetic energy term was used. The high-energy nodes are marked with grey circles, and low-energy nodes are marked with red crosses. Some FE nodes are marked twice in some mode shapes. In the first step,

the FE nodes with high energies constituted the recommended sensor locations. However, for other mode shapes the corresponding FE nodes had low energies, and the positioning of the sensors here was contraindicated. It should be noted that vibrational nodal points were weak when errors were included. However, the mode shapes used for the process were selected prior to selecting the sensor locations. Excluding vibrational nodal points is the most important step in detection problems, such as structural system identification problems.

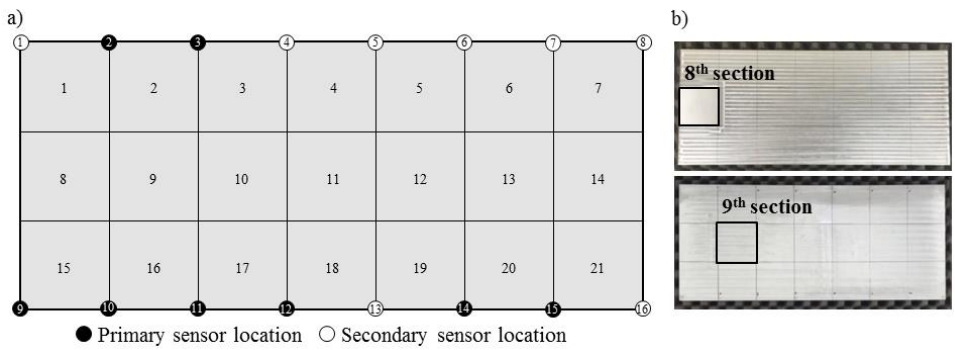

Figure 2.8 (a) The primary and secondary sensor locations. (b) Locations of the eighth and ninth sections.

It may be possible to select appropriate sensor locations that do not include nodal points associated with any mode shapes of interest. Figure 2.8(a) shows the primary sensor locations used to restore the full FE method mode. Figure 2.8(b) shows the perturbed sections presented in the examples. One of these included the perturbed part in the eighth section, and the other included the perturbed part in the ninth section. These two examples were selected within a section that could reveal differences in the mode shapes. Any elements exhibiting any changes could be selected as an example.

Chapter 3.

Residual error equation for identification process

3.1 Parameter optimizing equation setup

The general dynamic equilibrium equation can be expressed as the following equation.

$$\mathbf{Ku}-\lambda\mathbf{Mu}=\mathbf{0}. \tag{3.1}$$

Eq. (3.1) is the equilibrium equation of the initially assumed finite element model and is called the baseline system. The dynamic equilibrium of a real structure with structural changes due to various causes can be expressed as:

$$(\mathbf{K}+\Delta\mathbf{K})\mathbf{u}'-\lambda'(\mathbf{M}+\Delta\mathbf{M})\mathbf{u}'=\mathbf{0}. \tag{3.2}$$

This is called a perturbed system. λ' and u' in the above equations refer to the eigen value and vibration mode (eigenvector) of the actual structure obtained through the experiment, respectively. In addition, structural change ($\Delta\mathbf{K}$, $\Delta\mathbf{M}$) is expressed in the form of parameter ($\alpha_e{}^K$, $\alpha_e{}^M$) as in Eq. (3.3) for dimensionless structure change.

$$\Delta\mathbf{K} = \sum_{i=1}^{NE} \Delta\mathbf{K}_i = \sum_{i=1}^{NE} S_i^K \left(\alpha_i^K\right). \tag{3.3}$$

$$\Delta\mathbf{M} = \sum_{i=1}^{NE} \Delta\mathbf{M}_i = \sum_{i=1}^{NE} S_i^M \left(\alpha_i^M\right). \tag{3.4}$$

From the experimental data (λ', u') and the stiffness matrix ($\mathbf{K}$) and mass matrix ($\mathbf{M}$) of the initial finite element model obtained from the finite element model, an unknown structural change ($\Delta\mathbf{K}$, System identification proceeds in the form of $\Delta\mathbf{M}$). In this paper, we construct the residual error equation below using the above equilibrium equation.

$$\begin{aligned}\mathbf{R}(\boldsymbol{\alpha}) &= \left[\mathbf{K}'(\boldsymbol{\alpha}) - \lambda\mathbf{M}'(\boldsymbol{\alpha})\right]\mathbf{u} \\ &= \left[\mathbf{K} - \lambda\mathbf{M} + \sum_{i=1}^{NE}\left\{S_i^K\left(\alpha_i^K\right) - \lambda S_i^M\left(\alpha_i^M\right)\right\}\right]\mathbf{u}.\end{aligned} \tag{3.5}$$

Parameters are called system parameters that represent the system's characteristics of system identification and represent structural changes in stiffness and mass matrices.

$$\boldsymbol{\alpha} = \left\lfloor \alpha_1^K \quad \alpha_2^K \quad \cdots \quad \alpha_{NE}^K \quad \alpha_1^M \quad \alpha_2^M \quad \cdots \quad \alpha_{NE}^M \right\rfloor^T. \tag{3.6}$$

In some structural models that include rotational and translational degrees of freedom, such as shell elements, the weighting function of the following form is defined to prevent the problem of excessive emphasis of some rotational degrees due to the dimensional difference between two degrees of freedom. Converted to energy form.

$$W_{ii} = \left(\phi'_{ij}\right)^2. \tag{3.7}$$

Through this weighting, the final system identification problem is constructed in the form of finding the structural change (ΔK, ΔM) that minimizes the norm of residual energy.

$$\mathbf{R} = \mathbf{R}(\boldsymbol{\alpha}). \tag{3.8}$$

$$\text{Min}[\left\|\mathbf{R}(\boldsymbol{\alpha})^T \cdot \mathbf{W} \cdot \mathbf{R}(\boldsymbol{\alpha})\right\|]. \tag{3.9}$$

3.2 Converge criterion

The residual error $(\mathbf{R})$ is a key indicator that determines the parameters that agree with the perturbation, as described in Eq. (3.10).

$$\mathbf{R} = (\mathbf{K} + \Delta\mathbf{K})\boldsymbol{\varphi}' - \lambda'(\mathbf{M} + \Delta\mathbf{M})\boldsymbol{\varphi}'. \tag{3.10}$$

The parameters of the perturbed stiffness and mass matrices match with their eigenvalues and eigenvectors, which leads to the residual error attaining a minimum.

The perturbed model was restored using the frequency data gathered from selected DOFs, which correspond to the eigenvector $\boldsymbol{\varphi}'_p$, with the subscript p indicating primary DOFs. By utilizing the residual error constructed through the sensor location selection method, we could obtain the correct solution without any divergence in the given parameter range. The methods described here were employed to calculate the residual error based on the thickness ratio (th/th_0) as the parameter of the model, where th is the perturbed thickness and th_0 is the reference thickness.

$$Min\left((\mathbf{K}+\Delta\mathbf{K})\boldsymbol{\varphi}'-\lambda'(\mathbf{M}+\Delta\mathbf{M})\boldsymbol{\varphi}'\right). \tag{3.11}$$

The objective is to minimize the residual error in Eq. (3.11). The previously determined residual error was applied to determine the minimum. The additional residual error was modified by constructing the stiffness and mass matrices using the reduction method and sensor location selection method. By employing the method proposed in this study, the computational time can be minimized, and the convergence may be improved.

3.3 Weighting factor for parameter evaluation

$$\mathbf{R}=\mathbf{K}'\phi'-\mathbf{M}'\phi'\boldsymbol{\lambda}'. \tag{3.12}$$

The residual error $\mathbf{R}$ is defined from eigenvalue equilibrium equation. Differences between original reference model and perturbed experimental model

can be expressed as Eq. (3.12). $\boldsymbol{\lambda}'$ and $\boldsymbol{\phi}'$ are eigenvalue and eigenvector value each, which are gathered from vibration test. Both $\boldsymbol{\lambda}'$ and $\boldsymbol{\phi}'$ describes the dynamic responses of perturbed model. Perturbed stiffness matrix $\mathbf{K}'$ and mass matrix $\mathbf{M}'$ are described with finite element method and parameterized with its thicknesses from each element. $\mathbf{K}'$ and $\mathbf{M}'$ will be reconstructed depending on the thickness while residual error decreases to reach its minimum value.

$$\mathbf{R} = w_1 \sum_{i=1}^{NE} \left(\Delta \mathbf{K}_i - \lambda'_c \, \Delta \mathbf{M}_i \right) \varphi_c' + w_2 \sum_{j=1}^{NS} \frac{\left| \varphi'_{\mathrm{s,j}} - \varphi'_{\mathrm{c},j} \right|}{\varphi'_{c,j}}. \tag{3.13}$$

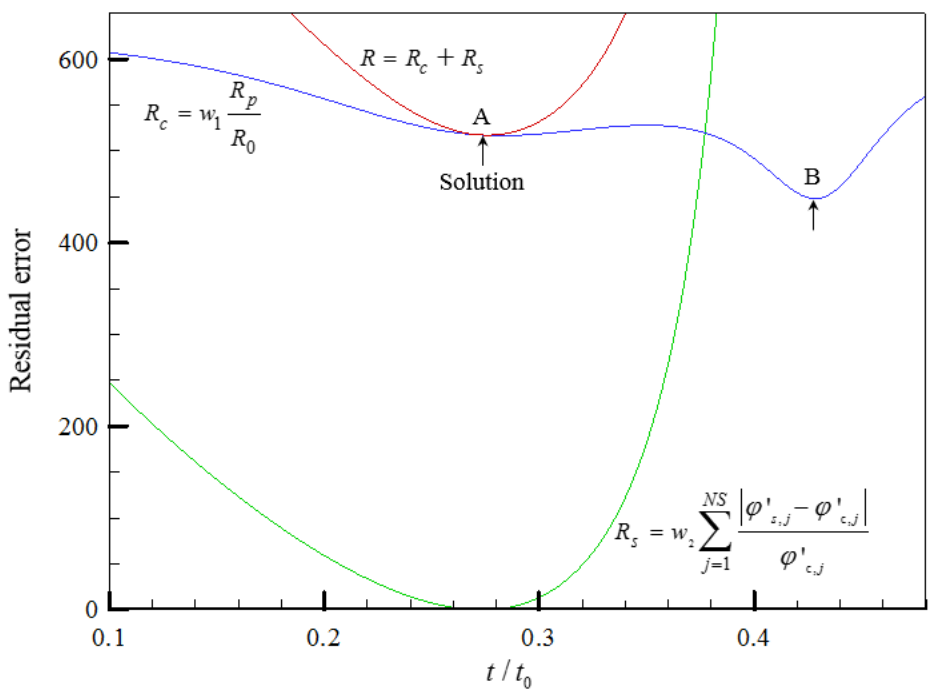

Figure 3.1 Convergence improvement of thickness identification

In simple structural system identification process, each element of the full model appears to be parameter to the inverse problem. As this study is an approach to handle such a complicated continuum problem, consideration of dramatically increasing number of parameters is unavoidable. Hence it also needs to simplify the number of parameters in identification process. Hierarchical approach by grouping sections divided, can be a methodology applied in this problem to handle increasing number of parameters. As a first step of hierarchical method, in this problem, given model can be divided into groups of interests, and each group will have uniform properties on them meshes. Damage detection has three levels, first is to find out if there is a damage on the model. Second level is to find the location of the damage. Lastly, determining the quantity of damage will be the last step. In this study, finding the region of the perturbation out of divided groups will be the second step and determining the value of the corresponding region will be the last step.

As a basic equation form of identification in this study, residual error has been constructed as Eq. (3.12). Corresponding residual error appeared to converge on the optimal parameter point. However, when thickness parameters face to the meaningless value outside the parameter range, residual error appeared to be the most proper answer to the problem, which is not. Residual error had to be reconstructed, preventing the answer to face to the proper answer. Hence, Eq. (3.13) has been proposed with additional term. The eigenvalue and eigenvector from experiment, as introduced before. Under letter s represents recommended (selected) sensor location and under letter *c* represents compared (other) sensor location. The compared eigenvectors are determined from analysis model in the selected sensor locations. The first term leads the residual error towards the

optimized parameter and second term avoids the residual value from falling into local minimum point which is wrong parameter values.

3.4 Identification examples

The structural system identification process was applied to an aluminum plate model. All the aluminum plates were produced in real plate models and identified by the proposed identification method. Since it is impossible to obtain the experimental information at all DOFs, we have devised the sensor location selection method based on the DOF-based reduction method. The identification process was progressed with the experimental information from the selected sensor locations. We were able to identify changes in the actual aluminum models through the proposed identification method. In Fig. 3.2, the *x* and *y* axes indicate the sections of the plate shown in Fig. 2.8. The *z*-axis denotes the estimated thickness change compared to the reference thickness $(|th_0 - th| / th_0)$. In the first example, the thickness of the ninth section was designed to differ from the thickness values of the remaining elements, corresponding to the secondary sensor location data. As shown in Fig. 3.2, the identification process failed when the sensors were located at nodal points. The secondary sensor locations were avoided when restoring the full FE method model in consideration of its nodal points. In the second example, the thicknesses of the eighth and ninth sections were designed to differ from those of the other elements, corresponding to the primary sensor location data. The primary sensor locations were recommended for the primary DOFs when restoring the full FE method model. This result was previously verified using a simple bar problem,

and restoring the full model using the nodal points appeared to be risky. The accuracy of the structural system identification process could be improved by avoiding the nodal points when selecting the sensor locations.

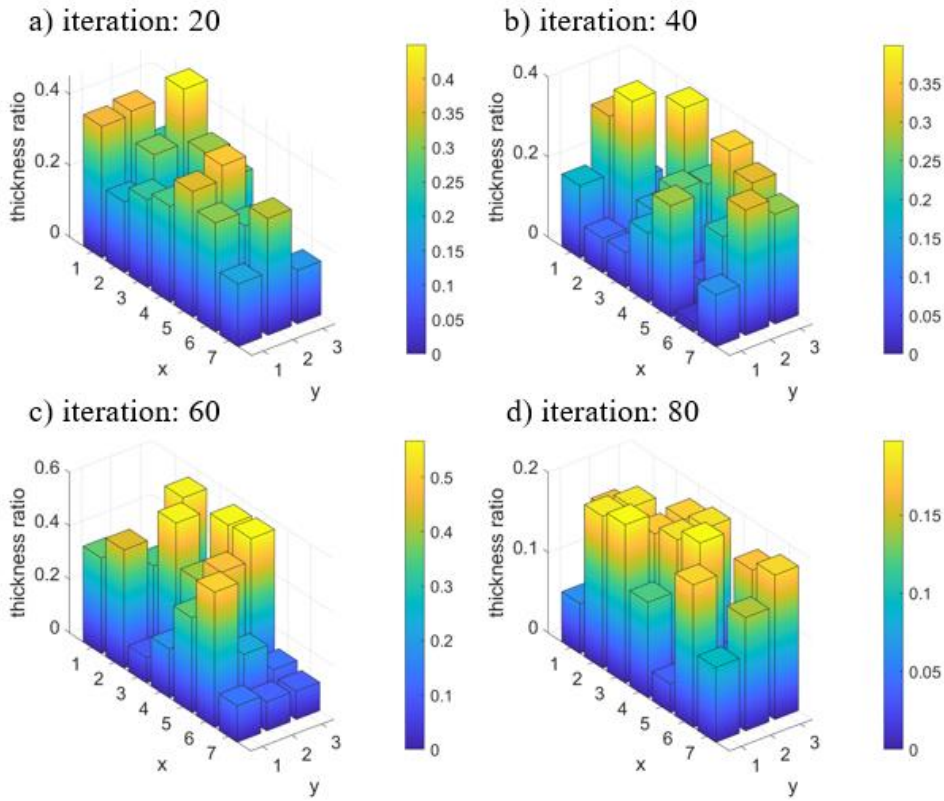

Figure 3.2 The identification process failed when the sensors were located at nodal points.

In the examples shown in Figs. 3.3 and 3.4, the aluminum plate model described in the previous example was examined, except with the primary selected sensor location data altered. The example of a perturbation applied to the eighth section is shown in Fig. 3.3. In Fig. 3.4, the sensor locations examined were the same as those examined in Fig. 3.3, except that the ninth section was perturbed. Both approaches appeared to search for the locations suitably, as shown in Fig. 3.3(b) and Fig. 3.4(c), after which the approaches searched for the thickness values of the corresponding elements in Fig. 3.3(d) and Fig. 3.4(d). Each initial thickness was determined by minimizing the residual error. As shown in Fig. 3.2, improper sensor locations lead the identification process to diverge. In Figs. 3.3 and 3.4, the detection for the location of the perturbation comes first in about 30 iterations and then identifies the amount of the perturbation next. Since other candidates are gone, it takes about 15 iterations to identify the exact value of the perturbation. The minimum residual error of each section and the initial thickness values were calculated as independent variables.

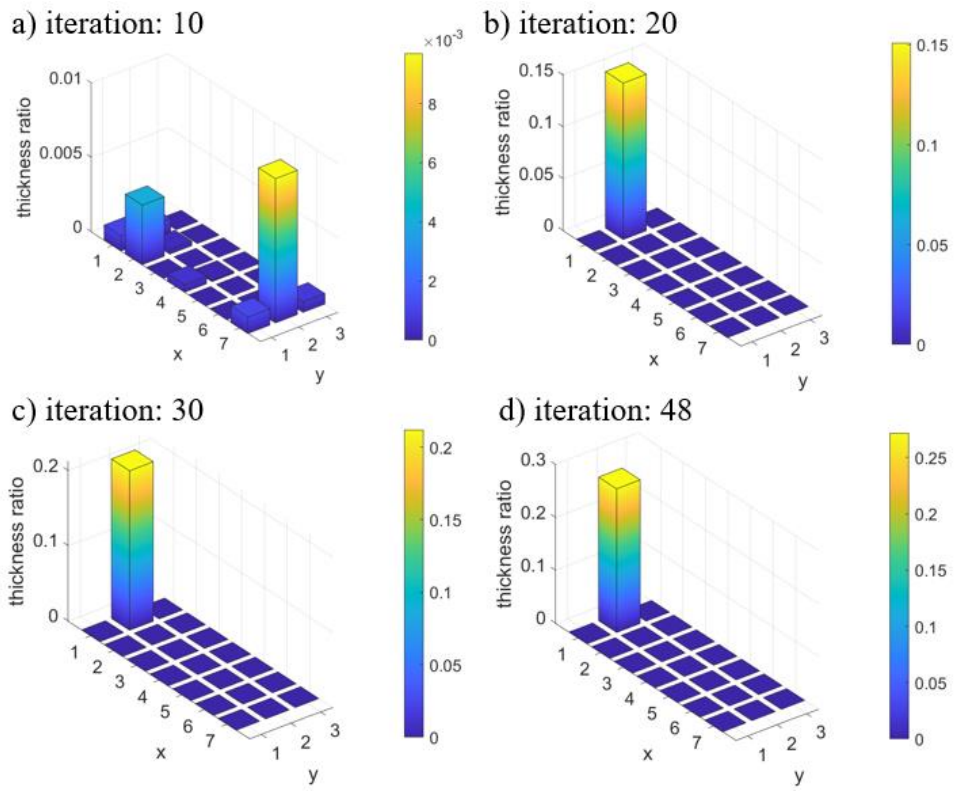

Figure 3.3 Accurate identification of the thickness perturbation in the eighth section.

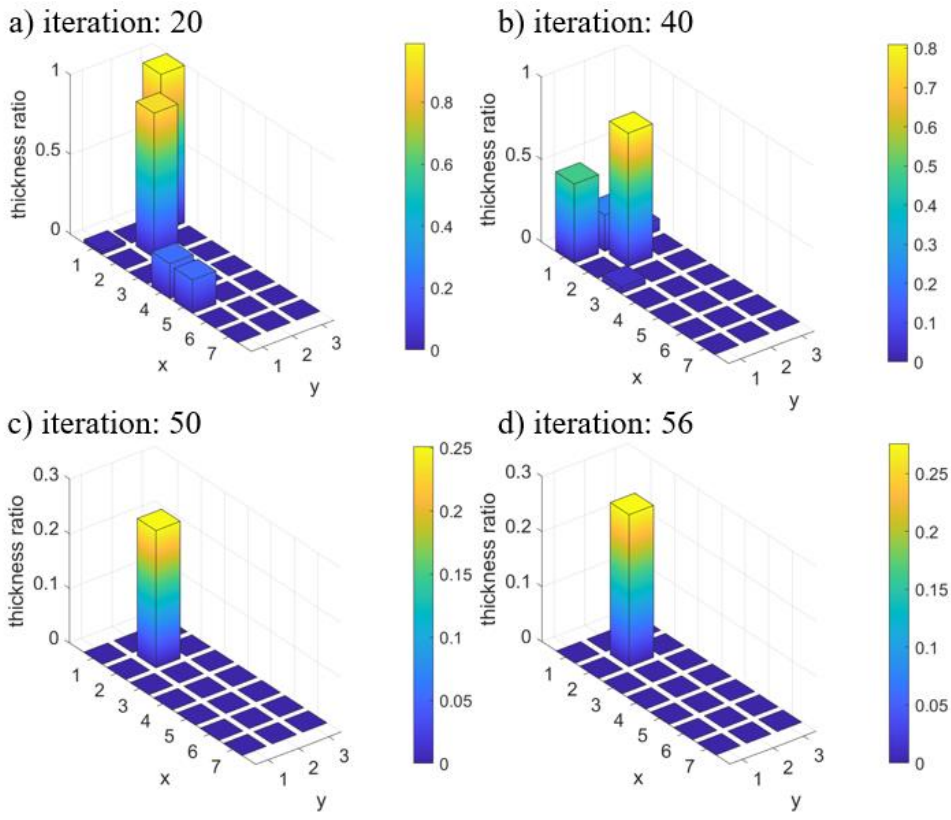

Figure 3.4 Accurate identification of the thickness perturbation in the ninth section.

It is necessary to upgrade the method to improve its convergence. Selecting a good sensor location provided an approach to gathering better experimental data. This effort is significant, because many types of system identification problems diverge or seek incorrect solutions as shown in Fig. 3.2. Table 3.1 lists the thickness ratio (th / th_0) and the error between the perturbed and identified models. The accuracy of the identification can be ascertained by the error compared to the target, which lies within 0.63% and 0.40%, respectively. Comparisons of the eigenvalues between the reference and perturbed models for the eighth and ninth sections are listed in Tables 3.2 and 3.3, respectively. The eigenvalues predicted by the identified model were in excellent agreement with those of the target. Changes in any region of the given structure appeared to be detectable using the proposed method.

Table 3.1 Identification results for the eighth and ninth sections.

	Perturbed	Identified	
Model		The eighth section	The ninth
Thickness ratio (th / th_0)	1.2666	1.2717	1.2759
Error	-	0.40%	0.63%

Table 3.2 Comparison of the eigenvalues for the eighth section.

Mode	Reference (λ)	Perturbed (λ')				
		Target	Experimental		Identified	
1	329.55	325.92	325.75	−0.05%	325.86	−0.02%
2	457.95	460.29	460.85	+0.12%	460.32	+0.01%
3	911.74	907.32	921.48	+1.56%	907.24	−0.01%
4	988.32	1005.4	1006.2	+0.08%	1005.7	+0.03%
5	1665.10	1705.2	1704.9	−0.02%	1705.8	+0.04%

Table 3.3 Comparison of the eigenvalues for the ninth section

Mode	Reference (λ)	Perturbed (λ')				
		Target	Experimental		Identified	
1	329.55	332.64	332.13	−0.15%	332.71	+0.02%
2	457.95	466.29	465.53	−0.16%	466.50	+0.05%
3	911.74	934.38	929.49	−0.52%	934.94	+0.06%
4	988.32	1023.2	1017.8	−0.53%	1024.2	+0.10%
5	1665.10	1701.9	1692.1	−0.58%	1703.0	+0.06%

For more verification, the modal assurance criterion (MAC) is defined as **[22, 35-36]**,

$$\mathrm{MAC} = \frac{\left|\{\boldsymbol{\varphi}'_t\}^T \{\boldsymbol{\varphi}'_i\}\right|^2}{\left(\{\boldsymbol{\varphi}'_t\}^T \{\boldsymbol{\varphi}'_t\}\right)\left(\{\boldsymbol{\varphi}'_i\}^T \{\boldsymbol{\varphi}'_i\}\right)}, \tag{3.14}$$

where $\boldsymbol{\varphi}'_t$ is the eigenvector for the target perturbation model and $\boldsymbol{\varphi}'_i$ is the eigenvector for the identified perturbation model. The perturbed thicknesses have been identified through the proposed method. It is important to confirm the accuracy of the eigenvectors as well as the accuracy of the eigenvalues. The accuracy of the eigenvectors using the MAC is shown in Table 3.4. If the value of the MAC is close to 1, a consistent correspondence is achieved. On the other hand, if the value is small, a poor resemblance between two modes is demonstrated. The mode shapes on the eighth and ninth sections were compared with those of the target. The perturbation of the thickness was found to be accurately identified. The accuracy of the eigenvalues is listed in Tables 3.2 and 3.3. Furthermore, the eigenvalues are summarized in Table 3.4. The MAC calculated directly with the experimental data at the sensor locations was not accurate. However, the MAC with the identified model is in excellent agreement with that of the target.

Table 3.4 Comparison of the MAC for the eighth and ninth sections

Mode	MAC for the eight section		MAC for the ninth section	
	Experimental	Identified	Experimental	Identified
1	0.9409	0.9998	0.9259	0.9998
2	0.9003	0.9992	0.8609	0.9997
3	0.5958	0.9965	0.4465	0.9928
4	0.6214	0.9667	0.6324	0.9547
5	0.4922	0.9450	0.4510	0.9304

Chapter 4.

A 2-dimensional convolution neural networks for system identification

4.1. Introduction

Structural model updating methods that use accurate measurements for structural system identification are critical for detecting structural changes. The reliability and accuracy of an entire structural model depends on the detection of structural changes. Many studies have attempted to improve the accuracy and efficiency of system identification approaches. Numerically designed models may be experimentally tested under various circumstances to increase model reliability. The model updating process is important for improving model accuracy by considering experimental data. The aim of this study is to improve the reliability of analytical numerical models by considering experimental models. In this study, a

system identification method was applied to update the parameters of a model of interest. The parameters corresponding to the experimental conditions were used to update the numerical model.

Several studies have attempted to improve the accuracy and efficiency of system identification by applying the degrees of freedom (DOFs)-based reduction method **[8-24]** and the inverse perturbation method (IPM) **[5-7]**. Experimental data were obtained from certain sensors positioned on the system. Experimental vibration data were restored to full finite element (FE) models by updating the numerical model using the reduction method. Previous methods were acceptable because the number of positions at which the experimental vibration data were gathered was less than the DOFs in the FE model **[1-4]**. These studies restored a full FE model that reflected the experimental model using the DOF-based reduction methods **[8-24]**. The restored model shape could be used to improve the accuracy of the numerical models. Specific sensor locations were selected using methods developed previously **[24]**. The transformation matrices in the DOFs-based reduction method enabled a comparison of the eigenvectors in the system identification and model updating methods.

The number of DOFs and parameters are significantly higher in a continuum structure compared to a discrete structure **[8-24]**. Reduction and inverse problem methods have been used to simplify the identification process and reduce the number of DOFs **[8-12]**. FE model accuracy relies on a high number of DOFs, and the accuracy of an FE model can be maintained by reasonably grouping the elements. The number of DOFs may be reduced using DOFs-based reduction methods while maintaining model accuracy **[8-12]**. Numerous structural system identification methodologies have been developed **[8-24]**. These methods tend to

be narrowly applicable to eigenvalue comparisons between simplified models and experimental systems, because distinct eigenvalues correspond to distinct structures **[1-3]**. Note that continuum structures are more complicated than discrete structures and have a variety of mode shapes. Structural differences, therefore, also correspond to eigenvector differences. Eigenvector comparisons are significant in structural system identification methods.

The most time-consuming steps of a model updating process are typically the iterative inverse problem identification steps. The transformation matrix used to restore experimental data to a full FE model must be updated at every iteration of the inverse problem. The calculation time may be minimized by pre-training an artificial neural network **[4, 69-75]**. FE model parameter selection and the application of perturbations determine the vibration data. Stainier et al. **[70]** introduced a model-free data-driven method by building a material database that could predict the responses of structures composed of that material. Identification methods using a convolutional neural network (CNN) were used to detect structural changes in a long steel girder bridge **[73]** and a frame model **[74]**. A wind turbine model was used to predict the effects of a mass added to a blade beam model **[71]** and blade delamination **[72]**. These updating methods saved calculation time and suggested approaches to real-time calculations **[75]**. The iterated improved reduced system (IIRS) was employed to overcome a lack of sensor information **[24]**. The updating calculation efficiency was improved using the system equivalent reduction-expansion process (SEREP) to restore the full numerical model. The CNN was used to improve training accuracy while maintaining the spatial information in the updating model. The number of DOFs of the FE model produced a large number of eigenvectors. A proper orthogonal

decomposition (POD) reduced the thousands of DOFs to a few coefficients. Minimizing the output data increased the efficiency of the CNN.

The objective of the present study was to explore an effective model updating method using the CNN. The updating calculation efficiency was improved by using the SEREP to restore the full eigenvectors of the numerical model when training the CNN. The output data could be minimized through the POD. The ANN showed accurate results in first few mode shape restorations, but the accuracy decreased as the complexity of the mode shape increased. The CNN preserved spatial information when trained using a database constructed from more than a thousand different mode shapes from different parameters of the numerical model. The IIRS was employed to overcome a lack of sensor information. Previous experimental and FE models of an aluminum plate (A6061-T6) developed using the sensor location selection method were employed to examine the efficiency and accuracy of the present CNN updating method.

4.2 The balance equation of the model updating method

The main object of the model updating method is to identify differences between a numerical model and an experimental model. The model is updated via structural system identification using precise experimental data. Previous experimental and FE models of an aluminum plate (A6061-T6) were used in this study (Fig. 4.1) **[24]**. The numerical model featured a uniform thickness across all elements of the plate. The experimental model, on the other hand, included a perturbation compared to the numerical model. The eigenvalue equations were expressed as

$$\mathbf{K}\boldsymbol{\varphi} = \lambda\mathbf{M}\boldsymbol{\varphi}, \tag{4.1}$$

$$\mathbf{K}'\boldsymbol{\varphi}' = \lambda'\mathbf{M}'\boldsymbol{\varphi}', \tag{4.2}$$

where $\mathbf{K}, \mathbf{M}$, and $\mathbf{K}', \mathbf{M}'$ are the numerical stiffness and mass matrices, and the experimental stiffness and mass matrices, respectively. Property changes in the elements were introduced by adjusting the components of the stiffness matrix $\mathbf{K}'$ and mass matrix $\mathbf{M}'$. The eigenvalues and eigenvectors of the numerical and experimental models were expressed as $\lambda, \boldsymbol{\varphi}$, and $\lambda', \boldsymbol{\varphi}'$, respectively. The numerical eigenvalues and eigenvectors were determined by numerical calculations, and the experimental eigenvalues and eigenvectors were determined using experimental vibration tests. Changes in the model properties were expressed using the FE matrices, so any property described using the equation could be selected as a parameter for the identification process.

4.2.1 The IPM method

Differences between the numerical and experimental models were minimized using the IPM by adjusting the chosen parameters. Model perturbations were achieved by minimizing the residual error $(\mathbf{R})$. The perturbed stiffness matrix was divided into the reference stiffness $(\mathbf{K})$ and the variations in the perturbed stiffness $(\Delta\mathbf{K})$, and the perturbed mass matrix was divided into the reference mass $(\mathbf{M})$ and the variation in the perturbed mass $(\Delta\mathbf{M})$,

$$\mathbf{R} = \mathbf{K}'\boldsymbol{\varphi}' - \lambda'\mathbf{M}'\boldsymbol{\varphi}'. \tag{4.3}$$

$$\mathbf{R} = (\mathbf{K} + \Delta\mathbf{K})\boldsymbol{\varphi}' - \lambda'(\mathbf{M} + \Delta\mathbf{M})\boldsymbol{\varphi}'. \tag{4.4}$$

The experimental eigenvalues and eigenvectors were applied to the numerical stiffness and mass matrices. The perturbation terms ($\Delta\mathbf{K}$ and $\Delta\mathbf{M}$) were varied by adjusting the parameters. The parameters that minimized the residual error represented the perturbed experimental model.

4.2.2 The DOF-based reduction method

The DOF-based reduction method was used to restore the full FE model with limited experimental data. The concept of the DOF-based reduction method was first introduced by Guyan **[8]**. The main idea underlying this method is that a few DOFs of a matrix can represent the whole matrix via a transformation matrix. An undamped mass–stiffness FE model could be decomposed into primary and secondary sets corresponding to the primary and secondary DOFs, respectively **[24]**,

$$\begin{bmatrix} \mathbf{M}_{pp} & \mathbf{M}_{ps} \\ \mathbf{M}_{sp} & \mathbf{M}_{ss} \end{bmatrix} \begin{Bmatrix} \ddot{\mathbf{u}}_p \\ \ddot{\mathbf{u}}_s \end{Bmatrix} + \begin{bmatrix} \mathbf{K}_{pp} & \mathbf{K}_{ps} \\ \mathbf{K}_{sp} & \mathbf{K}_{ss} \end{bmatrix} \begin{Bmatrix} \mathbf{u}_p \\ \mathbf{u}_s \end{Bmatrix} = \begin{Bmatrix} \mathbf{f}_p \\ \mathbf{f}_s \end{Bmatrix}, \tag{4.5}$$

where the subscript *p* indicates the primary DOFs and the subscript *s* indicates the secondary DOFs. The primary DOFs became the representative DOFs, which corresponded to the experimental sensor positions.

$$\mathbf{u} = \begin{Bmatrix} \mathbf{u}_p \\ \mathbf{u}_s \end{Bmatrix} = \begin{bmatrix} \mathbf{I} \\ -\mathbf{K}_{ss}^{-1}\mathbf{K}_{sp} \end{bmatrix} \{\mathbf{u}_p\} = \begin{bmatrix} \mathbf{I} \\ \mathbf{t}_G \end{bmatrix} \{\mathbf{u}_p\} = \mathbf{T}_G \mathbf{u}_p . \tag{4.6}$$

Through Eq. (4.6), the deformation of a full model was defined by the deformations of the primary DOFs and the Guyan transformation matrix $\mathbf{T}_G$,

where $\mathbf{T}_G$ gave accurate results in static problems but not in dynamic problems **[8]**. The transformation matrix accuracy was improved in various problems by O'Callahan **[9]** and Friswell *et al*. **[10]**.

$$\mathbf{u} = \begin{Bmatrix} \mathbf{u}_p \\ \mathbf{u}_s \end{Bmatrix} = \begin{bmatrix} \mathbf{I} \\ -(\mathbf{K}_{ss} - \lambda \mathbf{M}_{ss})^{-1}(\mathbf{K}_{sp} - \lambda \mathbf{M}_{sp}) \end{bmatrix} \{\mathbf{u}_p\} = \begin{bmatrix} \mathbf{I} \\ \mathbf{t}_G \end{bmatrix} \{\mathbf{u}_p\} = \mathbf{T}_G \mathbf{u}_p . \quad (4.7)$$

$$\begin{aligned} \mathbf{t}(\lambda) = & -\mathbf{K}_{ss}^{-1}\mathbf{K}_{sp} + \mathbf{K}_{ss}^{-1}(\mathbf{M}_{sp} - \mathbf{M}_{ss}\mathbf{K}_{ss}^{-1}\mathbf{K}_{sp})\lambda \\ & + \mathbf{K}_{ss}^{-1}\mathbf{M}_{ss}\left\{\mathbf{K}_{ss}^{-1}(\mathbf{M}_{sp} - \mathbf{M}_{ss}\mathbf{K}_{ss}^{-1}\mathbf{K}_{sp})\right\}\lambda^2 + O(\lambda^3), \end{aligned} \quad (4.8)$$

$$\mathbf{t}_{IRS} = \mathbf{t}_{IIRS}^{(1)} = -\mathbf{K}_{ss}^{-1}\mathbf{K}_{sp} + \mathbf{K}_{ss}^{-1}(\mathbf{M}_{sp} - \mathbf{M}_{ss}\mathbf{K}_{ss}^{-1}\mathbf{K}_{sp})\mathbf{M}_G^{-1}\mathbf{K}_G , \quad (4.9)$$

$$\mathbf{t}_{IIRS}^{(i)} = \mathbf{t}_G + \mathbf{K}_{ss}^{-1}\left(\mathbf{M}_{sp} + \mathbf{M}_{ss}\mathbf{t}_{IIRS}^{(i-1)}\right)\left(\mathbf{M}_{IIRS}^{(i-1)}\right)^{-1}\mathbf{K}_{IIRS}^{(i-1)} . \quad (4.10)$$

The improved reduced system (IRS) method, described in Eq. (4.9), was proposed as a more fundamental approach and was based on the Taylor series expansion in Eq. (4.8). This method predicted a natural frequency from Eq. (4.1), and the first and second terms of the Taylor series expansion were used to construct the transformation matrix. $\mathbf{M}_G$ and $\mathbf{K}_G$ are the reduced mass and stiffness matrices constructed using the Guyan method. The IRS transformation matrix in Eq. (4.9) turned out to be the first step of the iterated IRS (IIRS) transformation matrix **[10]**, in which the following updates were made:

$$\mathbf{K}_{IIRS}^{(i)} = \mathbf{K}_{pp} + \mathbf{K}_{ps}\mathbf{t}_{IIRS}^{(i-1)} + (\mathbf{t}_{IIRS}^{(i-1)})^T\mathbf{K}_{sp} + (\mathbf{t}_{IIRS}^{(i-1)})^T\mathbf{K}_{ss}\mathbf{t}_{IIRS}^{(i-1)} , \quad (4.11)$$

$$\mathbf{M}_{IIRS}^{(i)} = \mathbf{M}_{pp} + \mathbf{M}_{ps}\mathbf{t}_{IIRS}^{(i-1)} + (\mathbf{t}_{IIRS}^{(i-1)})^T\mathbf{M}_{sp} + (\mathbf{t}_{IIRS}^{(i-1)})^T\mathbf{M}_{ss}\mathbf{t}_{IIRS}^{(i-1)} . \quad (4.12)$$

A more accurate transformation matrix could be obtained using the inverse perturbation method (IPM), although this approach was time-consuming. To save

time, the system equivalent reduction-expansion process (SEREP) was used. Iterative application of the IPM was no longer needed in the SEREP, which reduced the calculation time significantly; however, this approach required equal numbers of mode shapes and primary DOFs. For this reason, the SEREP is not suitable in systems with numerous primary DOFs.

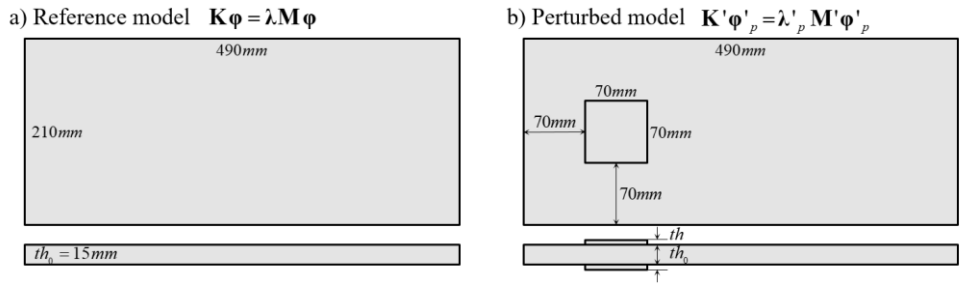

Figure 4.1 The aluminum plate model for model updating method.

4.2.3 Experimental data

The aluminum plate (A6061-T6) model in Sung et al. **[24]** was employed in the present study. A plate model with a uniform thickness was used as a reference model (Fig. 4.1a) for the numerical model. An experimental perturbed model was prepared (Fig. 4.1b). As shown in Fig. 4.1(a), the size of the plate model was 210 *mm* × 490 *mm* and the thickness of the plate model was 15 *mm*. The thickness variability in the plate model was selected as the study parameter here, and the perturbed thickness in the experimental model was used to update the numerical model. At the minimum residual error point, $\Delta\mathbf{K}$ and $\Delta\mathbf{M}$ represented the solution to the perturbation problem, and the obtained parameters could be applied when updating the reference model. The eigenvalues and eigenvectors of the experimental data collected at specific sensor positions were expressed as λ_p and $\boldsymbol{\varphi}_p$, respectively, with the subscript p identifying the primary DOFs.

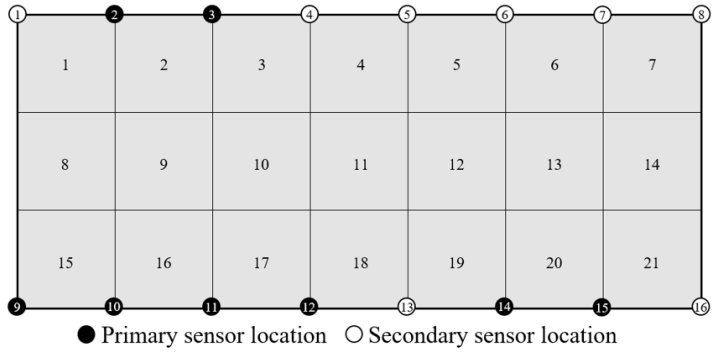

Figure 4.2 Aluminum plate (A6061-T6) divided into 21 sections. Each section was assigned a different thickness.

We assumed that the thickness remained uniform across each section. A vibration test was performed to obtain the eigenvalues and eigenvectors of the perturbed model. A reference aluminum plate model is presented in Fig. 4.2. The experimental perturbed model shown in Fig. 4.2 was fabricated using A6061-T6 aluminum. As shown in Fig. 4.2, the plate was divided into 21 same-sized sections. For example, if the thickness perturbation was applied in the 9^{th} section, Fig. 4.1(b) represented the perturbed model. The identification was explored using 21 sections to describe the same-sized square sections, as shown in Fig. 4.3(a). Each section was characterized by its own thickness parameter. The primary sensor positions in Fig. 4.2 were selected using the sensor location selection method **[24]**.

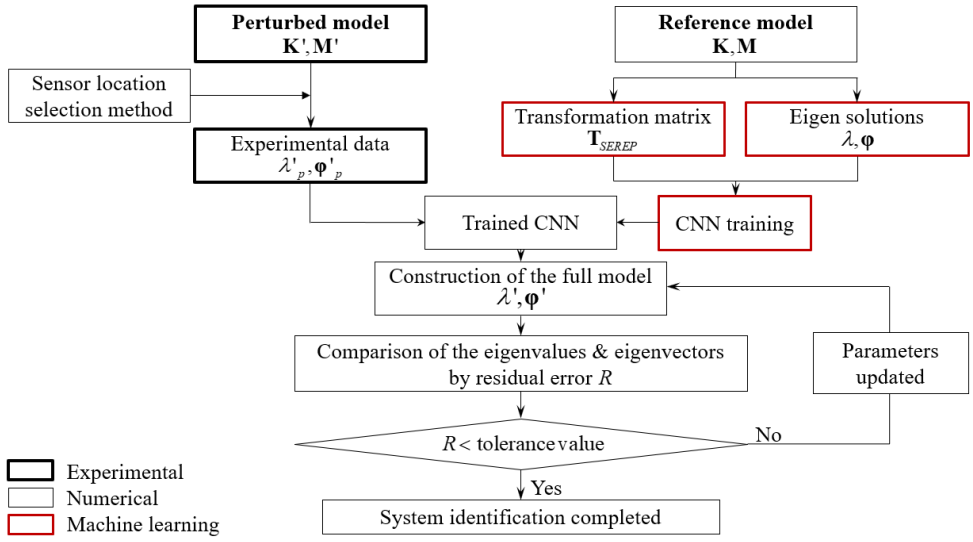

Figure 4.3 The algorithm of the model updating method

Figure 4.3 shows the flow chart of the algorithm. This approach was distinguished from previous algorithms in that machine learning was added to the identification method, highlighted in red in Fig. 4.3. The most time-consuming step involved the parameter updating process. Use of a trained convolution neural network (CNN) permitted the almost real-time construction of the transformation matrices. The system equivalent reduction-expansion process (SEREP) was employed to train the corresponding CNN. The eigenvectors of the secondary DOFs were needed to construct the transformation matrices from the SEREP. The numerical and experimental procedures, except for the CNN, are described in detail in Sung *et al*. **[24]**.

4.3 Convolutional neural network-based identification

4.3.1 The SEREP and POD

SEREP uses the mode shapes of the undamped analytical model by assuming the equation of motion of mass and stiffness matrix formation, $\mathbf{M}\ddot{x}+\mathbf{K}x=\mathbf{F}$. To reduce the size of the system to a smaller size with *p* modes or the *m* DOFs, where *p* is defined based on the expected bandwidth of the excitation and *m* is defined based on the number of DOFs that are acted upon by an external load, respectively. The number of retained coordinates is constrained to be equal to the number of retained mode shapes, and is chosen to be the larger of *p* or *m*. Then the coordinate vector can be partitioned into two parts, x_r and x_t, the retained and truncated coordinates, and reorganize the equation of undamped motion in the following equations:

$$\begin{bmatrix} M_{rr} & M_{rt} \\ M_{tr} & M_{tt} \end{bmatrix}\begin{bmatrix} \ddot{\mathbf{x}}_r \\ \ddot{\mathbf{x}}_t \end{bmatrix}+\begin{bmatrix} K_{rr} & K_{rt} \\ K_{tr} & K_{tt} \end{bmatrix}\begin{bmatrix} \mathbf{x}_r \\ \mathbf{x}_t \end{bmatrix}=\begin{bmatrix} \mathbf{F}_r \\ 0 \end{bmatrix}. \tag{4.16}$$

When considering the eigensolution for the mass normalized eigenvectors, $\Phi=[\Phi_{ar} \quad \Phi_{at}]$ where *r* and *t* stands for retained and truncated, and a represents that all coordinates are retained in the vector. The modes to be retained, Φ_{at}, is an $n\times(n-m)$ matrix.

$$\mathbf{x}=\begin{bmatrix} \mathbf{x}_r \\ \mathbf{x}_t \end{bmatrix}=\mathbf{\Phi r}=\begin{bmatrix}\Phi_{ar} & \Phi_{at}\end{bmatrix}\begin{bmatrix} \mathbf{r}_r \\ \mathbf{r}_t \end{bmatrix}=\begin{bmatrix} \Phi_{rr} & \Phi_{rt} \\ \Phi_{tr} & \Phi_{tt} \end{bmatrix}\begin{bmatrix} \mathbf{r}_r \\ \mathbf{r}_t \end{bmatrix}, \tag{4.17}$$

$$\Phi^T=\begin{bmatrix}\Phi_{ar} & \Phi_{at}\end{bmatrix}^T, \tag{4.18}$$

$$I\ddot{\mathbf{r}} + \lambda\mathbf{r} = \Phi^T\mathbf{F}, \tag{4.19}$$

$$\begin{bmatrix} \Phi_{ar}^T \\ \Phi_{at}^T \end{bmatrix} \begin{bmatrix} M_{rr} & M_{rt} \\ M_{tr} & M_{tt} \end{bmatrix} \begin{bmatrix} \Phi_{ar} & \Phi_{at} \end{bmatrix} = \begin{bmatrix} \Phi_{ar}^T M \Phi_{ar} & \Phi_{ar}^T M \Phi_{at} \\ \Phi_{at}^T M \Phi_{ar} & \Phi_{at}^T M \Phi_{at} \end{bmatrix} = \begin{bmatrix} I_r & \\ & I_t \end{bmatrix}, \tag{4.20}$$

$$\begin{bmatrix} \Phi_{ar}^T \\ \Phi_{at}^T \end{bmatrix} \begin{bmatrix} K_{rr} & K_{rt} \\ K_{tr} & K_{tt} \end{bmatrix} \begin{bmatrix} \Phi_{ar} & \Phi_{at} \end{bmatrix} = \begin{bmatrix} \Phi_{ar}^T K \Phi_{ar} & \Phi_{ar}^T K \Phi_{at} \\ \Phi_{at}^T K \Phi_{ar} & \Phi_{at}^T K \Phi_{at} \end{bmatrix} = \begin{bmatrix} \Lambda_r & \\ & \Lambda_t \end{bmatrix}, \tag{4.21}$$

Substituting Eq. (4.17) into Eq. (4.18) and pre-multiplying the result by Eq. (4.18) yielded the equations of motion in the modal coordinates, as shown in Eq. (4.19), with the transformed mass and stiffness matrices, Eq. (4.20) and Eq. (4.21), respectively. Equations (4.17) through Eq. (4.21) yielded the motion equation in the reduced deformation vectors, expressed as

$$\Phi_{rr}^{-1^T}\Phi_{ar}^T M \Phi_{ar}\Phi_{rr}^{-1}\ddot{\mathbf{x}}_r + \Phi_{rr}^{-1^T}\Phi_{ar}^T K \Phi_{ar}\Phi_{rr}^{-1}\mathbf{x}_r = \Phi_{rr}^{-1^T}\Phi_{ar}^T\mathbf{F}, \tag{4.22}$$

The transformation matrix of the SEREP was defined as

$$T_{SEREP} = \Phi_{ar}\Phi_{rr}^{-1} = \begin{bmatrix} \Phi_{rr} \\ \Phi_{tr} \end{bmatrix}\Phi_{rr}^{-1} = \begin{bmatrix} I \\ \Phi_{tr}\Phi_{rr}^{-1} \end{bmatrix}, \tag{4.23}$$

$$\tilde{\mathbf{M}}\ddot{x}_r + \tilde{\mathbf{C}}\dot{x}_r + \tilde{\mathbf{K}}x_r = \tilde{\mathbf{F}}, \tag{4.24}$$

where $\tilde{\mathbf{M}} = \mathbf{T}^T\mathbf{M}\mathbf{T}, \tilde{\mathbf{C}} = \mathbf{T}^T\mathbf{C}\mathbf{T}, \tilde{\mathbf{K}} = \mathbf{T}^T\mathbf{K}\mathbf{T}$ and $\tilde{\mathbf{F}} = \mathbf{T}^T\mathbf{F}$. As in Eq. (4.23), the transformation matrix constructed through SEREP can be expressed with eigenvectors of the selected DOFs. The transformation matrix construction using SEREP will be applied in advanced system identification process to improve the calculation efficiency.

The main idea of the POD was to identify a set of ordered orthonormal basis vectors in a subspace without loss of generality. In such a subspace, a random vector R^m would assume a value such that the samples in the sample space can be expressed optimally. The samples were selected using the first *l* basis vectors. The mean square errors (MSE) could be defined as a measure for the optimal problem, i.e.,

$$E\left\{\left\|x-x(l)\right\|^2\right\} \le E\left\{\left\|x-\hat{x}(l)\right\|^2\right\}, \tag{4.25}$$

where *x*(*l*) is the approximate expression of a random vector *x* using the first *l* basis vectors of the undetermined set of orthonormal basis vectors and $\hat{x}(l)$ is the approximate expression of *x* using arbitrary *l* basis vectors in R^m. Assume that $x \in R^m$ is a random vector and $\{\phi_i\}_{i=1}^m$ is a set of arbitrary orthonormal basis vectors: then *x* can be expressed as

$$x = \sum_{i=1}^{m} \alpha_i \phi_i = \Phi\alpha, \tag{4.26}$$

where $\alpha_i = \phi_i^T x\,(i=1,2,\ldots,m), \quad \alpha = (\alpha_1,\alpha_2,\ldots,\alpha_m)^T$, and $\Phi = [\phi_1,\phi_2,\ldots,\phi_m]$. The objective of the POD was to find a set of basis vectors that satisfied the following extreme value problem:

$$\begin{aligned} &\min_{\phi_i} \varepsilon^2(l) = E\left\{\left\|x-x(l)\right\|^2\right\} \\ &\text{s.t.}\,\phi_i^T\phi_j = \delta_{ij} \quad i,j=1,2,\ldots,m, \end{aligned} \tag{4.27}$$

where $x(l) = \sum_{i=1}^{l} \alpha_i\phi_i\ (l \le m)$. The output data set of this study is the

eigenvector information of a FE model. A model of 6600 DOFs was adopted as an example in this study, and more than a hundred perturbations in each mode shape were gathered. Maximizing the efficiency of such a large system using CNN training might have been computationally intensive. In the present study, the POD enabled the eigenvector data set to be minimized to about 40 POD coefficients. The number of POD coefficients was selected by considering the energy percentage of the eigenvalues. The physical meaning of the eigenvalues, , obtained by solving eigen-problem is how much the mode participates in the system response. Note that the eigenvalues assumed a descending order,

$$\lambda_1 \geq \lambda_2 \geq \cdots \geq \lambda_N \geq 0. \tag{4.28}$$

The total energy of the system represents the summation of the eigenvalues. The energy percentage, $E(k)$, captured by the 1st mode to the *k*-th mode can be expressed as

$$E(k) = \frac{\sum_{j=1}^{k} \lambda_j}{\sum_{i=1}^{N} \lambda_i}. \tag{4.29}$$

A higher energy percentage corresponded to a higher POD accuracy. The number of POD modes was determined by maintaining the energy percentage above 99.9999%, which ensured data quality. The number of POD coefficients that satisfied the energy percentage criterion was not fixed.

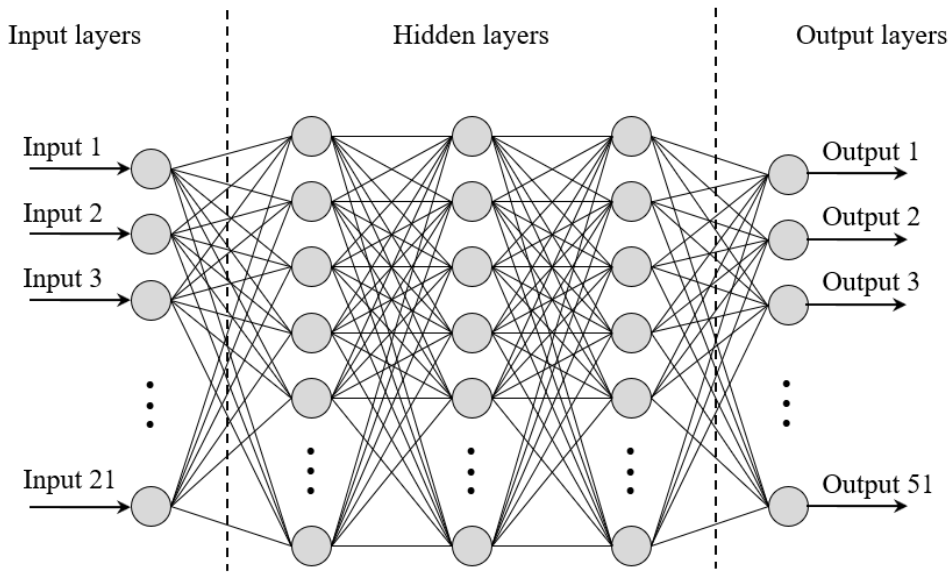

Figure 4.4 ANN algorithm map for given problem.

4.3.2 The 2D-CNN

The input data of the artificial NN was limited to a one-dimensional (1D) form, as shown in Fig. 4.4, and comprised a single vector in a fully connected layer. The data present in the colored photographs corresponded to three-dimensional information, encoded in RGB (red, green and blue layers). Training a fully connected NN using photographic data required flattening the 3D photo data into 1D data, and spatial information was inevitably lost. In a word, artificial NNs are limited in their ability to extract features and improve model accuracy due to a lack of information (loss of spatial information). By contrast, convolutional neural networks (CNNs) can be trained while maintaining spatial information. CNNs differ from general NNs in the following ways: (i) CNNs maintain the shape of input/output data in each layer. (ii) CNNs efficiently recognize the characteristics of adjacent images while maintaining spatial information. (iii) CNNs can extract features and learn from images using multiple kernels (also called filters). (iv) CNNs pool layers to collect and enhance the characteristics of the extracted image (the pooled layer is an optional layer). (v) Because the kernel is used as a shared parameter, few learning parameters are required in CNNs compared to general NNs.

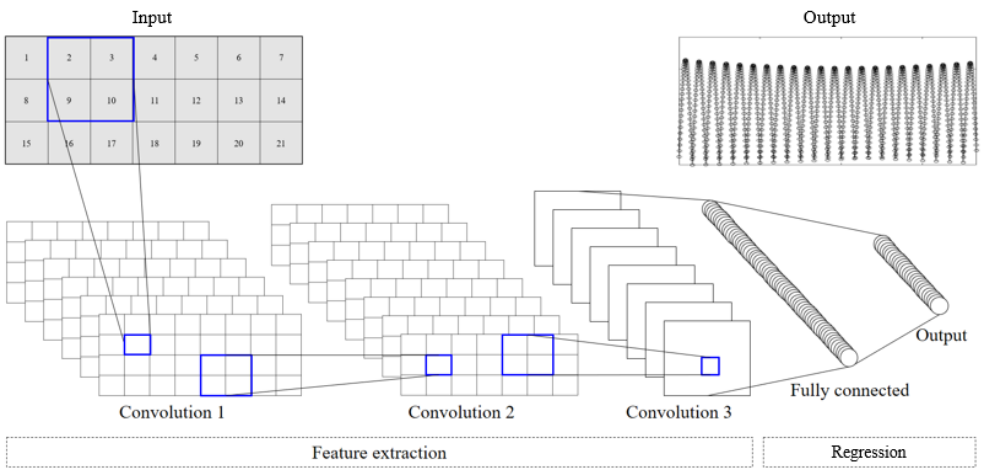

Figure 4.5 CNN algorithm map for given problem.

The CNN could be divided into parts that extracted the features of an image and parts that classified the image, as shown in Fig. 4.5. The feature extraction area consisted of multiple layers of the convolution layer. The convolution layer was an essential element that reflected the activation function after applying a kernel to the input data. The CNN training process produced a fully connected layer for classifying images using the same process as was used in the artificial NN (Fig. 4.4). A flattened layer was positioned between the part that extracted the features of the image and the part that classified the image, rendering image data as an array. Image feature extraction was achieved once the kernel traversed the input data, calculated the composite product, and created a feature map using the calculated results. In the convolution layer, the shape of the output data changed depending on the kernel size, application of stride, application of padding, or the maximum pooling size.

The convolution operation was applied to 2D input data using $I^1(m \times m)$, with one kernel, $\omega^1(n \times n)$.

$$F_{ij}^1 = \sum_{a=1}^{n} \sum_{b=1}^{n} \omega_{ab}^1 I_{(i+a-1)(j+b-1)}^1 \tag{4.30}$$

A feature map, $F^1((m-n+1) \times (m-n+1))$, was created from the results of convolution processing. Every pixel in the image corresponded to a real number. Natural colors expressed in colored photographs provided 3D data in which each pixel was represented by three RGB real numbers. A colored image consisted of three channels. On the other hand, a black-and-white photograph that expressed only black and white contrast was composed of one 2D data channel. The thickness perturbations in a plate model could be trained using black-and-white photographs.

One or more kernels were applied to the input data flowing into the convolution layer. One kernel became the channel of a feature map. The application of n kernels to a convolution layer produced output data with n channels. Kernels are commonly used to find the characteristics of a model. Kernels are usually defined as square $(n \times n)$ matrices. The target of CNN learning is a kernel. As shown in Fig. 4.6, input data were traversed at a specified interval, and the products of each channel were combined. The sum of the products of all channels formed a feature map. The kernel created a feature map by multiplying the kernel and the entire input data while moving at a specified interval. The specified interval that traversed the kernel was called the stride. A stride set to 2 resulted in a kernel calculating the composite product by moving 2 spaces. The input data produced one feature map per kernel, regardless of the number of channels. Multiple kernels of the same size could be applied to one convolution layer to create one corresponding feature map.

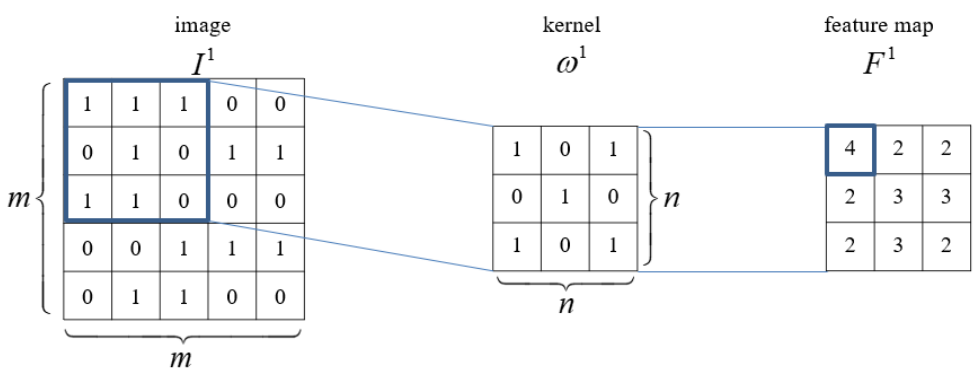

Figure 4.6 CNN feature map creation.

The kernel traversed the input data of a convolution layer, and the output created through the convolution was called the feature map or activation map. The feature map comprised a matrix created by calculating the composite product. The feature map was the result of applying the active function to the feature map matrix. In other words, the final output result of the convolution layer was the feature map. The feature map was smaller than the input data as a result of the kernel's action, given the stride, on a convolution layer. Padding prevented the output data of the convolution layer from shrinking. Padding involved adding a specified number of pixels with a specific value, usually zero.

4.4 Experimental examples

The two most time-consuming steps in system identification are the eigensolution step and the transformation matrix construction step **[71]**. A CNN can improve the calculation efficiency in the eigensolution part. The eigenvalues and eigenvectors obtained from a full FE model have more than a thousand DOFs under each perturbed condition. The restored mode shapes of each case can be trained using a CNN. The transformation matrices of each perturbed condition are required for identification, and SEREP is useful in this stage. Experimental eigenvector data can be restored to a full eigenvector by multiplying the transformation matrices constructed using the SEREP. An equal number of eigenmodes and primary DOFs should be used in the reduction method to determine the transformation matrices using the SEREP. For example, if ten positions in a model are selected as the primary DOFs, the SEREP requires ten eigenmodes to construct a transformation matrix. The transformation matrices were restored using the eigensolution constructed via the SEREP.

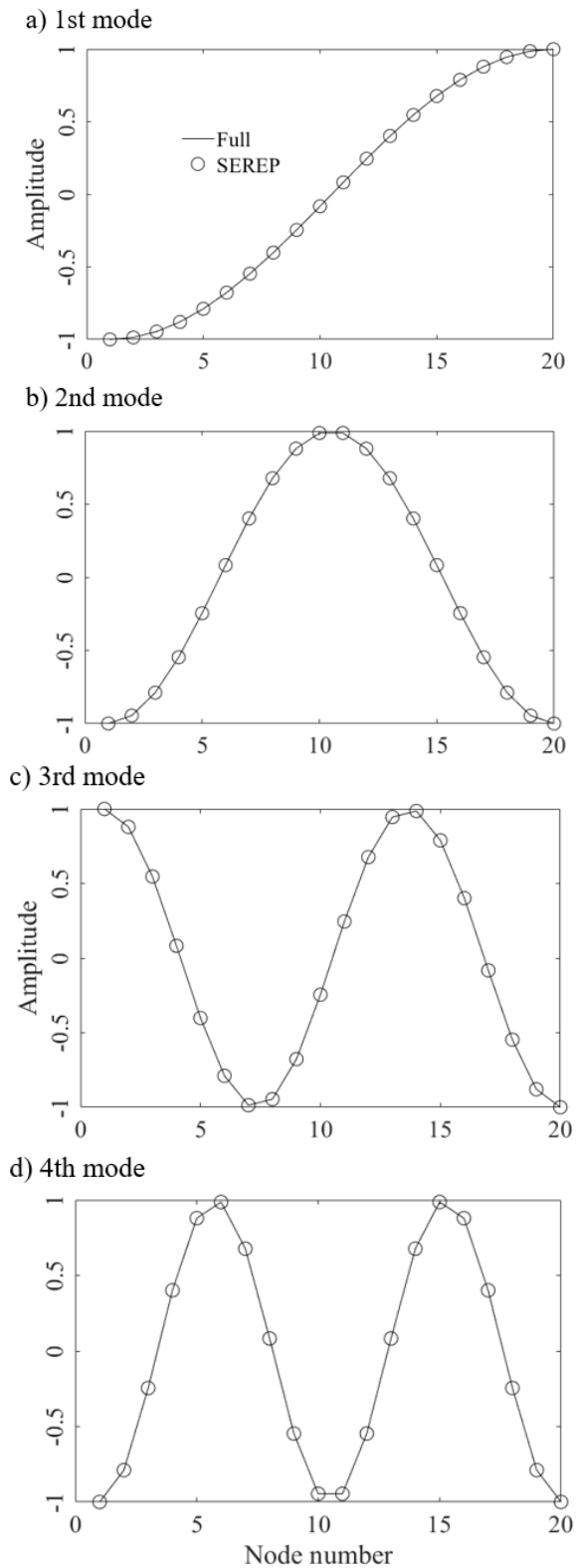

Figure 4.7 Comparison of the SEREP and full eigen solution mode shapes (1D beam).

Before proceeding further, the accuracy of the two methods must be assessed. A one-dimensional beam model was used for this assessment, and the results are shown in Fig. 4.8. Four mode shapes provided by the SEREP are compared to those provided by the full FE calculation. As shown, excellent agreement between the two methods was obtained. The maximum error was less than 5.64e–14, indicating that the transformation matrices constructed by the SEREP provided accurate results. In the event that the number of primary DOFs increases in the SEREP, the number of mode shapes must also increase.

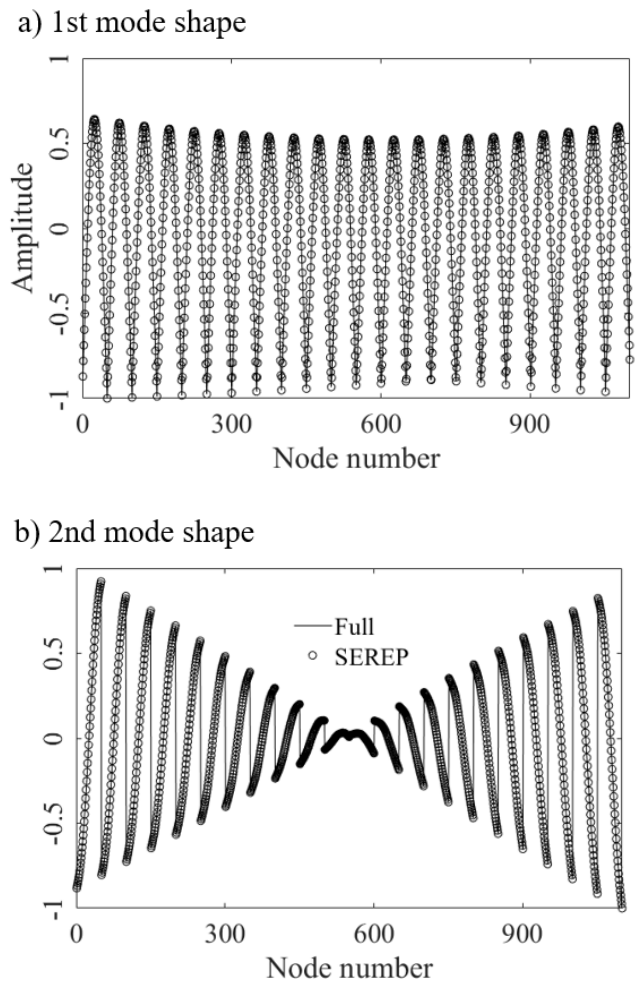

Figure 4.8 Comparison of the SEREP and full calculated mode shapes (plate).

Next, the plate model was applied given a selection of 8 sensor positions **[24]**. The first two mode shapes are shown in Fig. 8. As the number of primary DOFs was eight, eight mode shapes were employed to solve the problem. The maximum error was less than 4.043e-12. As shown previously, the transformation matrices constructed using the SEREP were in excellent agreement with those obtained from the full calculation. If the present CNN could provide the accurate mode shapes needed to construct the transformation matrices, the accuracy of the SEREP would be fully satisfied.

Table 4.1 The POD reduction of output (eigenvector) for CNN training.

Mode shape	1st	2nd	3rd	4th	5th	6th	7th	8th
Original vector size	1100	1100	1100	1100	1100	1100	1100	1100
Reduced vector size	51	54	59	59	63	63	65	63
Reduction ratio (%)	4.64	4.91	5.36	5.36	5.73	5.73	5.91	5.73
Mean element error (%)	6.6e-6	8.9e-6	4.2e-6	3.4e-4	5.5e-6	2.6e-4	1.8e-4	1.6e-5

As mentioned above, the POD was employed to minimize the size of the CNN output data. The plate model used in this study featured 6600 DOFs. Because the vibrations occurred only along the z-axis, only 1100 nodes along the z-axis could be selected from the 6-DOF nodes. It was still necessary to reduce the size of the output data to accurately train the CNN. Applying the POD to the training output data, which represented the eigenvector, reduced the POD coefficients and modes, as shown in Eq. (26). Errors at this stage were minimized by selecting a sufficient number of POD coefficients. The POD coefficients and modes were selected separately in each eigenmode. As shown in Table 4.1, 1100 vectors for each case were reduced to 50–65 vectors. A 5% reduction ratio yielded relatively small errors, indicating accurate restoration. The size of the reduced vector, which indicated the number of POD coefficients, differed in each mode. The number of POD modes was chosen by maintaining the POD energy percentage above 99.9999%.

In the next step, the SEREP and POD were simultaneously applied in concert with the CNN. The main goal of this study was to gather the eigenvalues and eigenvectors of a perturbed plate model under various perturbation cases. The gathered eigenvectors were then used to train the CNN; however, the DOFs of the plate model were too numerous to efficiently train a CNN. Herein, we developed a high-quality dataset for CNN training. The SEREP was used to minimize the DOFs during training. The SEREP transformation matrices required an equal number of mode shapes and primary DOFs. In the present study, eight mode shapes were gathered to train the CNN using a selection of eight sensor positions. Perturbation of the plate model was expressed using 21 vectors by changing the thickness at a specific position. The output data were expressed using the POD coefficients.

The present CNN was validated by comparing the basic conditions of the full eigensolution with those of the CNN. For validation, the modal assurance criterion (MAC) was defined as **[36]**

$$\mathrm{MAC} = \frac{\left|\{\boldsymbol{\varphi}'_t\}^T \{\boldsymbol{\varphi}'_i\}\right|^2}{\left(\{\boldsymbol{\varphi}'_t\}^T \{\boldsymbol{\varphi}'_t\}\right)\left(\{\boldsymbol{\varphi}'_i\}^T \{\boldsymbol{\varphi}'_i\}\right)}, \tag{4.32}$$

where $\boldsymbol{\varphi}'_t$ is the eigenvector for the target perturbation model and $\boldsymbol{\varphi}'_i$ is the eigenvector for the identified perturbation model. The errors of the eigenvalues fell within about 1%, and the MAC value of the eigenvectors exceeded 0.998. The calculation times were compared to determine the efficiency. As shown in Table 4.2, 3000 seconds were required to set up the CNN, and this time was called the off-line calculation time. This additional off-line calculation time appears to be inefficient; however, the off-line calculation was required only once. Because the function was constructed, the on-line calculation time was 200 times faster than that of the full calculation time. Identification using the IPM required a repetitive task, which significantly degraded the efficiency. The calculation times required of each method are compared in Tables 4.2 and 4.3. It is exciting to see that the calculation time of the CNN was about 160 times faster than that of the full calculation.

Table 4.2 Data loading and training time (*off-line*).

	Full	CNN
File load time	-	0.81 *sec*
Make function time	-	11 *sec*

Table 4.3 The calculation time comparison of the trained function (*on-line*).

Iterations	Iteration: 1		Iteration: 20		Iteration: 100	
	Full	CNN	Full	CNN	Full	CNN
On-line calculation	19.8 *sec*	0.12 *sec*	197.6 *sec*	1.19 *sec*	1976.4 *sec*	11.90 *sec*

In the present CNN, the widely used Levenberg–Marquardt (LM) back-propagation training algorithm and Adam (Adaptive moment estimation) optimizer were adopted to carry out CNN learning by minimizing a predefined error function formulated as the MSE between the network outputs and the actual values corresponding to the given set of input vectors. As a result, an optimal set of weights was obtained. The identification of a true optimal combination can be very time consuming, and some novel methods have been proposed in an attempt to tackle this problem. Currently, a trial procedure is commonly applied to the design of a CNN topology. In fact, it has been shown that a network with only one hidden layer suffices to approximate a large spectrum of complex functions; therefore, the effort required to identify a desirable network design can be considerably reduced by using just two or three hidden layers.

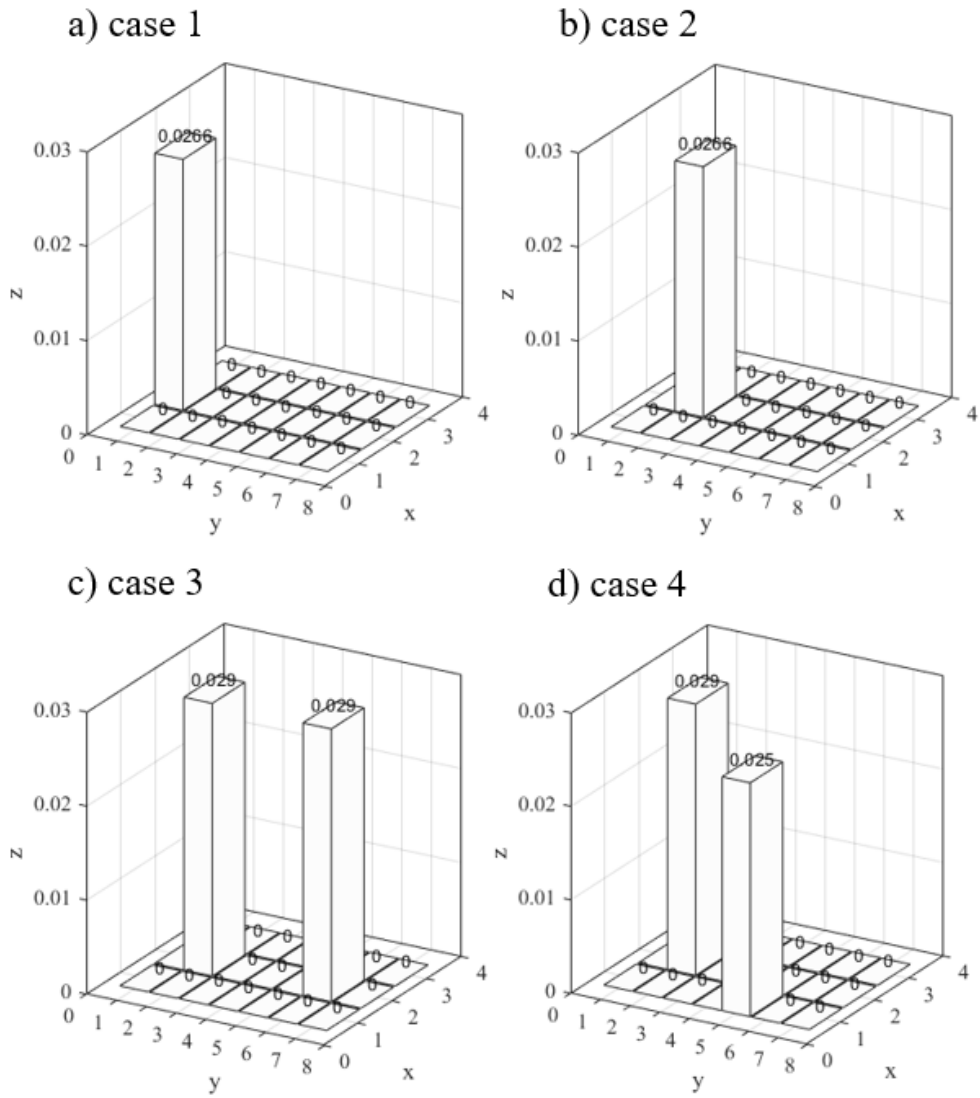

Figure 4.9 The plate model identification cases for validation.

This study used 21 divided sections, corresponding to the number of regions having uniform thicknesses. Each section changed thickness separately. Four perturbation cases are shown in Fig. 4.9: two single perturbations (Figs. 4.9(a) and 9(b)) and two double perturbations (Figs. 4.10(c) and 4.10(d)). The results of the CNN are shown in the following figures and tables. The CNN was trained using 8 mode shapes (with the highest vibration energy) for 251 different thickness cases (from 0.015 m to 0.030 m) across all 21 sections, as shown in Fig. 4.2.

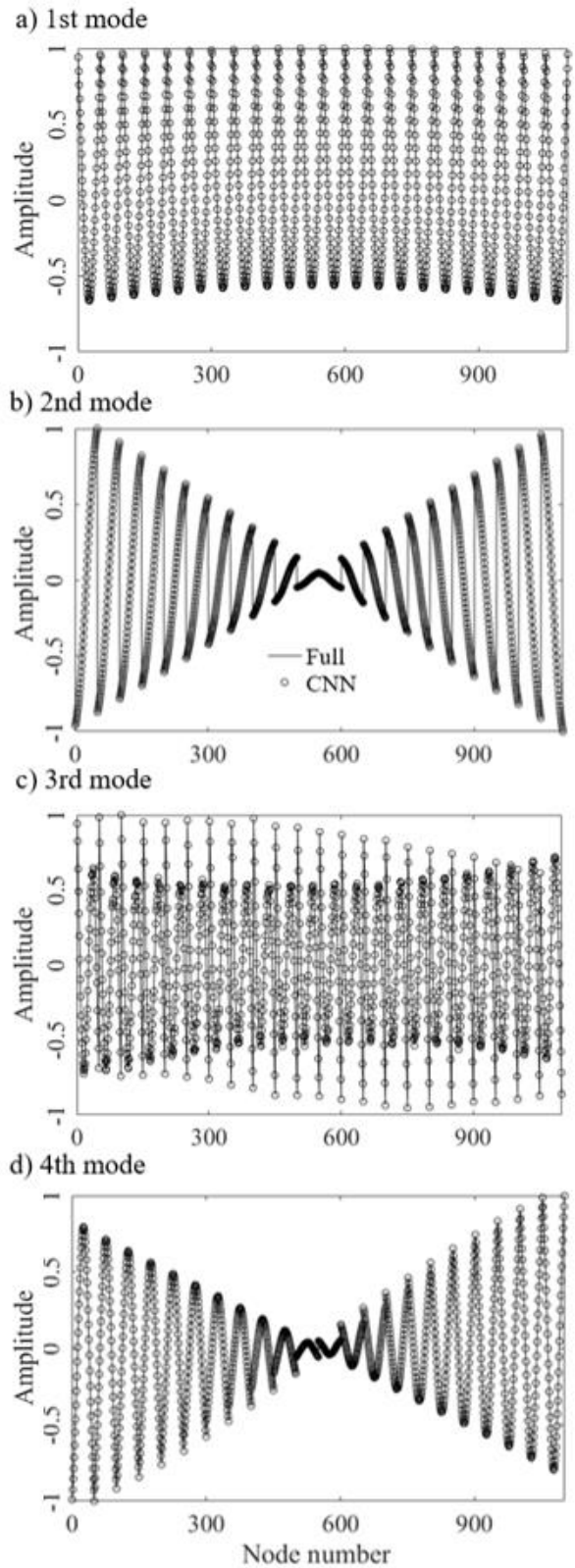

Figure 4.10 Comparison of the CNNID with SEREP and full calculated mode shapes (1st to 4th) of aluminum plate model (case 1).

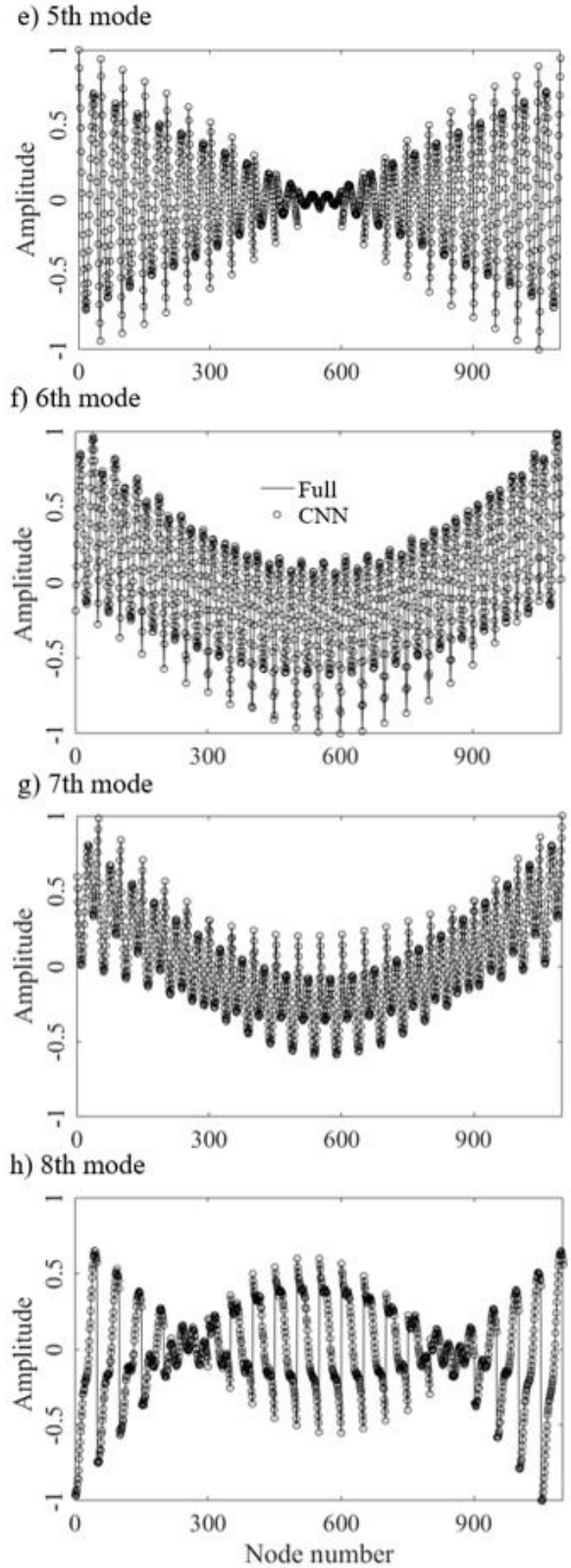

Figure 4.11 Comparison of the CNNID with SEREP and full calculated mode shapes (5th to 8th) of aluminum plate model (case 1).

Table 4.4 MAC value comparison of full eigen solution versus CNN.

Mode	1st	2nd	3rd	4th	5th	6th	7th	8th
case 1	0.998	0.999	0.995	0.999	0.999	0.997	0.996	0.999
case 2	0.999	0.999	0.996	0.999	0.998	0.995	0.995	0.996
case 3	0.999	0.999	0.995	0.996	0.982	0.981	0.984	0.937
case 4	0.998	0.999	0.996	0.996	0.989	0.992	0.973	0.939

Table 4.5 Calculation time comparison of full eigen solution versus CNN.

Mode	Full	CNN	Improvement
case 1	1201 *sec*	13.2 *sec*	90.9 times faster
case 2	1411 *sec*	14.2 *sec*	99.4 times faster
case 3	-	15.5 *sec*	-
case 4	-	14.9 *sec*	-

Figures 4.10 and 4.11 show the eight mode shapes used in the model updating process. The solid line and circle represent the full FE calculation and the CNN, respectively. The MAC values of the updated model are compared in Table 4.4. The CNN calculation time was significantly lower than the full FE calculation time, and the accuracy was maintained, as shown in Table 4.5. Because the calculations of transformation matrices and eigenproblems were replaced by the CNN, the calculation was more than 80 times faster than the full FE calculation. Experimental data were employed in the identification process in cases 1 and 2, and numerical data were employed in cases 3 and 4. Other cases were validated to confirm the performance of the present CNN method. We found that the identification process worked well in the presence of double perturbations by using the CNN in single perturbations.

A method of structural system identification using a convolutional neural network (CNN) was developed and validated using experimental and numerical examples. A variety of structural system identification methods have been constructed and applied to model updating, but these methods are limited by their large calculation time requirements. The computational demand arises mainly from iterations in the finite element model restoration. In the present study, these limitations were resolved by using the system equivalent reduction-expansion process (SEREP) in concert with the proper orthogonal decomposition (POD). The SEREP, a type of degree of freedom-based reduction method, was employed to construct a full model of the perturbed plate model. The significance of the SEREP was highlighted in the restoration process because it did not require iterations and it preserved the computational accuracy. The SEREP need for a large number of eigenvectors was addressed using a CNN. The output data could be minimized

through the POD. The SEREP was employed to overcome the sensor's lack of information. Previous experimental and finite element models of an aluminum plate (A6061-T6) using a sensor location selection method were employed to examine the efficiency and accuracy of the CNN. Training the CNN significantly reduced the calculation time. The accuracy of the SEREP was validated using a simple beam problem. The CNN maintained spatial information when trained by the database constructed from more than a thousand different mode shapes based on different numerical model parameters. The present updating method using the CNN could be used to minimize the computational time and increase the identification convergence.

Chapter 5.

A model updating for complex models

5.1 The model updating and digital twin

A model updating can be an effective methodology for a digital twin method. The digital twin is a digital replica of a living or non-living physical entity. Digital twin refers to a digital replica of potential and actual physical assets (physical twin), processes, people, places, systems and devices that can be used for various purposes. However, in mechanical industries, the object of the digital twin may be the structural models. The digital twin concept consists of three distinct parts: the physical product, the digital/virtual product, and connections between the two products. The connections between the physical product and the digital/virtual product is data that flows from the physical product to the digital/virtual product and information that is available from the digital/virtual product to the physical environment. Previously introduced structural system identification and model

updating methods can be completed and integrated through the digital twin concept. The digital twins in the mechanical industries are implemented by using existing data in order to facilitate processes and reduce marginal costs. Currently, mechanical designers expand the existing physical materiality by incorporating software-based digital abilities. A specific example of digital twin technology in the automotive industry is where automotive engineers use digital twin technology in combination with the firm's analytical tool in order to analyze how a specific car is driven. In doing so, they can suggest incorporating new features in the car that can reduce car accidents on the road, which was previously not possible in such a short time frame.

The application field of digital twin will be endless even in mechanical engineering, but in this study, the scope of the digital twin is the FE model simplification by updating properties that reflect the real model. To improve the experiment and analysis accuracy, several methods were introduced previously. The machine learning process is applied to enable the real-time calculation. The methods were applied to simple examples and were validated. In this chapter, the introduced methods are applied to tank bracket model. The methods are validated in more complex model and also the assembly problems are discussed.

5.2 A complex model example

5.2.1 The tank bracket model

Through previous studies, the shell elements for plate model were employed for the model updating method. The thicknesses of each element were the interest of the process. The mode shapes change due to the thickness change of the plate model

indicated the identification. In this chapter, more complex model will be introduced using the method that were introduced previously. The model that is applied here for validation is a tank bracket model in commercial trucks. These brackets connect the gas tank to the main frame of the truck. Each part of the model should be tested to identify the FE model. Each selected parameter for the model will be updated to improve the accuracy of the FE model. The updated parts of the model can be assembled by connecting boundary conditions. The contact properties and assembly properties can be the updating parameters in the assembly problems.

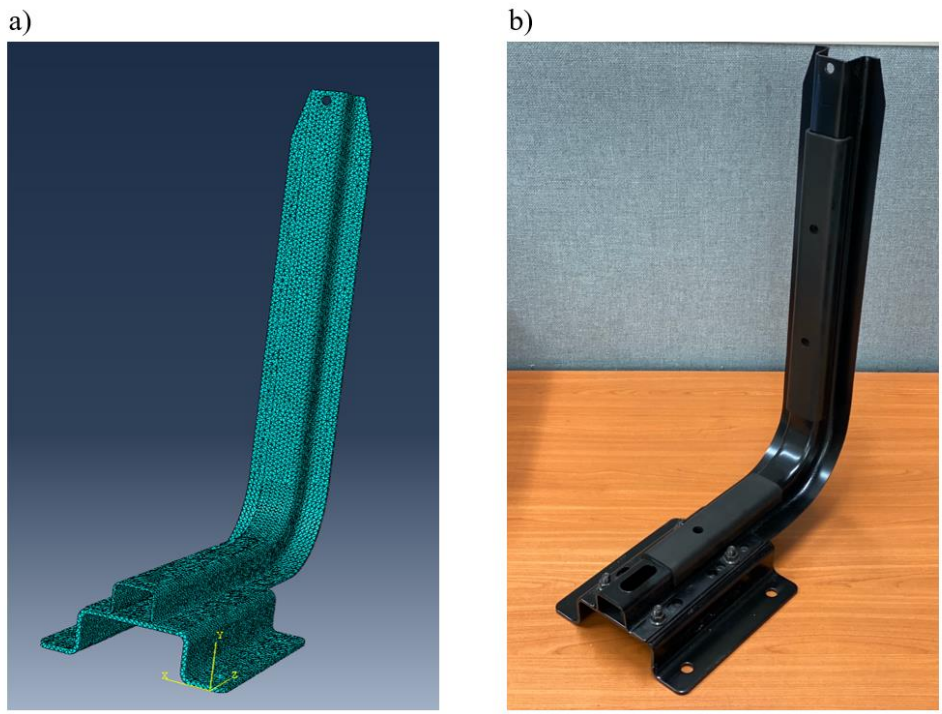

Figure 5.1 (a) A tank bracket model designed in ABAQUS. (b) A tank bracket model designed for experiment.

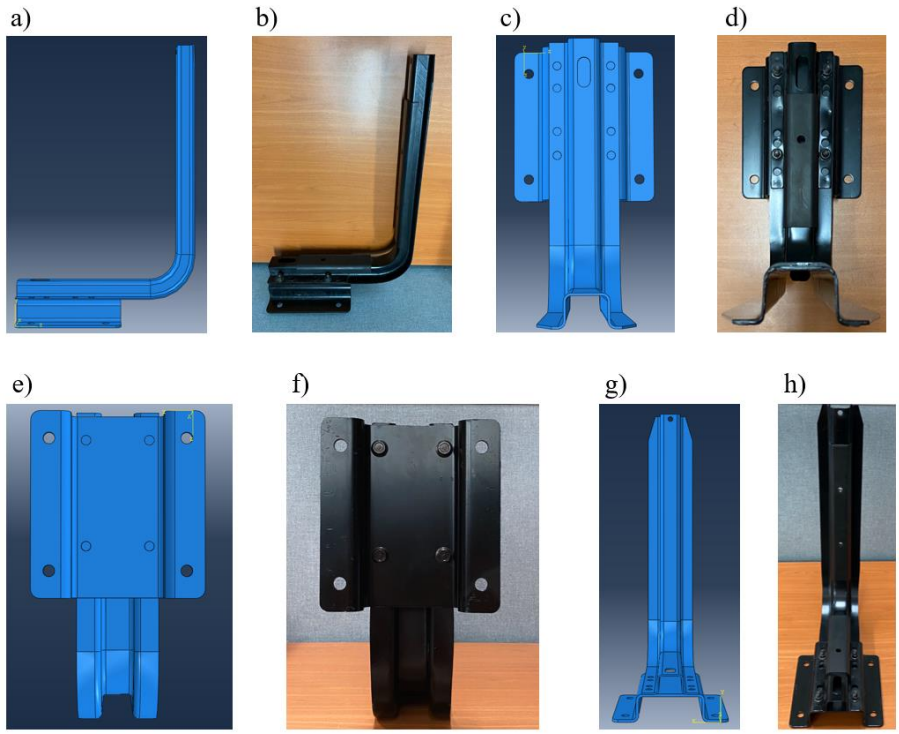

Figure 5.2 A tank bracket model in various view designed in ABAQUS and real experiment.

A tank bracket model is shown in Fig. 5.1 and 5.2. There are two parts in the tank bracket model and assembled by four bolts. The models in Fig. 5.1(a) and (b) are the ABAQUS model and real model, respectively. Various views of the tank bracket model are shown in Fig. 5.2. Due to the complexity of the model, the C3D10 tetrahedral elements were employed for tank bracket model. The C3D10 element is a general-purpose tetrahedral element. The C3D10 element is especially attractive because of the existence of fully automatic tetrahedral meshing process. To match the dynamics of the experimental tank bracket model to the numerical tank bracket model, each part of the assembled model should be identified first. Then the assembled model can be updated by identifying the bolt assembles.

5.2.2 The sensor location selection

Each part of the tank bracket can be divided and named bottom (Fig. 5.3(a)) and top (Fig. 5.3(b)). Each bottom and top parts are separately modeled and nodal points are to be checked so that the avoidable points are determined. The avoidance area of each model is shown in Fig. 5.3(a) and (b), for bottom and top bracket model, respectively. First 5 modes are shown and each mode shows the region not to place a sensor in vibration experiments. As the nodal points are chosen, the sensor locations for both models can be decided. Figure 5.4 shows the size of the models and the chosen sensor locations. The eigenvectors from each sensor locations will be applied to the transformation matrices and the full eigenvector of each model can be restored. Although it is a more complex model than plate model, the transformation matrices from SEREP showed extremely accurate restorations.

Table 5.1 Experimental eigen modes

	bottom part (Hz)	top part (Hz)
mode 1	321.9063	95.0017
mode 2	372.3958	158.2019
mode 3	651.3021	181.1169
mode 4	909.4271	367.8403
mode 5	1159.8697	538.6043

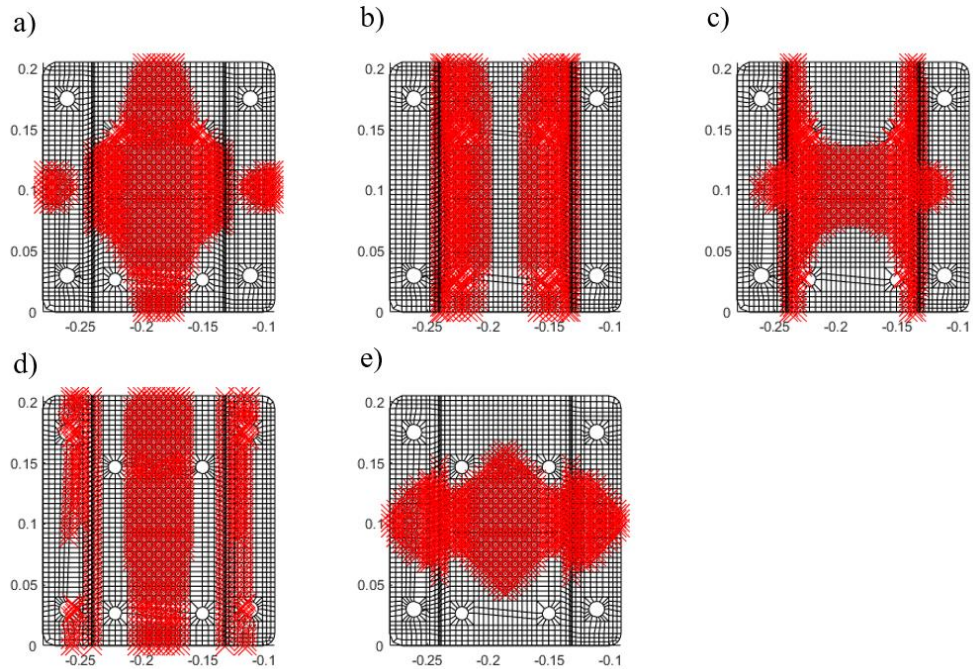

Figure 5.3 Nodal points selected by sensor location selection method in first 5 modes. (bottom model).

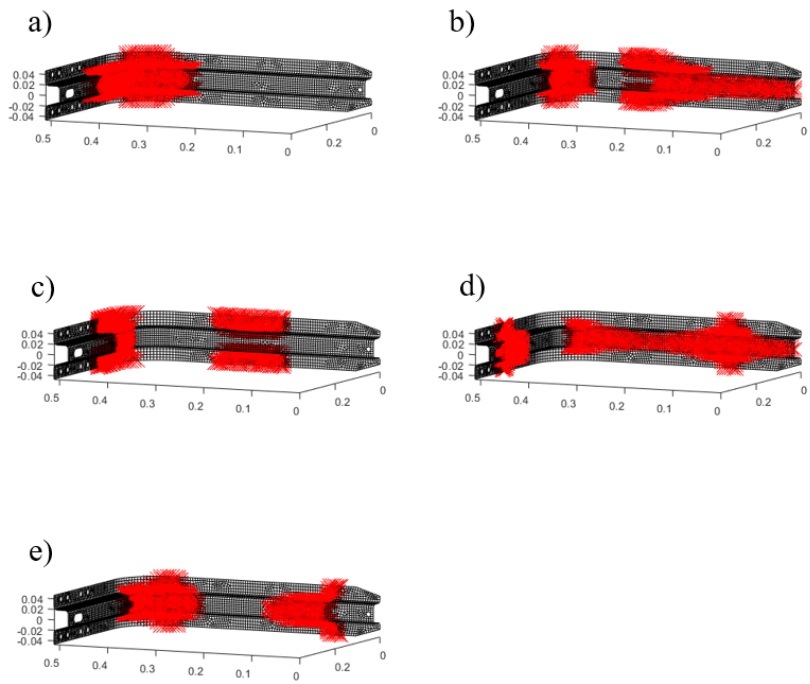

Figure 5.4 Nodal points selected by sensor location selection method in first 5 modes. (top model).

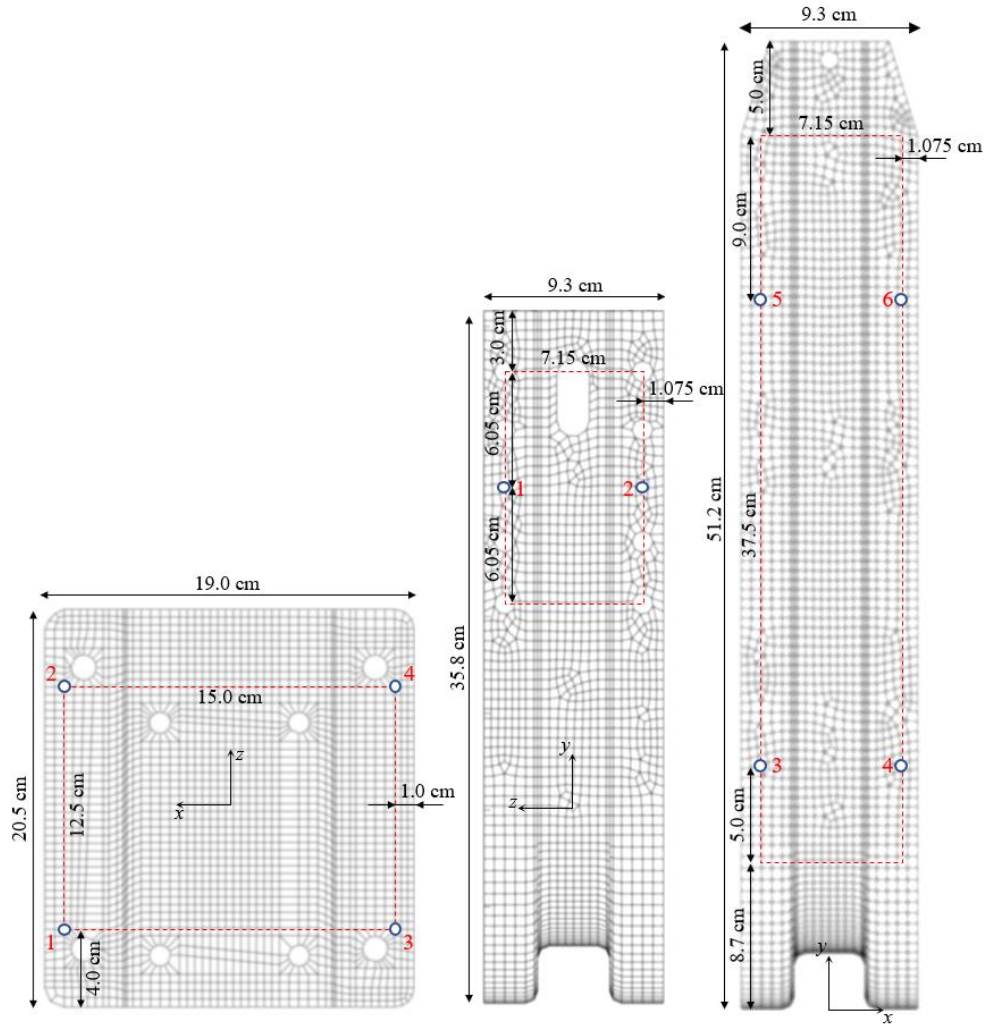

Figure 5.5 Selected sensor locations of top and bottom parts.

5.3 The bolt joint assembly simplification

The bolt joint assembly research field itself has a tremendous research detail and history. The design goals for bolt design is to increase the tension in the bolt and to decrease the clamping force between the joint members. Also, it has to guarantee enough clamping force to prevent bolt self-loosening or fatigue, and to prevent joint slip, separation, or leakage when clamping forces are at a minimum and those hard-to-predict service loads are at a maximum. The considerations of the structural model designers are applied when designing parts and assemblies of the various models. However, in this study, the model used in real commercial trucks was applied, and the dynamic behavior of the actual model was updated through eigenvalue analysis. We wanted to simplify the design of the bolted joint as much as possible and update the properties of the fastened joint.

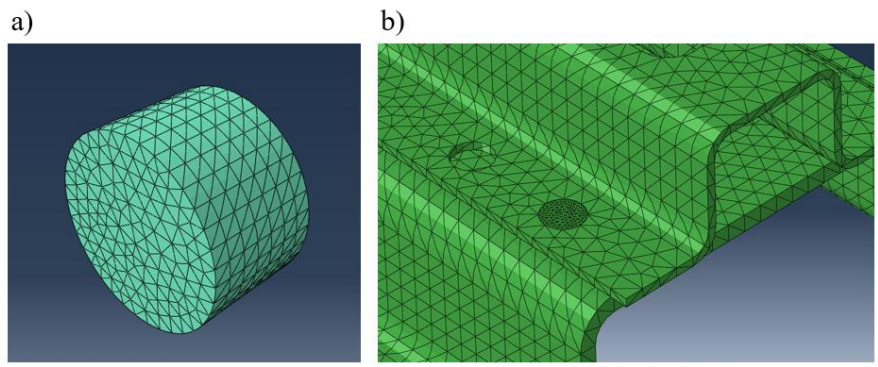

Figure 5.6 Simplified bolt joint in part assembly.

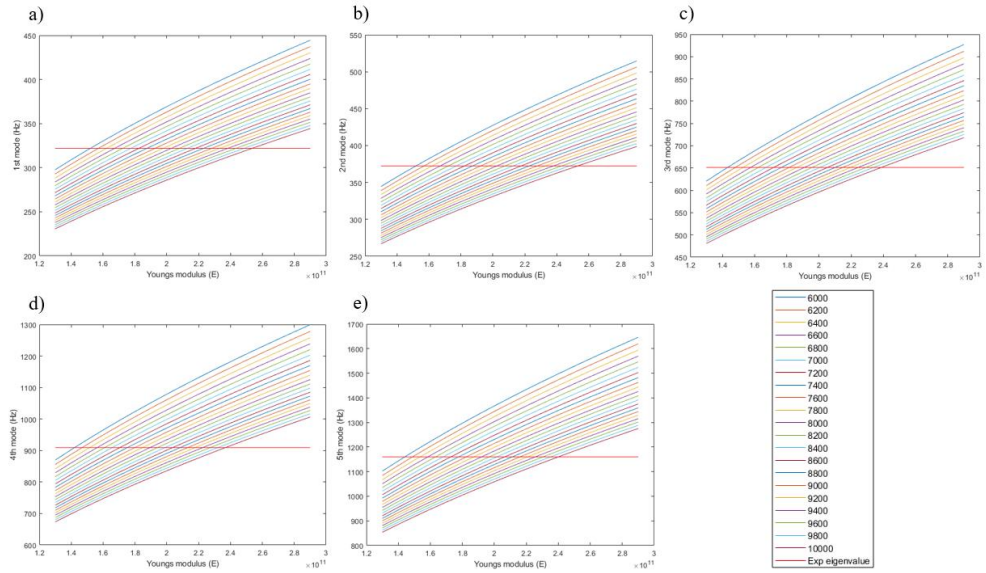

Figure 5.7 The bottom part eigenvalues of the tank bracket model.

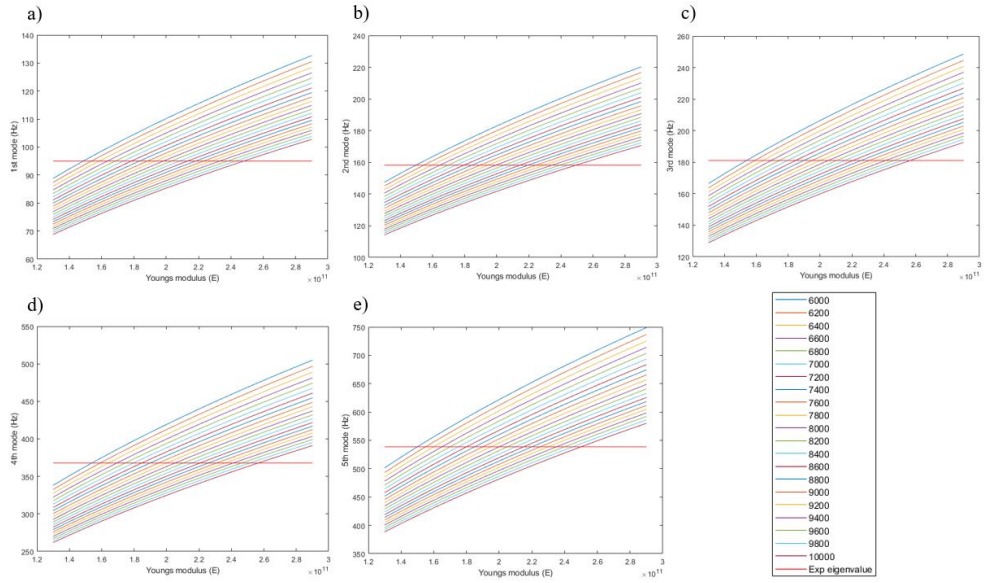

Figure 5.8 The top part eigenvalues of the tank bracket model.

The eigenvalue changes of the top and bottom parts of the tank bracket model with the property changes are plotted in Figures 5.7 and 5.8. About 500 cases were calculated and applied to the neural network functions to find out the parameters that fits the experimental eigenvalues and eigenvectors in first 5 modes. Identified propertied of the bottom and top parts are updated to the numerical model. The updated parts are then applied to the assembly model.

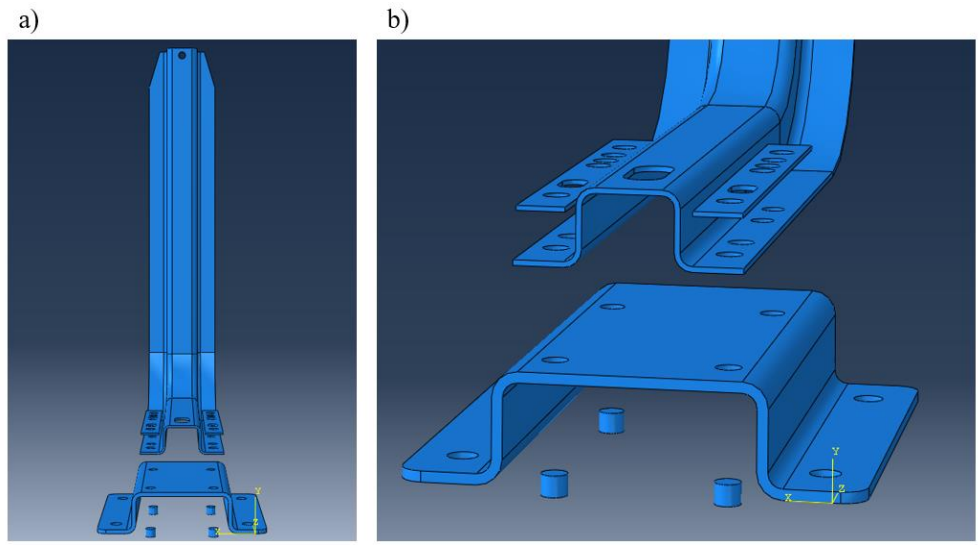

Figure 5.9 The assembly model with simplified bolt.

The simplified cylinder represents the bolt joint in this problem. Top and bottom parts of the model is aligned and the normal and tangent contact properties are given. The cylinder and washers are located in their positions and the tie conditions are given in each hole of the model. Each property of top and bottom parts is identified and applied to the assembly model. The density and Young's modulus have been trained by 500 cases. 7800 kg/m^3 and 190 GPa was selected as the density and Young's modulus, respectively, of the top and bottom parts. The properties of cylinder and washer will be updated in assembly case.

Not only the density and Young's modulus of the cylinders and washers, but also the contact properties will be the parameters for model updating. The bolt joint model is simplified to the cylinder model which reflects the real experimental model. In this study, no consideration was given to bolt loosening or breakage, and it was intended to reflect the dynamic behavior most accurately (modally equivalent model) when perfect fastening was achieved. The material of the model is steel, so the density and Young's modulus are given from 7500 kg/m3 to 8500 kg/m3 and from 190 GPa to 210 GPa, respectively. As the assembly conditions, tangent and normal behaviors were considered. The tangential behaviors (friction coefficient, slip rate, contact pressure) were confirmed to have no significant effect through pre-calculation. The effect of normal contact stiffness was confirmed and considered as an input for training.

In the example of the tank bracket structure in this study, two parts (top and bottom parts) were each constructed to have the modally equivalent model compared to the experimental results. By using the neural network function trained by using the density and Young's modulus of each part as parameters, it was possible to construct a modally equivalent model. Similarly, in the assembly process, a neural network function was constructed using the density and Young's modulus of the bolt assembly structure as parameters, but it was not enough to express the contact conditions. Therefore, in order to build the modally equivalent model of the bolt assembly structure, the function of the neural network using the tangential friction coefficients and normal stiffness coefficients of the bolt assembly were employed as the parameters.

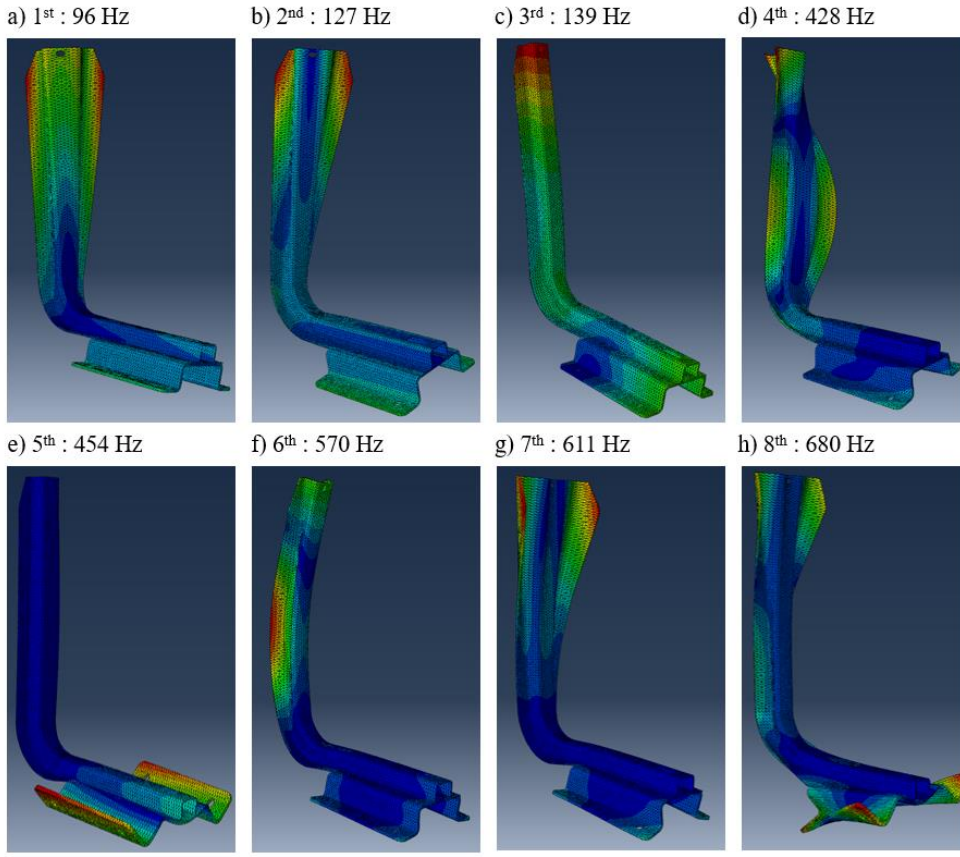

Figure 5.10 The tank bracket eigen modes without updating.

The density and Young's modulus of the cylinders and washers will be the parameters for model updating. The bolt joint model is simplified to the cylinder model which reflects the real experimental model. In this study, no consideration was given to bolt loosening or breakage, and it was intended to reflect the dynamic behavior most accurately when perfect fastening was achieved. The material of the model is steel, so the density and Young's modulus are given from 6000 kg/m^3 to 10000 kg/m^3 and from 190 *GPa* to 220 *GPa*, respectively. As the assembly conditions, tangent and normal behaviors were considered. The tangential behaviors (friction coefficient, slip rate, contact pressure) were confirmed to have no significant effect through pre-calculation. The effect of normal contact stiffness was confirmed and considered as an input for training. The initial value of density

was employed by measuring volume and weight of the experimental model. The initial values of Young's modulus and normal contact stiffness were chosen as the median of each given range.

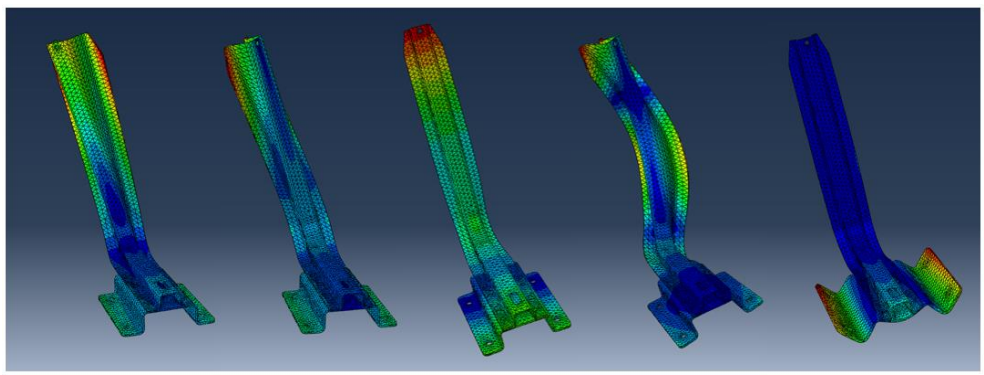

Figure 5.11 The updated tank bracket model.

Table 5.2 Fully-assembled tank bracket eigenvalue comparison.

	Exp (Hz)	Updated (Hz)	Error (%)
mode 1	88.656	89.078	0.476
mode 2	117.65	118.07	0.357
mode 3	128.54	128.97	0.335
mode 4	397.22	394.39	0.713
mode 5	423.78	424.58	0.189

By applying the properties of the bolt joint, washer parts and contact properties as a parameter for the assembly model, the numerical fully-assembled tank bracket model became possible to react same as the experimental model. The density and Young's modulus of top and bottom parts are updated first. Then the contact properties and the bolt joint, washer properties are updated next. The updated tank bracket model shows accurate eigenvalues and eigenvectors compared to the experimental data. As shown in this example with complex model, the digital twin concept consists of three distinct parts: the physical product (the experimental model), the digital/virtual product (the numerical model), and connections between the two products (the identification of the model updating parameters). The

connections between the experimental model and the numerical model is the vibration data that flows from the physical product to the digital/virtual product. The connection information of the problem can be changed in different concept of the examples that is available from the digital/virtual product to the physical environment.

Table 5.3 Updated properties of the tank bracket assembly model.

	Density (kg/m^3)	Young's modulus (GPa)
Top part	8021	211
Bottom part	7617	193
Bolt joints	9012	178
Washers	8783	183
Contact stiffness	1.3909e15 N/m	

Table 5.4 Updated properties compared to the initial properties.

	Bottom (initial)	Bottom (updated)	Top (initial)	Top (updated)
Density (ρ, kg/m^3)	7464.1	7617.0	8194.9	8021.0
Young's modulus (E, GPa)	200	193	200	211

Chapter 6.

Conclusion

In this study, a method was proposed for structural system identification using a sensor location selection method, and this was validated using two different experimental examples. A variety of structural system identification methods have been constructed and applied to system identification problems, but these have limitations. The limitations on structural system identification methods arise from an increase in the number of system parameters and the complexity of a model. In the present study, these limitations were resolved by applying the inverse of a DOF-based reduction method. The DOF-based reduction method was employed to construct a full model of the perturbed plate model. The significance of the structural system identification problem can be highlighted in the experimental problem, because we update the numerical model using data from the experimental model. Practical problems were considered, using the continuum model as a delicate approach to vibrational testing. When selecting a sensor location on the structure, the influence of the error was found to increase dramatically at the nodal

points. A sensor location selection method was proposed, by selecting a high displacement term and avoiding nodal points corresponding to certain interesting mode shapes. The influence of the nodal points was confirmed through a simple bar problem, and the sensor location selection method was applied in the experimental verification. Constructing a system identification method using the IPM and IIRS methods with the sensor location selection method provided a strong system identification method. The methodology proposed here was employed to construct and validate a structural system identification method. This method could be used to minimize computational time and increase convergence.

The model updating method of structural system has been proposed and validated by experimental example in this study. A various methods of structural system identification had been constructed while having situational limitations. Limitations are handled by IIRS and IPM. Degrees of freedom-based reduction method, IIRS, enabled the limitations of the number of the sensors on vibration test. Again, the IPM led us to solve an inverse problem and enabled to solve an accurate parameter that matches with the experiment data. The sensor location selection method was employed to select proper locations for the vibration test to minimize the experiment error. A simple aluminum plate model and a complex tank bracket model were applied for experimental verification. Each model was applied to find thickness and mechanical properties as a parameter to detect a model change. Through these verifications the identification method was determined as an accurate process. According to this study, an identification process was introduced and expect to be able to detect damages in even more areas or to improve the accuracy of the structural analysis models.

In this study, a method was proposed for model updating using DOF-based

reduction method and CNN, and this was validated using two different experimental examples and two different numerical examples. A variety of structural system identification methods have been constructed and applied to model updating problems, but these have limitations in calculation time and variety of the application. The limitations on calculation time arise from iteration time in FE model restoration. In the present study, these limitations were resolved by applying the SEREP and CNN. The SEREP, one kind of DOF-based reduction method was employed to construct a full model of the perturbed plate model. The significance of the SEREP is highlighted in the restoration process, because it does not have any iterations while maintaining the accuracy. The problem of SEREP which needed more numbers of eigenvectors were overcome by CNN. Since SEREP required eigenvector as many as the number of sensors, eight mode shapes were needed to construct transformation matrices by SEREP. By training the 2D-CNN function, it was able to decrease the calculation time significantly. The accuracy of SEREP was validated by 1D bar problem. The 2D-CNN function was validated through the experimental examples from previous study and showed significant calculation efficiency while maintaining the identification accuracy. Constructing a model updating method using the SEREP and 2D-CNN provided a strong updating method. The methodology proposed here was employed to construct and validate a structural system identification method. This method could be used to minimize computational time and increase the identification convergence.

Proposed updating methodologies were applied to complex models. The vibration responses of the experimental models were employed to the numerical model and updated its properties to improve the accuracy of the numerical models.

A complex FE models were applied to updating process, such as bottom and top parts of the tank bracket model of the commercial trucks. Each updated parameter of the part improved its accuracy and applied to assembly model. The assemble modeling including the contact properties and bolt joints were simplified by proposed updating methods.

Appendix A.

Structural design of soft robotics using a joint structure of photo responsive polymers

A.1 Overview

Photoresponsive polymers (PRPs) have a non-contact bending behavior based on their position when they are irradiated by a specific wavelength of light. In this paper, the behavior of self-deforming PRPs is discussed through multiscale simulations and structural designs. In repeated bending, it is difficult to return to the initial state through different paths because the PRP moves periodically in the same path. We designed an anti-obstructing motion of a PRP operator based on a nonlinear co-rotational finite element model, which could not be designed for the

existing bending behavior. The PRP operator can move independently in specified directions by attaching an opaque part to the PRP operator as a joint structure. The device can be divided into two separate regions. One region can be bent to move the desired object, and then the PRP operator can move away, avoiding the object by bending in the other region. The PRP operators can take actions whether to move an object or to avoid an obstacle and adjust the friction force of robot feet based on bio-inspiration. In our experiments, the production process of PRPs is presented, and operations implemented in soft robot applications of gear rotation and walking.

A.2 Structural design of soft robotics

Photoresponsive polymers (PRPs), self-deformable polymers operated by light irradiation, are an excellent material for use in soft robotics. Unlike any other self-deformable material, PRPs have significant advantages in that they can be reversibly operated without any cable or wire connections. Since the driving force for actuation is induced by external light, the system does not require any external power supply, such as a battery or a supercapacitor. Due to these advantages, PRPs have been investigated by many research groups to assess their usefulness in soft robotics **[76-87]**.

The functionality of a PRP is based on its liquid crystalline polymer network. Each monomer chain consists of a flexible side chain and a rigid mesogen core, where the chains are crosslinked. Similar to conventional mesogen molecules that form a liquid crystal phase, these crosslinked chains can form a variety of liquid

crystal phases by aggregating or self-aligning. However, they differ in the intermolecular interaction characteristics between the molecules and in the structural interference of the side chains inside the molecule that simultaneously affect the thermo-mechanical behavior of the compound. The mechanical properties of the material depend on the type of mesogenic moieties present, the length of the side chains, and the crosslinking ratio of the network.

In a PRP, part of the mesogen is substituted with a photosensitive monomer. Hence, a reversible conformation change occurs when irradiated with a specific wavelength of light, and the state is restored to its original state when exposed to another wavelength of light. During the change of conformation of a photosensitive monomer, the local orientational order of the liquid crystalline matrix is affected, which acts as a trigger to turn the liquid crystalline phase into an isotropic phase (or vice versa). The light intensity exponentially decays as light penetrates the PRP, the photoinduced reaction is distributed throughout the thickness of the PRPs, and the corresponding actuation behavior is observed experimentally in the form of bending.

Azobenzene-incorporated liquid crystal polymers (azo-LCPs) can respond via photoirradiation using a liquid crystal monomer and azobenzene crosslinker. Many studies of azo-LCPs have been done **[76-81]**. A soft robot can be designed based on the unique characteristics of materials and operating mechanisms. The direct bending of the PRP introduced a fundamental movement of a PRP by light **[82]**. With continued research and development on PRPs, various applications were shown: a plastic motor, a three-dimensional (3D) movement, and a photoswitchable device **[83-85]**. Since PRPs do not require any cable connections or contacts while operating, examples of control in a tight space were demonstrated

[86-87]. To operate PRP-based soft robotics and to design its accurate movement, multiscale mechanics for PRPs and experimental environments were developed as follows: the photobending feature of the in silico PRPs was produced, and its mechanical behavior described **[88-89]**. The photostrain of the azo-LCPs for the PRPs was predicted with various light irradiation conditions and molar ratios of azobenzene moieties **[90]**. Molecular dynamics simulations were carried out to investigate the multi-physical actuation behavior of the neat specimen of the PRPs **[91-93]**. The trans-to-cis isomerization reaction of the azo-LCPs in the PRPs was represented by applying the photoreactive potential energy to the torsional potential for diazene groups in the unit cell. As a continuum part of the multiscale simulation, the nonlinear finite element method (FEM) was employed to solve the light-induced bending curvature in terms of the penetration depth and light intensity **[94-97]**. The photomechanical properties of the interphases in the light-responsive polymer nanocomposites were identified by multiscale and multi-physical analysis **[98-99]**. The photothermal actuation performance of the PRPs was satisfactorily explained by the multiscale simulation **[100-103]**. Most of these studies developed applications for simple bending or stretching of the PRPs.

The objective of the present study is to develop prototypes of photoreactive mechanical elements to assess the feasibility of the photomobility of the PRPs as a practical mechanical device. The behavior of the PRPs was evaluated through multiscale simulations and structural designs. In a repeated bending behavior test, it is difficult to return to the initial state through different paths because the PRP tends to move in the same path. By attaching an opaque joint structure part into the PRPs, an anti-obstructing motion based on the nonlinear co-rotational finite element model was designed. Through the bending behavior of the separated parts

of the PRP, it was able to move independently in the desired direction. The soft robots introduced in this paper can take actions whether to move an object or to avoid an obstacle. These movement studies were applied to a rotating gear and a quadruped walking robot. Multiscale mechanics was incorporated to manage various actions of the soft robotics. In the experiments, the production process for the PRPs was presented then implemented showing, for example, that the friction force of a robot's feet can be adjusted based on bio-inspiration. The findings show a robust design for the creation of photo-mobile soft robots. This paper is organized into five sections. Section A.3 describes the experimental setup for the PRPs, and section A.4 includes the multiscale mechanics and nonlinear FEM for structural design. The results are discussed in section A.5. The manuscript is wrapped up with a summary and conclusion in section A.6.

A.3 Experimental setup

A.3.1 Synthesis process

We synthesized the azobenzene cross-linkers by ourselves through the following process with prepared chemical compounds (KI, MgSO4, trimethylamine, acryloyl chloride, K2CO3, 6-bromohexan-1-ol, and hydroquinone: from Sigma-Aldrich, 4,4’-(diazene-1,2-diyl)diphenol: from Tokyo Chemical Industry Company, organic solvents such as tetrahydrofuran (THF), N,N-dimethylformamide (DMF), chloroform, methanol, ethyl acetate, and deionized (DI) water: from Daejung Chemical Company). The chemical compounds and the organic solvents we prepared were dissolve in organic solvent, recrystallization, quenched in DI water, extraction, filtering, several times of column chromatography purifying, and final

recrystallization in methanol to obtain DA-hex-AB (yield: 80%). Details regarding the production process of the azo-LCPs can be found in the reference **[100]**.

A.3.2 Sample preparation

The liquid crystal (LC) monomer (RM82), azobenzene crosslinker (2azo), photoinitiator (ChivaCure 534, Chitec), and hydroquinone were used to construct a polymer network. The thickness of the PRPs can be adjusted by placing the spacers (Fluka, Sigma-Aldrich) between the glass molds coated by the alvamide solution (methanol 98% and Elvamide® 2%). The spacers employed here are sphere-shaped, having diameters of 30 μm and 40 μm, which finally produce the specimens of 30 μm and 40 μm thicknesses, respectively. The spacers can be placed in the edge of the glass mold to produce a uniform thickness specimen.

The azobenzene crosslinker(2azo) and RM82 were melted in a glass vile at a different molar ratio with 3 *wt%* photoinitiator (Chivacure 534, Chitec) and trace amount of hydroquinone inhibitor at 100 °C until fully melt. The well-mixed compound mixtures were injected into the glass mold by capillary force. Monomers were aligned to the direction of the coated surface of the glass mold. Mixtures have a relaxation time in the dark for 30 *min* then polymerized by a 530 *nm* light at an intensity of 80 $mW \cdot cm^{-2}$ for 2 *h*. Film-type samples can be obtained by peeling off the glass mold on the sample surface with stabilization time for one day.

A.3.3 Spectrometer characterization

A Fourier-transform infrared spectrometer (iS5-ATR-iD5, Thermo Fisher Scientific) was employed to test the degree of polymerization and the alignment of the samples. The optical and thermal properties of the azo-LCP are listed in Table 1. The effect of the azobenzene concentration on the LC monomer (MD-RM82, Synthon Chemicals) was tested by regulating the relative 2azo content. Three concentrations (10 %, 20 % and 30%) were chosen: MD-RM82-10, MD-RM82-20 and MD-RM82-30. The alignment factor (S) is calculated, $S = (R - 1)/(R + 2)$. Here, R is the dichroic absorbance ratio of each film at 1600 cm^{-1} [79-80]. The azo-LCPs have a various phase such as crystal phase, nematic phase and isotropic phase depending on the temperature in Fig. A.1. The Specimens of three different concentrations were used and measured using a microscope. The table 1 shows the basic information of our samples. The glass transition temperature (T_g) and storage modulus E' were tested in a dynamic mechanical analyzer (DMA, Q800, TA instrument). Single-frequency iso-strain mode and 1 Hz frequency sweep test mode with the temperature ramping from 25 ℃ to 150 ℃ (3 ℃·min^{-1}) were used.

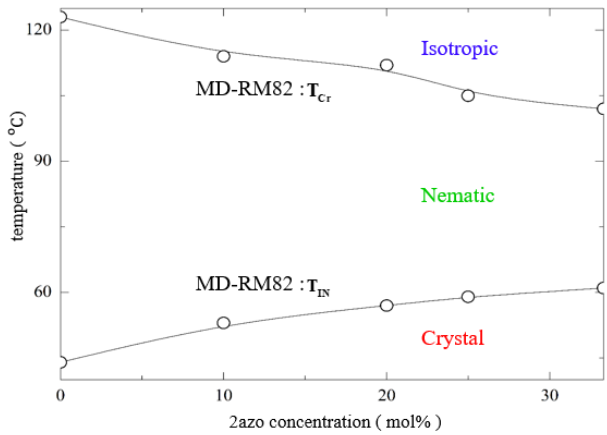

Figure A.1 Phase changes of the azo-LCPs (RM82).

Table A.1 Optical and thermal properties of the azo-liquid crystal polymer (LCP).

Azo-LCPs	R	S	T_g	v_e (%)
MD-RM82-10	3.7462	0.478	78	72
MD-RM82-20	3.5342	0.458	74	62
MD-RM82-30	3.8142	0.484	70	58

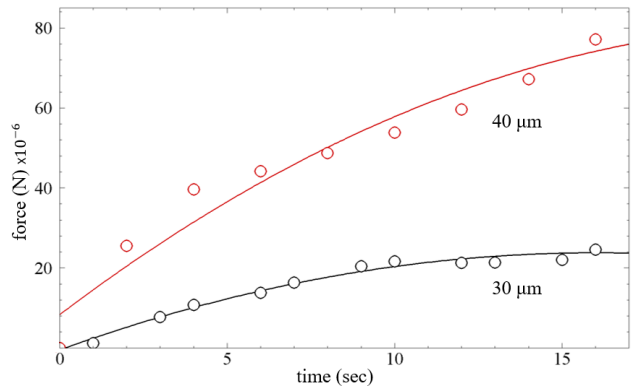

Figure A.2 The bending force as a function of time for two specimens of 30 µm and 40 µm thicknesses.

The cross-linking ratio ν_e is calculated by $\nu_e = E'/3RT_r$, where E' is the storage modulus, R is the gas constant, and T_r is a rubbery transition temperature ($T_r = T_g + 20\ ^oC$) of the samples.

The force transmitted by PRPs and the reaction speed are most important factors in photo responsive soft robotics. Figure A.2 shows the exerted bending force as a function of time under the UV-irradiation. In the experiment, the LC monomer (RM82) specimens of 30 μm and 40 μm thicknesses were employed. The precise scale (AS X2 series) was used to measure the bending force. As shown in Fig. A.2, the specimen of 40 μm thickness can exert a bigger force than that of 30 μm thickness. However, the reaction speed of the specimen of 30 μm thickness is faster than that of 40 μm thickness.

A.4 Structural modeling

A.4.1 Multiscale modeling

Before introducing structural modeling, it is worth outlining the underlying mechanism of the deformation of the PRPs. The liquid crystalline polymer network consists of chain-like molecules with flexible side chains and a rigid mesogen core. Trans-to-cis isomerization occurs when irradiated, and the trans-state is restored when exposed to visible light. The multiphysical analysis efficiently represents the microscopic change of the PRPs by implementing the light-induced variation of the step length tensor into the neo-classical free energy formalism. As the actinic light traveling through the material inevitably loses its energy, the gradient of the accompanied eigenstrain is obtained through the thickness direction. The

eigenstrain is the photostrain of the flat-plate structure that induces the bending deformation. The amount of light-induced strain that is determined by the isomerization of the photochromic chromophore is, therefore, the governing factor of the length change. The population of the cis azobenzene should be calculated as functions of time and the penetrating thickness; then, the light-intensity profile in the thickness direction is expressed by a form of the Lambert-W function that depicts the bending mechanism with the unbalanced cis population. Parametric research regarding the photo-bleaching effect can be found in the referenced paper [104]. In order to describe this, a nonlinear FEM was utilized to predict and design the unusual photodeformation path of the devised joint structures.

A co-rotational nonlinear FE model was designed to predict the end-point path of the PRPs. In this study, we concentrated on the control of the movements and to find the path of the end-point for various scenarios. For the end-point path design, we came up with a joint structure. If there is an area that does not absorb light, it would be possible to make different movements by divided regions. This joint structure was designed by attaching an opaque part. The device can be divided into two separate regions. One region can be bent to move the desired object, and then the PRP operator can move away, avoiding the object by bending the other region. This movement with the joint structure allows contact with the desired object or to avoid an obstacle, as needed. The co-rotational nonlinear FE modeling enables us to design the pathway. Since the photobending behavior of the PRP is rotation-dominated, the deformation of the microstructure remains small, whereas the global shape of the structure is severely distorted. The element-independent co-rotational formalism was employed to represent this geometric nonlinearity of the structure upon irradiation, assuming that the material undergoes a local linear

deformation. As a result, some essential photomechanical physics (*e.g.* the deconvolution of various stimuli and deformation due to snap-through instability) could be comprehended from a mechanical point of view. The present FE model enables us to design and analyze the PRPs with arbitrary shapes and boundary conditions, considering the geometric nonlinearity as well as the microstate evolution in the off-axis direction.

A.4.2 Nonlinear FEM with a co-rotational formulation

The physical phenomenon of the PRPs is theoretically expressed by tensorial notation. The free-energy description is composed of a deformation gradient and a shape tensor designating the nematic ordering. The constitutive laws including the photothermomechanical effects are derived from a free-energy formulation whereby a variational calculus approach is incorporated **[104]**. The resulting constitutive laws are easily applicable regarding the FEM equation of the linear shell element,

$$\begin{aligned}\delta W &= \int_{\Omega} \delta\left(\boldsymbol{\varepsilon}^{0} - z\hat{\mathbf{k}}\right)\left(\boldsymbol{\sigma}^{0} - \boldsymbol{\sigma}^{ph}\right) dV \\ &= \delta\overline{\mathbf{d}}_{d} \cdot \overline{\mathbf{K}}^{e} \cdot \overline{\mathbf{d}}_{d} - \delta\overline{\mathbf{d}} \cdot \overline{\boldsymbol{\Sigma}}^{ph}.\end{aligned} \tag{A.1}$$

Where $\overline{\mathbf{K}}^{e}$ is the internal stiffness matrix and $\overline{\boldsymbol{\Sigma}}^{ph}$ consists of the photo-triggered stress and moment resultants. From a mechanical-design viewpoint, the deformations resulting from the applied external stimuli should be effectively computed. The external stimulation can be equivalently counted as a mechanical force. Since the light-induced change of the nematic director can cause significant rotation, the nonlinear FEM should be adopted to treat the geometric nonlinearity.

Most of the deformations accompanied by an unbalanced photoisomerization are from bending behaviors, so a large portion of the displacement is expressed as rigid-body rotation. The geometric nonlinearity consideration plays a vital role in a deformation analysis. The nonlinear FEM, based on a co-rotational formulation, was implemented in the present study **[105]**.

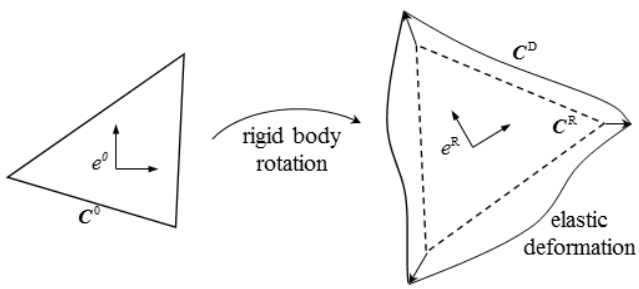

Figure A.3 Configurations of the co-rotational formulation.

In Fig. A.3, C^0, C^R, and C^D represent the configuration of the initial, co-rotated, and deformed states, respectively. The displacement is treated as a two-sequence process; one is the rigid-body motion from the initial state to the co-rotated configuration, and the other is the elastic deformation itself. The total of the displacements and the rotations at the structure nodes are expressed by δu_i and $\delta\omega_i$, both of which are expressed as a 3×1 vector. That is, $\delta\omega_i$ is the pseudovector of the rotation tensor R_i, and the subscript i represents the nodal number of each element. The expression changes if the displacements and the rotations should undergo a series of manipulations through the multiplication of the specific matrices. This includes the frame rotation, the movement from an undeformed to a co-rotated formulation, and the axial-rotation angle extraction

from the rotation matrix. The localized displacements and rotations are considered the elastic deformation of each element. The conversion procedure is expressed by

$$\begin{bmatrix} \delta\overline{\mathbf{u}}_{di} \\ \delta\overline{\boldsymbol{\theta}}_{di} \end{bmatrix} = \mathbf{H}\begin{bmatrix} \delta\overline{\mathbf{u}}_{di} \\ \delta\overline{\boldsymbol{\omega}}_{di} \end{bmatrix} = \mathbf{HP}\begin{bmatrix} \delta\overline{\mathbf{u}}_{i} \\ \delta\overline{\boldsymbol{\omega}}_{i} \end{bmatrix} = \mathbf{HPT}\begin{bmatrix} \delta\mathbf{u}_{i} \\ \delta\boldsymbol{\omega}_{i} \end{bmatrix}, \tag{A.2}$$

where δu_i and $\delta\omega_i$ represent the total nodal displacements and the total rotations from the global frame, respectively. $\delta\overline{u}_{di}$ and $\delta\overline{\omega}_{di}$ are obtained through the multiplication of the rotational matrix **T**, for which the original coordinate is related to the co-rotated coordinate. **T** is determined from the geometric value of the angle difference between the global and co-rotated frames. **P** is the projector matrix for which a location change is applied in the rigid-body motion, and are measured from the co-rotated elemental frame that can be considered as the elastic deformation. **P** is determined by the location of each element, whereby the translational movement is obtained using the centroid-location difference. The **H** matrix relates a rotating pseudovector to the axial rotating angles to produce the degree of freedom (DOF) between the plate and the shell element in the elastic deformation. The projectors **P** and **H** are obtained through the calculation of a Jacobian from each of the related displacements depending on the geometrical properties **[105]**.

The internal and external force vectors are obtained via the above procedure,

$$\begin{aligned} \mathbf{f}_{\text{int}}^{(\text{g})} &= \mathbf{T}^{\text{T}}\mathbf{P}^{\text{T}}\mathbf{H}^{\text{T}}\overline{\mathbf{f}}_{\text{int}}^{(\text{e})} = \mathbf{T}^{\text{T}}\mathbf{P}^{\text{T}}\mathbf{H}^{\text{T}}\mathbf{K}_{\text{elem}}\mathbf{v}_{d}^{(\text{e})} \\ \mathbf{f}_{\text{ext}}^{(\text{g})} &= \mathbf{T}^{\text{T}}\mathbf{H}^{\text{T}}\overline{\mathbf{f}}_{\text{ext}}^{(\text{e})}. \end{aligned} \tag{A.3}$$

The difference between the calculations of the internal and external forces is a consideration of the projector properties. The external force vector is a follower force exerted on the deformed configuration of an element. The translational rigid body motion is not considered. In the present study, the externally applied force results in an in-plane force and the moment from the light-induced strain. The driving force of the eigenstrain on the PRPs is affected by external stimuli such as light and thermal changes. In the co-rotational formulation, the frame-change process is well treated by the rotation and projection matrices. A strong point is produced here when a comparison to other nonlinear FEM theories is made. Regarding the total and updated Lagrangian method that expresses the total displacements using the deformation gradient, it is difficult to factor out the properties of the rigid-body projection, while difficulties are encountered in the application of the higher-order plate and shell elements.

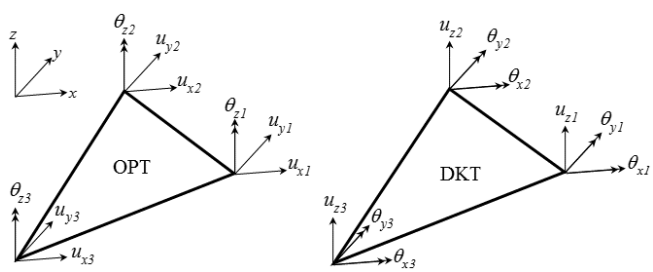

Figure A.4 High-order plate and shell elements.

A classically established FE model can be easily implemented, and high-order plate and shell elements can be used because the element itself undergoes only an elastic deformation, which produces more choices in terms of the element selection. The usage of a higher-order element guarantees the convergence and accuracy of the solution in a small number of meshes. The number of elements is directly

related to the number of design variables in an optimization simulation, so a higher-order element provides flexibility regarding the selection of the number of design variables as well as an effective solution. The plate and shell elements are selected and assembled in 18 DOF elements **[106]**. The plate element is the optimal triangular element (OPT) from Fellipa **[105]**, and the shell element is the Discrete Kirchhoff triangular element (DKT) **[107]** as in Fig. A.4. The assembled triangular element consists of 18 DOF elements (6 DOFs for each node). It is worth noting that the two half-thickness cantilevers with the two attached cantilevers are modeled with pre-assembled triangular elements of different diagonal directions. The two pairs of triangular elements are then merged into a total of four triangles for the formation of one rectangular element. In this case, the bending rigidity of the element should be recalculated because of its thickness dependency, and the element connectivity information for the virtual overlaid rectangular should be formed while the consistency of the ordering rule for the numbering of the local nodes is maintained. The local coordinates that can eliminate the warping error that is inherent in the element itself are explicitly obtained from the triangular element. The formation of a rectangular element in the pattern-design point-of-view is advantageous. Also, the direction dependency of the resultant moment in the triangular element does not exist in the rectangular element, resulting in a guaranteed mesh dependency.

For the attainment of a nonlinear FEM solution, the Newton-Raphson method is used. The tangent-stiffness matrix is obtained from the differential of the residual force. Compared with the initial flat specimen, the force-increment tendency of the last bent specimen is divergent. The tangent-stiffness matrix in the bent shape undergoes a significant rotation that induces the complexity in terms of the

calculation of the sub-matrices. However, a small initial-force increment incurs a high computational cost. An optimal situation consists of a significant increment for the early phase and a small increment for the latter phase. The adaptive Newton-Raphson algorithm is therefore applied through a determination of the divergence point. The force-increment size is divided in half; the convergence is guaranteed while the computation time is adequately reserved. The presented multi-physical analysis efficiently represents the microscopic conformational change of the PRPs by implementing the light-induced variation of the step length tensor into the neo-classical free energy formalism. Also, the decaying light intensity profile and the associated local photomechanical properties along the penetration depth are efficiently computed using nonlinear Beer's law, which reflects the photobleaching effect **[108]**. Accordingly, the nonlinear FE simulation is utilized to predict and design the unusual photodeformation path of the devised joint structures of the PRPs. This procedure is crucial to realize and optimize the user-defined complex 3D deformations, such as bypassing the obstacles, actuating the mechanical component, and walking.

A.5 Result and discussion

It is challenging to implement a motion that proceeds in one direction continuously when the motion in the forward direction coincides with the backward motion. A simple bending is made repetitively on the same path only. It is necessary to separate the irradiation region to operate the PRPs effectively. We attempt to solve this problem by introducing a joint structure into the PRPs. As shown in Fig.

A.5(a), an opaque part (p2) as a joint structure is placed in the center of the PRPs so that the PRP parts (p1 and p3) are separated by p2. Due to the opaque part, the PRPs can operate independently. From now on, the schematic of the PRPs in Fig. A.5(a) is called a PRP operator. As the UV light irradiates the PRP operator, a bending motion occurs from the center point of the light irradiation. Without any boundaries, however, it is almost impossible to adjust the range of irradiation. Various motions are expected by adding the joint structure. The movement of the PRP operator depends on the path to the endpoint over which an object moves or avoids an obstacle. The size of the operator can be determined by design necessity. The width of the opaque part should be wide enough to separate the UV light. It is highly desirable to adopt the PRP operator into soft robotics through the following improvement process.

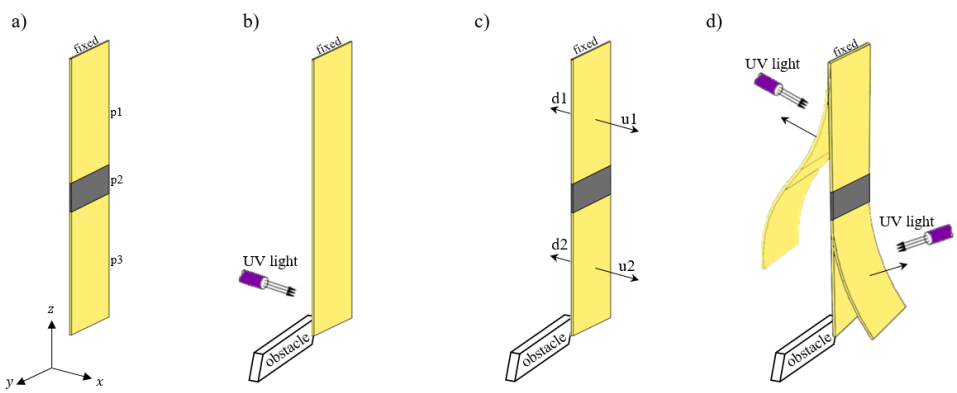

Figure A.5 (a) Schematic of the PRP operator (p1 and p3) with a joint structure (p2). (b) Cantilevered simple bending of the PRP operator with an obstacle. (c) Given options of the bending directions. (d) A detailed procedure of the anti-obstructing motion.

A basic movement of cantilevered simple bending is displayed in Fig. A.5(b), where the PRP operator bends toward the UV light. As seen, the endpoint of the

cantilevered simple bending cannot avoid an obstacle if located on the path. As mentioned earlier, when the PRP operator with a joint structure is employed, it may be possible to avoid the obstacle. A schematic of the cantilevered PRP operator with the obstacle is shown in Fig. A.5(c). The main target is to avoid the obstacle without contacting the obstacle. The endpoint of the operator is bent to the upper side (u1, u2) to the *x*-axis direction or the lower side (d1, d2) to the negative direction of the *x*-axis by the UV light (Fig. A.5(c)), and all operations are available to return to the initial state by exposure to green light. To avoid the obstacle in Fig. A.5, it is necessary to shrink the PRP operator as possible to the longitudinal *z*-axis direction. The green light initializes the deformation of the structure with the alignment of molecules. Each of the four parts can be bent by UV light and initialized by green light. All possible paths are listed in Table A.2, where case 1 and case 2 are made by irradiating u1 and u2 in the upper direction. This motion shrinks the *x*-direction length to avoid the obstacle. For case 1, after irradiating u1, the next step is no longer meaningful to avoid the obstacle. For cases 3 and 4, the operator is stuck in the obstacle, and no further movement is possible. Case 2, however, is the only way to avoid the obstacle and reach the other side without any contact. After irradiating u2, d1 can be irradiated to pull the endpoint further from the obstacle in the *x*-direction and move around the obstacle down to the *z*-direction. The u2 bending, irradiated by UV light, can be initialized by the green light. A proper method is achieved by moving around the obstacle after these trials. A detailed procedure for case 2 is illustrated in Fig. A.5(d).

Table A.2 Case studies of the anti-obstructing motion.

case 1	u1 on	u2 on	u1 off	fail	no path available
case 2	u2 on	d1 on	u2 off	success	-
case 3	d1 on	-	-	fail	obstacle contact
case 4	d2 on	-	-	fail	obstacle contact

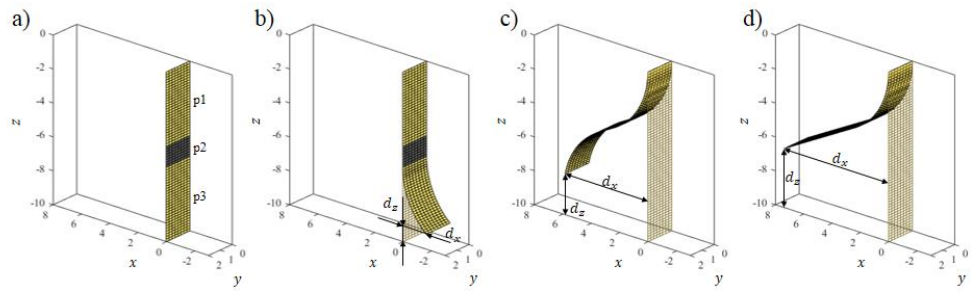

Figure A.6 Finite element (FE) simulation of the path of the photoresponsive polymer (PRP) operator.

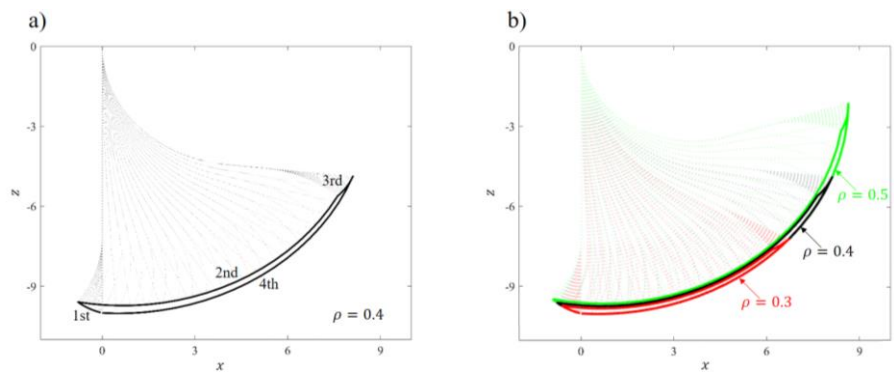

Figure A.7 (a) Prediction of the endpoint reciprocating path from the initial state through different paths. The area of the endpoints determines the size of the avoidable obstacle. (b) The path of the endpoint and the size of the area changes by the UV light intensity.

As shown in Fig. A.6, the path of the endpoint can be predicted by FE simulation, where the nonlinear co-rotational FEM is employed. It would be difficult to predict how much bending is made by the UV light. No bending is made in the gray-shaded opaque part. Here, d_x and d_z denote the x- and z-direction distances between the initial endpoint and the present endpoint, respectively. These values are useful in designing an anti-obstructing motion. This design concept can apply to a gear tooth, regularly arranged on the gear. Once the gear tooth is pushed by the operator, the next tooth appears at the same position. To rotate the gear continuously in one direction, the operator has to return to the original state without disturbing the gear. The path of the endpoint is the primary consideration for repetitive, continuous gear rotation. Two actions are required to rotate the gear: pushing the teeth of the gear and returning to the initial state without any contact to push the next tooth. The teeth of the gear can be pushed by the PRP operator only if the height of the teeth is within the range of d_z in Fig. A.6(b). After pushing the gear, the operator has to return without touching the next gear that appears in the same position. To avoid the next tooth of the gear, d_z in Fig. A.6(c) must be larger than d_z in Fig. A.6(b). When the operator avoids the gear teeth, p3 must be initialized first, then p1 is initialized to be in a position to push the next gear teeth.

Figure A.7(a) shows the predicted path of the endpoint for the anti-obstructing motion. The top end is cantilevered, and the trajectory of the endpoint for the reciprocating path is shown. The movement of the endpoint is divided into four motions in Fig. A.7(a). The first motion is to push the gear teeth in the direction of the gear rotation by irradiating p3 (Fig. A.6(a)), which avoids the obstacle by making a space for the endpoint. The more the operator is bent, the more it can push the object or secure more space and avoid the larger obstacle. It is an

initialization process through the second to the fourth motions. The second motion is most important due to its special motion, which is not realistic in the basic bending movement. By constructing an *S* shape in the second motion (Fig. (A.6c)), the endpoint can move around the space made by the first motion. After the initialization of p3 in the third motion, the endpoint returns to the initial point by the initialization of p1 in the fourth motion so that it can push the next gear tooth. The disadvantage of this process is the time-consuming initialization process. The time-consuming problem may be resolved by installing more than one operator so that the other operator can operate simultaneously during initialization.

The PRP operator can push and avoid the corresponding object and obstacle as needed. As the motion is fixed, the next task is to predict how much it moves. The bending can be designed by the size of an object to push or the size of an obstacle to avoid. The bending amount can be adjusted by the UV light intensity and the size and thickness of the PRP operator. The thicknesses of 30 μm and 40 μm were determined in Section A.3.1 by considering the light intensity and the size of the PRP operator. Figure A.7(b) shows the prediction of the endpoint path by adjusting the light intensity. The path of the endpoint can be changed by light intensity. The paths of the endpoint are displayed in Fig. A.7(b) for ρ = 0.3, 0.4, and 0.5. The inner area of the trajectories in Fig. A.7(b) shows the area that the operator can avoid. As the avoiding area of the endpoint increases, the object moves further to avoid the larger obstacle.

As the light intensity increases, the range of motion 1 increases. The size of the operator in Fig. A.7 is 10 *mm* × 2 *mm*. The first consideration is how much the operator can push the object in motion 1. As the light intensity increases, the range of the endpoint also increases. The *z*-direction deformation changes are 0.63 *mm*,

0.80 *mm*, and 0.94 *mm* as the UV light intensity changes through 0.3, 0.4, and 0.5. We next examine the *x*-direction avoidance range for comparison. To avoid and move around the obstacle, the *x*-direction shrinking degree determines the possible avoidance range. The *x*-direction shrinking degree changes through 0.28 *mm*, 0.46 *mm*, and 0.49 *mm* as the UV light intensity changes through 0.3, 0.4, and 0.5, respectively. These can be represented by the area that the endpoint makes in a reciprocating path. The larger the area gets, the z-direction pushing degree and the avoidance range increase. The area of the endpoint changes through 1.499 mm^2, 2.674 mm^2, and 4.146 mm^2 as the UV light intensity increases through 0.3, 0.4, and 0.5, respectively. The area of the endpoint is influenced by the UV light intensity and the size of the PRP operator.

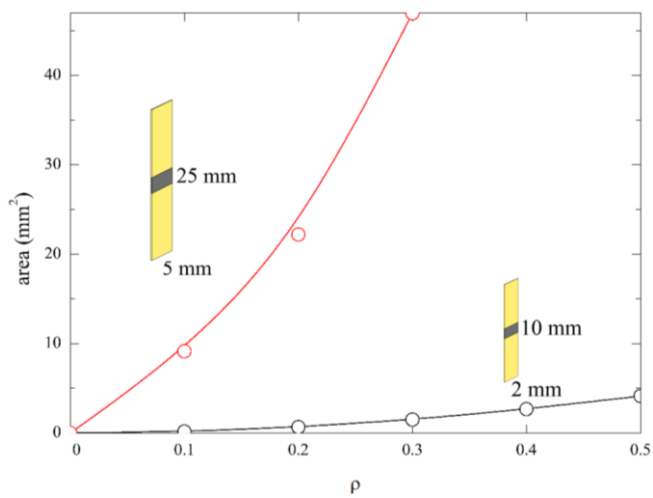

Figure A.8 Prediction of the avoidable area versus the UV light intensity for two sizes of the PRP operator (10 *mm* × 2 *mm* and 25 *mm* × 5 *mm*).

The avoidable area versus UV light intensity is predicted in Fig. A.8 for two sizes of the PRP operator (10 *mm* × 2 *mm* and 25 *mm* × 5 *mm*). The avoidable area can be calculated using three factors: the UV light intensity, the thickness, and the size of the PRP operator. The size of the operator and the UV light intensity are designed by the shape and size of the object. As the thickness increases, the strength of the operator increases, but its reaction rate slows. The thickness is chosen to be thin to enhance the reaction rate. Similarly, as the UV light intensity increases, the operator reacts significantly. The excessive light intensity can destroy the nanostructures of the PRP operator. All these data can be predicted by the FE simulation. In sum, the size of the PRP operator can be determined by the size of the obstacle that must be avoided. Next, the UV light intensity is determined to control how much the operator must be bent. Finally, the path of the endpoint is determined to use the correct PRP operator for the movement of the obstacle.

A basic movement of the PRP operator for gear rotation is shown in Fig. A.9. The initial state of the rotation is shown in Fig. A.9(a). The endpoint is located between the gear teeth, which represents a state to prepare for gear rotation. Figure A.9(b) shows the gear rotation state by pushing the gear teeth in the desired direction. The rotation is available by the basic bending motion. The obstacle avoidance state is shown in Fig. A.9(c), which is the key motion of the process. Details regarding obstacle avoidance are found in Figs. A.5–7. By utilizing the obstacle avoidance state, the gear can return to the initial state without rotating the gear in the opposite direction.

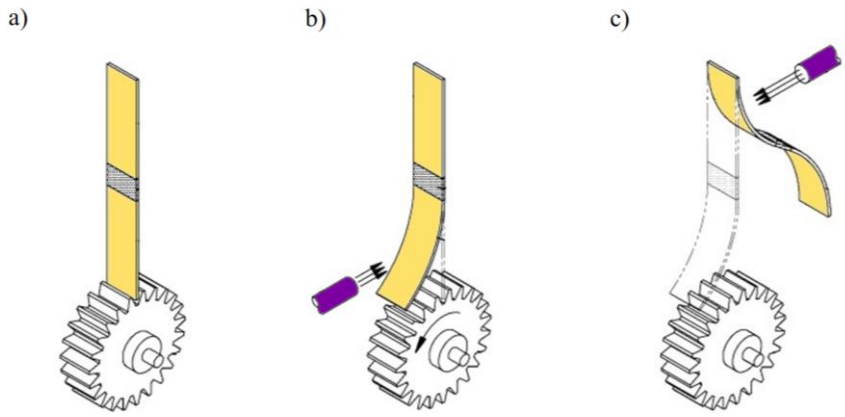

Figure A.9 A basic movement of the PRP operator for gear rotation: (a) initial state, (b) gear rotation state, and (c) obstacle avoidance state.

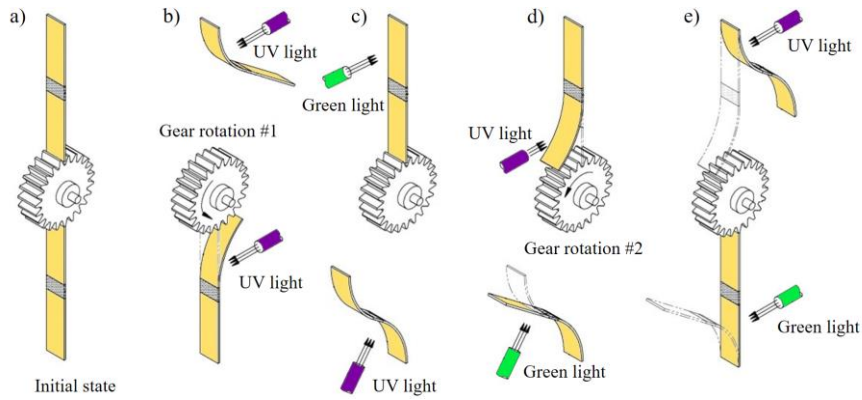

Figure A.10 Detailed movement of the PRP operator for gear rotation.

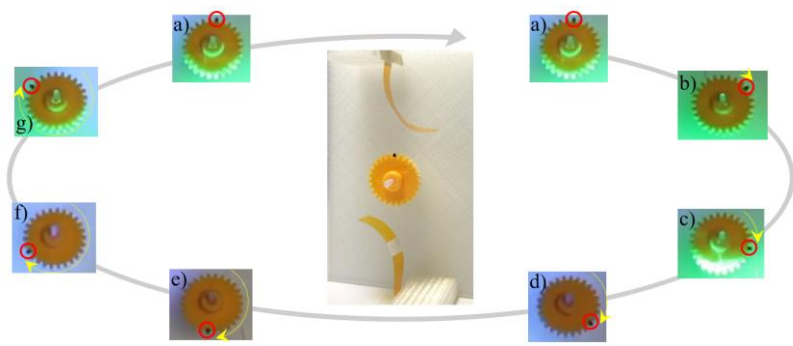

Figure A.11 Photos of the gear rotation with a speed of 0.176 *rpm* (340 *s*/*cycle*).

Two cantilevered PRP operators are installed on the top and bottom of the gear to rotate the gear efficiently, which is shown in the center of Fig. A.11. The PRP operator installed on the top rotates the gear first in Fig. A.10(b) (or Fig. A.11(b)) with UV light, as shown in Fig. A.10(b). The operator on the bottom rotates the gear once again by UV light in Fig. A.10(d) (or Fig. A.11(d)), while the operator on the top returns to its initial state in Fig. A.10(d) (or A.11(d)). The operating and initializing processes interact alternately by the cantilevered PRP operators on the top and bottom. While returning to the initial state, the obstacle avoidance state is used. To minimize the operating time, another operator actuates the gear while the original operator takes time to avoid contacting the gear and returns to its initial state again and vice versa. Figure A.11 summarizes the experimental gear rotation. The black dot in the red circle shows the rotation of the gear. It is necessary to push four times on the top and four times on the bottom for one *cycle*. It takes 340 *s* to rotate a *cycle*, and the speed of rotation is 0.176 *rpm*. By applying the PRP operator to the gear rotator, gears can rotate using UV light and green light. If two more PRP operators are placed on the right and left sides, the rotation speed increases.

The second application is a walking device using a double joint structure. The doubled joint structure is classified into two parts: a regular joint opaque part in the middle and a foot joint opaque part near the edge. The opaque joint part in the middle was previously employed to operate a separation motion. As shown in Fig. 12(a), another opaque joint part near the edge is employed to adjust the friction, inspired from the feet of a human body. When the soles of the feet are attached to the ground, the frictional force of the feet increases to a high friction mode. When the heel is lifted, the friction decreases to a low friction mode. The PRP operator can push itself by supporting specific legs through the adjustment of the friction

force. These high and low friction modes are displayed in Figs. A.12(b) and (c), respectively. A view of the three-legged walking device, composed of three PRP operators, is shown in Fig. A.12(d). As seen, two PRP operators, as the front legs of the device, are located to allow a balanced walk. The rear leg plays a role in pushing the device by stretching the operator.

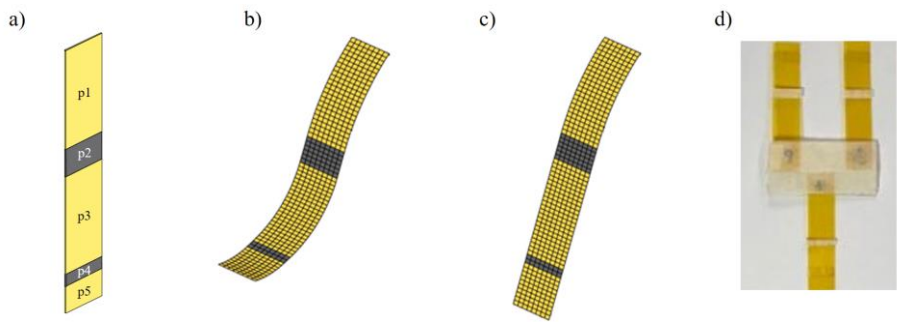

Figure A.12 (a) Double joint structure. (b) High friction mode. (c) Low friction mode. (d) Three-legged walking device.

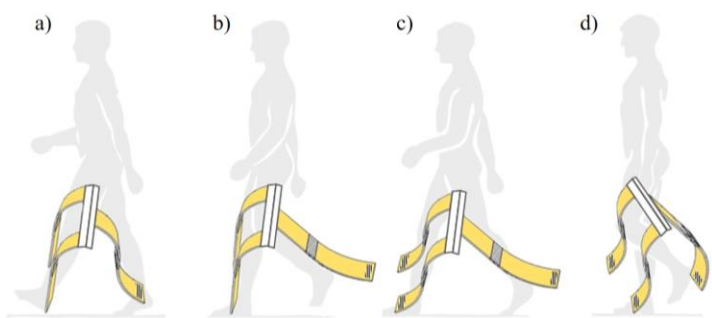

Figure A.13 Three-legged walking mechanism.

A walking mechanism is demonstrated in Fig. A.13, which is similar to the human walking process. The device with three legs is walking by UV light and green light, without any contact with the walking device. As mentioned earlier, the joint structure near the edge was designed to adjust friction and support the device effectively in the high friction mode (Fig. A.12(b)) or to move the device in the desired direction in the low friction mode (Fig. A.12(c)). The walking mechanism mimics the human walking process, like pushing the body forward (Fig. A.13(b)). Unlike ordinary human walking, we tried to simulate the process of pushing one foot from the back and pulling the other foot from the front. We focused on ideas to move forward through the process. The first idea is to concentrate the weight on the rear foot and push the front foot forward. The other idea is to move the concentrated weight to the front foot and pull the rear foot. Other motions would be an intermediate stage to switch these actions. The idea of concentrating and moving the weight of the human body is replaced by controlling the friction force of each foot (Figs. A.12(b) and (c)). Figure A.13(a) shows the state where the front legs get ready to slide while the rear leg gets ready to push. Figure A.13(b) represents the state where the device moves forward after getting ready to slide. As an intermediate stage, the front feet have to increase the friction force of themselves to pull the rear leg to the front, as shown in Fig. A.13(c).

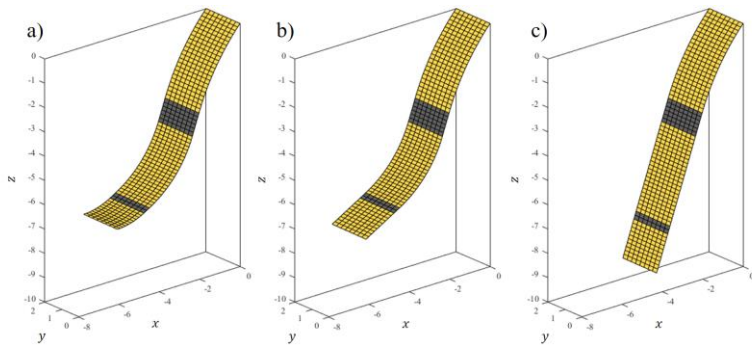

Figure A.14 Movement of the front leg.

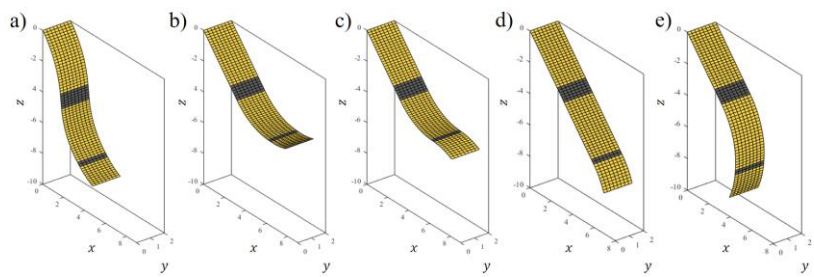

Figure A.15 Movement of the rear leg.

The original idea of the walking mechanism was intended to predict the movement through FE analysis. The movement of the front leg is shown in Fig. A.14, and the movement of the rear leg in Fig. A.15. As seen, the movement of the front leg is slightly different from that of the rear leg. By adjusting the friction, the high friction mode is well predicted and supports the device effectively (Fig. A.14). The low friction mode moves the device in the desired direction (Fig. A.15). In the initial state of walking, part 5 (p5) needs to be in the high friction mode to stay in a steady-state (Figs. A.14(a) and A.15(a)). The front leg must change its shape in the low friction mode by initializing p5 and p3 one by one, to push the device forward, as seen in Figs. A.14(b) and A.14(c), respectively. This pre-pushing step is demonstrated in Fig. A.13(a). After setting the front leg in the low friction mode,

the rear leg pushes the body forward by initializing p1. The three-legged device can be pushed forward by stretching p1 of the rear leg via its high friction mode on the foot of the rear leg and the low friction mode on the feet of the front legs.

The device has to hold the position of the rear foot in the high friction mode and stretch the rear leg to push the body forward. The rear leg has to be shrunk while the front feet hold their position to move forward properly. The front leg must change its state to the high friction mode to hold the position of the front feet. The front leg can change its state from Fig. A.14(c) to Fig. A.14(a). The front leg is then holding its position in the high friction mode. The rear leg must be shrunk in the forward direction to pull the body forward correctly. This process operates step-by-step, by bending p1, p3, and p5 of the rear leg. The high friction mode of the rear foot can change to the low friction mode through Fig. A.15(b) to Fig. A.15(d). P1 and p3 would then shrink as in Fig. A.13(d).

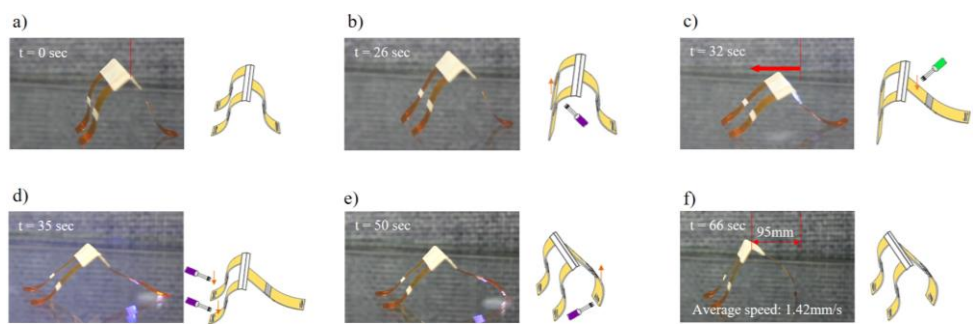

Figure A.16 Photos of the three-legged walking device. The average walking speed is 1.42 $mm \cdot s^{-1}$.

Photos of the three-legged walking device are shown in Fig. A.16, where the PRP operators (25 *mm* × 5 *mm*) are employed. The initial state is shown in Fig. A.16(a). All feet are in the high friction mode for standing in a stable state. The front legs change their positions to the low friction mode to prepare to move forward (Fig. A.16(b)). In Fig. A.16(c), the front legs slide in the moving direction while the rear leg is holding itself in the high friction mode. After stretching the body, the front legs change to the high friction mode, and the rear leg returns to the low friction mode in Figs. A.16(d) and (e). The next step is pulling the rear leg in the forward direction. The walking device eventually returns to its initial state and prepares to repeat walking in Fig. A.16(f). The walking distance for one *cycle* is 95 *mm*. The average walking speed is 1.42 $mm \cdot s^{-1}$. The present three-legged walking device can be used in various applications by improving its stability and by adding more legs.

A.6 Summary of Appendix A

In this study, the behaviors of self-deforming PRPs were explored through multiscale simulations and structural designs. We designed an anti-obstructing motion in the PRP operator based on a nonlinear co-rotational finite element model. The azobenzene-incorporated polymer is a promising material to make remotely controllable deformations. The Azo-LCP of the PRP operator reacted with UV light so that the PRP operator bent toward the irradiated light. The self-deforming PRPs have a non-contact repeatable bending behavior based on their position when specific wavelengths of light were irradiated. It is impossible to return to the initial state through different paths because the PRP moves periodically in the same path

in a repeated, simple bending behavior. We proposed a design for an anti-obstructing motion that could not be designed based on the existing simple bending behavior. By attaching an opaque part into the PRP operator as a joint structure, the PRP operator was able to operate independently due to this opaque part. The nonlinear FE model was constructed to move independently in specified directions through the bending behavior of the separated parts of the PRP operator. The basic movement was applied to a gear rotation and a quadruped walking robot. The PRP operator can take action on whether to move an object or avoid an obstacle. When avoiding an obstacle, the area of the endpoint of the PRP operator is influenced by the UV light intensity and the size of the PRP operator. The size of the PRP operator can be determined by the size of the object or the obstacle that has to be moved or avoided. In the gear rotation, a single joint structure was applied to the PRP operator to react separately. A simple bending motion was used to rotate the gear in the first step. The anti-obstructing motion was used in the next step when returning to the initial state so that the next movement could start. Gear rotation was possible by applying the joint structure of the PRP operator with UV and green light. In the walking application, a double joint structure was applied. The double joint structure is composed of two parts: a regular joint opaque part in the middle to mimic human legs and a foot joint opaque part near the edge to adjust the friction. By controlling the friction force of the feet, the body could hold its position and push itself in the desired direction. The FEM predictions enabled the design of the details of the walking mechanism. The three-leg device was used for walking with double front legs and a single rear leg. The position of the rear foot was fixed by the high friction mode, and the rear leg was stretched to push the body forward. The rear leg had to shrink in the forward direction to pull the body forward

correctly. These two applications showed an improvement of the PRP soft robot and a possibility of non-contact soft robotics, employing single and double joint structures in the PRP operators. If the PRP operator has enough strength to support the weight of itself, we expect to implement various applications with a higher number of joint structures. We anticipate adding more advanced applications by using the joint structures of the PRPs.

Bibliography

[1] Mottershead, J. E., and Friswell, M. I., “Model updating in structural dynamics: a survey”, *Journal of Sound Vibration*, Vol. 167, No. 2, 1993, pp. 347-375.

[2] Friswell, M. I., and Penny, J. E. T., “Updating model parameters from frequency domain data via reduced order model”, *Mechanical Systems and Signal Processing*, Vol. 4, No. 5, 1990, pp. 377-391.

[3] Liu, P. L., “Identification and damage detection of trusses using modal data”, *Journal of Structural Engineering*, Vol. 121, No. 4, 1995, pp. 599-608.

[4] Liu, J. J., Ma, C. K., Kung, I. C., and Lin, D. C., “Input force estimation of a cantilever plate by using s system identification technique”, *Computer Methods in Applied Mechanics and Engineering*, Vol. 190, No. 11-12, 2000, pp. 1309-1322.

[5] Stetson, K. A., “Perturbation method of structural design relevant to holographic vibration analysis”, *AIAA Journal*, Vol. 13, No. 4, 1975, pp. 457-459.

[6] Kim, K. O., Anderson, W. J., and Sandstorm, R. E., “Nonlinear inverse perturbation method in dynamic analysis”, *AIAA Journal*, Vol. 21, No. 9, 1983, pp. 1310-1316.

[7] Hoff, C. J., Bernitsas, M. M., Sandstorm, R. E., and Anderson, W. J., “Inverse perturbation method for structural redesign with frequency and mode shape constraints”, *AIAA Journal*, Vol. 22, No. 9, 1984, pp. 1304-1309.

[8] Guyan, R. J., “Reduction of stiffness and mass matrices”, *AIAA Journal*, Vol. 3, No. 2, 1965, p. 380.

[9] O’Callahan, J., “A procedure for an improved reduced system (IRS) Model”, *Proceedings of 7th International Modal Analysis Conference*, Las Vegas, 1989, pp. 17-21.

[10] Friswell, M. I., Garvey, S. D., and Penny, J. E. T., “The convergence of the iterated IRS method”, *Journal of Sound and Vibration*, Vol. 211, No. 1, 1998, pp. 123-132.

[11] Kim, H., and Cho, M., “Two-level scheme for selection of primary degrees of freedom and semi-analytic sensitivity based on the reduced system”, *Computer methods applied mechanics and engineering*, Vol. 195, No. 33-36, 2006, pp. 4244-4268.

[12] Kim, H., and Cho, M., “Improvement of reduction method combined with sub-domain scheme in large-scale problem”, *International Journal for Numerical Methods in Engineering*, Vol. 70, No. 2, 2006, pp. 206-251.

[13] Cho, M., and Kim, H., “Improved semi-analytic sensitivity analysis combined with a higher order approximation scheme in the framework of adjoint variable method”, *Computers and Structures*, Vol. 84, No. 29-30, 2006, pp. 1827-1840.

[14] Kim, H., and Cho, M., “Fast update of elastic body simulation under impact load by efficient reduction method”, *Advanced in Engineering Software*, Vol. 38, No. 3, 2007, pp. 193-211.

[15] Kim, H., and Cho, M., “Sub-domain reduction method in non-matched interface problems”, *Journal of Mechanical Science and Technology*, Vol. 22 (2008) pp. 203-212.

[16] Kim, H., and Cho, M., “Sub-domain optimization of multi-domain structure constructed by reduced system based on the primary degrees of freedom”, *Finite Elements in Analysis and Design*, Vol. 43, No. 11-12, 2007, pp. 912-930.

[17] Cho, M., Baek, S., Kim, H., and Kim, K. O., “Identification of structural systems using an iterative improved method for system reduction”, *AIAA Journal*, Vol. 47, No. 9, 2009, pp. 2255-2259.

[18] Choi, D., Kim, H., and Cho, M., “Iterative method for dynamic condensation combined with substructuring scheme”, *Journal of Sound and Vibration*, Vol. 317, No. 1-2, 2008, pp. 199-218.

[19] Kim, H., Cho, M., Kim, H., and Choi, H., “Efficient construction of a reduced system in multi-domain system with free subdomains”, *Finite Elements in Analysis and Design*, Vol. 47, No. 9, 2011, pp. 1025-1035.

[20] Jeong, J., Baek, S., and Cho, M., “Dynamic condensation in a damped system through rational selection of primary degrees of freedom”, *Journal of Sound and Vibration*, Vol. 331, No. 7, 2012, pp. 1655-1668.

[21] Kim, H., and Cho, M., “Study on the system reduction under the condition of dynamic load”, *Journal of Mechanical Science and Technology*, Vol. 27, No. 1, 2013, pp. 113-124.

[22] Kim, H., Park, S., and Cho, M., “Structural topology optimization based on system condensation”, *Finite Elements in Analysis and Design*, Vol. 92, 2014, pp. 26-35.

[23] Chang, S., Baek, S., Kim, K. O., and Cho, M., “Structural system identification using degree of freedom-based reduction method and hierarchical clustering algorithm”, *Journal of Sound and Vibration*, Vol. 346, 2015, pp. 139-152.

[24] Sung, H., Chang, S., and Cho, M., “Structural system identification via a reduced system and the sensor-location selection method”, *AIAA Journal*, Vol. 57, No. 5, 2019, pp.2100-2108.

[25] Ahmadian, H., Mottershead, J. E., and Friswell, M. I., “Regularization methods for finite element model updating”, *Mechanical Systems and Signal Processing*, Vol. 12, No. 1, 1998, pp. 47–64.

[26] Friswell, M. I., Mottershead, J. E., and Ahmadian, H., “Combining subset selection and parameter constraints in model updating”, *Journal of Vibration and Acoustics*, Vol. 120, No. 4, 1998, pp. 854–859.

[27] Weng, S., Xia, Y., Zhou, X. Q., and Xu, Y. L., “Inverse substructure method for model updating of structures”, *Journal of Sound and Vibration*, Vol. 331, No. 25, 2012, pp. 5449-5468.

[28] Lu, Y., and Tu, Z., “A two-level neural network approach for dynamic FE model updating including damping”, *Journal of Sound and Vibration*, Vol. 275, No. 3-5, 2004, pp. 931-952.

[29] Arora, V., Singh, S. P., and Kundra, T. K., “Finite element model updating with damping identification”, *Journal of Sound and Vibration*, Vol. 324, 2009, pp. 1111-1123.

[30] Boulkaibet, I., Mthembu, L., Marwala, T., Friswell, M. I., and Adhikari, S., “Finite element model updating using Hamiltonian Monte Carlo techniques”, *Inverse Problems in Science and Engineering*, Vol. 25, No. 7, 2016, pp. 1042-1070.

[31] Alvin, K. F., and Park, K. C., “Second-order structural identification procedure via state-space-based system identification”, *AIAA Journal*, Vol. 32, No. 2, 1994, pp. 397-406.

[32] Hajela, P., and Soeiro, F. J., “Structural damage detection based on static and modal analysis”, *AIAA Journal*, Vol. 28, No. 6, 1990, pp. 1110-1115.

[33] Robertson, A. N., Park, K. C., and Alvin, K. F., “Extraction of impulse response data via wavelet transform for structural system identification”, *Journal of Vibration and Acoustics*, Vol. 120, No. 1, 1998, pp. 252-260.

[34] Chen, H., Kurt, M., Lee, Y. S., McFarland, D. M., Bergman, L. A., and Vakakis, A. F., “Experimental system identification of the dynamics of a vibro-impact beam with a view towards structural health monitoring and damage detection”, *Mechanical Systems and Signal Processing*, Vol. 46, No. 1, 2014, pp. 91-113.

[35] Kim, T., and Kim, Y., “Mac-based mode tracking in structural topology optimization”, *Computers and Structures*, Vol. 74, 2000, pp. 375-383.

[36] Pastor, M., Binda, M., and Harcarik, T., “Modal assurance criterion”, *Procedia Engineering*, Vol. 48, 2012, pp. 543-548.

[37] Shan, V. N., and Raymund M., “Analytical selection of masters for the reduced eigenvalue problem”, *International Journal for Numerical Method in Engineering*, Vol. 18, No. 1, 1982, pp. 89-98.

[38] Kim, K. O., and Choi, Y. J., “Energy method for selection of degree of freedom in condensation”, *AIAA Journal*, Vol. 28, No. 7, 2000, pp. 1253-1259.

[39] Kammer, D. C., “Optimal sensor placement for modal identification using system realization methods”, *Journal of Guidance*, Vol. 19, No. 3, 1995, pp. 729-731.

[40] Paz, M., “Dynamic condensation”, *AIAA Journal*, Vol. 22, No. 5, 1984, pp. 724-727.

[41] Miller, C. A., “Dynamic Reduction of Structural Models”, *Journal of Structural Division ASCE*, Vol. 106, 1980, pp. 2097-2108.

[42] Conti, P. A., “Higher Order Generalization of the Guyan Reduction method”, *Proceedings of the 7th International Modal Analysis Conference*, Las Vegas, Nevada, 1989, pp. 529-532.

[43] Gordis, J., “An analysis of the improved reduced system (IRS) model”, *Proceedings of the 10th International Modal Analysis Conference*, San Diego, California, 1992, pp. 471–479.

[44] Kim, K.O., and Kang, M. K., “Convergence Acceleration of iterative Modal Reduction Methods”, *AIAA Journal*, Vol. 39, No.1, 2001, pp.134-140.

[45] Friswell, M. I., Garvey, S. D., and Penny, J. E. T., “Model reduction using dynamic and iterative IRS techniques”, *Journal of Sound and Vibration*, Vol. 186, No. 2, 1995, pp. 311-323.

[46] Xia, Y., and Lin, R., “Improvement on the iterated IRS method for structural eigensolution”, *Journal of Sound and Vibration*, Vol. 270, 2004, pp. 713-727.

[47] Cho, M., and Kim, H., “Element-Based Node Selection Method for Reduction of Eigenvalue Problem”, *AIAA Journal*, Vol. 42, No. 8, 2004, pp. 1677-1684.

[48] Doebling, S. W., Farrar, C. R., Prime, M. B., and Shevitz, D. W., “Damage identification and health monitoring of structural and mechanical systems from changes in their vibration characteristics: A literature review”, *National Report LA-13070-MS*, Los Alamos National Laboratory, Vol. 30, 1996, pp. 1-127.

[49] Ni, Y. Q., Xia, Y., Liao, W. Y., and Ko, J. M., “Technology innovation in developing the structural health monitoring system for Guangzhou New TV Tower”, *Structural Control & Health Monitoring*, Vol. 26, 2009, pp. 73-83.

[50] Zhan, J. W., Xia, H., Chen, S. Y., and Roeck, G. D., "Structural damage identification for railway bridges based on train-induced bridge responses and sensitivity analysis", *Journal of Sound and Vibration*, Vol. 330, 2011, pp. 757-770.

[51] Worden, K., Manson, G., and Allman, D., "Experimental validation of a structural health monitoring methodology: Part I. Novelty detection on a laboratory structure", *Journal of Sound and Vibration*, Vol. 230, No. 2, 2000, pp. 357-378.

[52] Friswell, M. I., Penny, J. E. T., and Garvey, S. D., "Parameter subset selection in damage location", *Inverse Problems in Engineering*, Vol. 5, No. 3, 1997, pp. 189-215.

[53] Penny, J. E. T., Friswell, M. I., and Garvey, S. D., "Automatic choice of measurement locations for dynamic testing", *AIAA Journal*, Vol. 32, No. 2, 1994, pp. 407–414.

[54] Kim, K. O., Cho, J. Y., and Choi, Y. J., "Direct approach in inverse problems for dynamic systems", *AIAA Journal*, Vol. 42, No. 8, 2004, pp. 1698-1704.

[55] Juneja, V., Haftka, R. T., and Cudney, H., "Damage detection and damage detectability-analysis and experiments", *Journal of Aerospace Engineering*, Vol. 10, No. 4, 1997, pp. 135-142.

[56] Gul, M., and Catbas, F. N., "Identification of structural changes by using statistical pattern recognition", *The 6th International Workshop on Structural Health Monitoring*, Stanford, California, 2007, pp. 11-13.

[57] Catbas, F. N., Gul, M., Zaurin, R., Terrell, T., Dere, Y., Marcus, A. H., Dan, F. M., and Grimmelsman, K. A., "Structural Health Monitoring of Bridges: Fundamentals, Application Case Study, and Organizational Considerations",

Don't Mess with Structural Engineers ASCE, Vol. 330, No. 4, 2009, pp. 757-770.

[58] Woodbury, M. A., "Inverting modified matrices", *Statistical Research Group*, Princeton University, Princeton, New Jersey, No. 42, 1950, pp. 1-4.

[59] Ward, J. H., "Hierarchical grouping to optimize an objective function", *Journal of the American Statistical Association*, Vol. 58, 1963, pp. 236-244.

[60] Murtagh, F., and Legendre, P., "Ward's hierarchical agglomerative clustering method: Which Algorithms Implement Ward's Criterion?", *Journal of Classification*, Vol. 31, 2014, pp. 274-295.

[61] Zhang, G., Ma, J., Chen, Z., and Wang, R., "Automated eigensystem realization algorithm for operational modal analysis", *Journal of Sound and Vibration*, Vol. 333, No. 15, 2014, pp. 3550-3563.

[62] Cheng, W., Lee, S., Zhang, Z., and He, Z., "Independent component analysis-based source number estimation and its comparison for mechanical systems", *Journal of Sound and Vibration*, Vol. 331, No. 23, 2012, pp. 5153-5167.

[63] Cheng, W., Zhang, Z. and He, Z., "Vibration analysis of a submarine model based on an improved ICA approach, advance in neural network research and applications", *Lecture Notes in Electrical Engineering*, Vol. 67, 2010, pp. 721-728.

[64] Cheng, W., Zhang, Z. and He, Z., "Enhance the separation performance of ICA via clustering evaluation and its applications", *Advanced Science Letters*, Vol. 4, 2011, pp.1951-1956.

[65] Sung, H., Chang, S., Cho, M., "Structural system identification using degree of freedom-based reduction method and sensor selection algorithm", *AIAA Model and Simulation Technologies Conference*, No. 0578, 2017, pp. 1-8.

[66] Sung, H., Chang, S., Cho, M., “Experimental Examples for Identification of Structural Systems Using Degree of Freedom-Based Reduction Method”, *Model Validation and Uncertainty Quantification*, Vol. 3, 2017, pp. 375-378.

[67] Sung, H., Chang, S., Cho, M., “Experimental Examples for Identification of Structural Systems Using Neural Network and DOF-Based Reduction Method”, *Structural Health Monitoring, Photogrammetry & DIC*, Vol. 6, 2019, pp.59-62.

[68] Sung, H., Chang, S., Cho, M., “Reduction method based structural model updating method via neural networks”, *AIAA SciTech Forum*, No.1445, 2020, pp.1-10.

[69] Liu, W. K., Karniadakis, G., Tang, S., Yvonnet, J., “A Computational mechanics special issue on: data-driven modeling and simulation—theory, methods, and applications”, *Computational Mechanics*, Vol. 64, 2019, pp.275-277.

[70] Stainier, L., Leygue, A., Ortiz, M., “Model-free data-driven methods in mechanics: material data identification and solvers”, *Computational Mechanics*, Vol. 64, 2019, pp.381-393.

[71] Gantasala, S. Luneno, J.-C., Aidanpää, J.-O., “Investigating how an artificial neural network model can be used to detect added mass on a non-rotating beam using its natural frequencies: a possible application for wind turbine blade ice detection”, *Energies*, Vol. 10, No. 184, 2017, pp.1-21.

[72] Loh, C.-H., Loh, K. J., Yang, Y.-S., Hsiung, W.-Y., Huang, Y.-T., “Vibration-based system identification of wind turbine system”, *Structural Control and Health Monitoring*, Vol. 24, No. 3, 2017, pp.1-19.

[73] Zhang, Y., Miyamori, Y., Mikami, S., Saito, T., “Vibration-based structural state identification by a 1-dimensional convolution neural network”, *Computer-Aided Civil and Infrastructure Engineering*, Vol. 34, No. 9, 2019, pp.822-839.

[74] Atalla, M. J., Inman, D. J., “On model updating using neural networks”, *Mechanical Systems and Signal Processing*, Vol. 12, No. 1, 1998, pp.135-161.

[75] Spear, A. D., Priest, A. R., Veilleux, M. G., Ingraffea, A. R., “Surrogate modeling of high-fidelity fracture simulations for real-time residual-strength predictions”, *AIAA Journal*, Vol. 49, No. 12, 2011, pp.2770-2782.

[76] White, T. J., Broer, D. J., “Programmable and adaptive mechanics with liquid crystal polymer networks and elastomers”, *Nature Materials*, Vol.14, 2015, pp.1087-1098.

[77] Geelhaar, T., Griesar, K., Reckmann, B., “125 Years of liquid crystals-A scientific revolution in the home”, *Angewandte Chemie International Edition*, Vol. 52, 2013, pp.8798−8809.

[78] Li, C., Lo, C.-W., Zhu, D., Li, C., Liu, Y., Jiang, H., “Synthesis of a photoresponsive liquid-crystalline polymer containing azobenzene”, *Macromolecular Rapid Communications*, Vol. 30, 2009, pp.1928−1935.

[79] Yu, Y., Nakano, M., Shishido, A., Shiono, T., Ikeda, T., “Effect of cross-linking density on photoinduced bending behavior of oriented liquid-crystalline network films containing azobenzene”, *Chemical Materials*, Vol. 16, 2004, pp.1637−1643.

[80] Broer, D. J., Mol, G. N., Challa, G., “In-situ photopolymerization of oriented liquid-crystalline acrylates, 5. Influence of the alkylene spacer on the properties of the mesogenic monomers and the formation and properties of oriented polymer networks”, *Makromolekulare Chemie*, Vol. 192, 1991, pp.59−74.

[81] Huang, C., Lv, J.-A., Tian, X., Wang, Y., Liu, J., Yu, Y., “A remotely driven and controlled micro-gripper fabricated from light-induced deformation smart material”, *Smart Materials and Structures*, Vol. 25, 2016, 095009.

[82] Yu, Y., Nakano, M., Ikeda, T., “Direct bending of a polymer film by light”, *Nature*, Vol. 425, 2003, p.145.

[83] Yamada, M., Kondo, M., Mamiya, J.-I., Yu, Y., Kinoshita, M., Barrett, C. J., Ikeda, T., “Photomobile polymer materials: Towards light-driven plastic motors”, *Angewandte Chemie International Edition*, Vol. 47, No. 27, 2008, pp.4986-4988.

[84] Yamada, M., Kondo, M., Miyasato, R., Naka, Y., Mamiya, J.-I., Kinoshita, M., Shishido, A., Yu, Y., Barrettc, C. J., Ikeda, T., “Photomobile polymer materials: various three-dimensional movements”, *Journal of Materials Chemistry*, Vol. 19, No. 1, 2009, pp.60-62.

[85] Liu, D., Bastiaansen, C. W. M., den Toonder, J. M. J., Broer, D. J., "Photo-switchable surface topologies in chiral nematic coatings", *Angewandte Chemie International Edition*, Vol. 51, No. 4, 2011, pp.892-896.

[86] Huang, C., Lv, J.-A., Tian, X., Wang, Y., Yu, Y., Liu, J., "Miniaturized swimming soft robot with complex movement actuated and controlled by remote light signals", *Scientific Reports*, Vol. 5, 2015, 17414.

[87] Song, S.-H., Kim, M.-S., Rodrigue, H., Lee, J.-Y., Shim, J.-E., Kim, M.-C., Chu, W.-S., Ahn, S.-H., "Turtle mimetic soft robot with two swimming gait", *Bioinspiration and Biomimetics*, Vol. 11, 2016, 036010.

[88] Yun, J.-H., Li, C., Chung, H., Choi, J., Cho, M., "Photo deformation in azobenzene liquid-crystal network: Multiscale model prediction and its validation", *Polymer*, Vol. 75, 2015, pp.51-56.

[89] Yun, J.-H., Li, C., Chung, H., Choi, J., Cho, M., "Multiscale modeling and its validation of the trans-cis-trans reorientation-based photodeformation in azobenzene-doped liquid crystal polymer", *International Journals of Solids and Structures*, Vol. 128, 2017, pp.36-49.

[90] Yun, J.-H., Li, C., Chung, H., Choi, J., Cho, M., "Predicting photoisomerization profile of the highly polymerized nematic azobenzene liquid crystal network: First principle calculation", *Chemical Physics Letters*, Vol. 20, No. 627, 2015, pp.20-25.

[91] Choi, J., Chung, H., Yun, J.-H., Cho, M., "Photo-isomerization effect of the azobenzene chain on the opto-mechanical behavior of nematic polymer: A molecular dynamic study", *Applied Physics Letters*, Vol. 105, 2014, 221906.

[92] Choi, J., Chung, H., Yun, J.-H., Cho, M., "Molecular dynamics study on the photothermal actuation of a glassy photoresponsive polymer reinforced with gold nanoparticles with size effect", *ACS Applied Materials and Interfaces*, Vol. 8, No. 36, 2016, pp.24008-24024.

[93] Moon, J., Kim, B., Choi, J., Cho, M., "Multiscale study of the relationship between photoisomerization and mechanical behavior of azo-polymer based on the coarse-grained molecular dynamics simulation", *Macromolecules*, Vol. 52, No. 5, 2019, pp.2033-2049.

[94] Chung, H., Choi, J., Yun, J.-H., Cho, M., “Light and thermal responses of liquid-crystal-network films: A finite element study”, *Physical Review E*, Vol. 91, 2015, 042503.

[95] Chung, H., Yun, J.-H., Choi, J., Cho, M., “Finite-element analysis of the optical-texture-mediated photoresponse in a nematic strip”, *Computational Mechanics*, Vol. 59, No. 1, 2017, pp.147-160.

[96] Chung, H., Choi, J., Yun, J.-H., Cho, M., “Nonlinear photomechanics of nematic networks: upscaling microscopic behaviour to macroscopic deformation”, *Scientific Reports*, Vol. 6, 2016, 20026.

[97] Chung, H., Park, J., Cho, M., “Numerical study of light-induced phase behavior of smectic solids”, *Physical Review E*, Vol. 94, 2016, 042707.

[98] Choi, J., Shin, H., Cho, M., “Multiscale multiphysical analysis of photo-mechanical properties of interphase in light-responsive polymer nanocomposites”, *Composites Science and Technology*, Vol. 160, 2018, pp.32-41.

[99] Moon, J., Shin, H., Baek, K., Choi, J., Cho, M., “Multiscale modeling of photomechanical behavior of photo-responsive nanocomposite with carbon nanotubes”, *Composites Science and Technology*, Vol. 166, 2018, pp.27-35.

[100] Li, C., Yun, J.-H., Kim, H., Cho, M., “Light propagation and photoactuation in densely cross-linked azobenzene-functionalized liquid-crystalline polymers: Contribution of host and concerted isomerism”, *Macromolecules*, Vol. 49, No. 16, 2016, pp.6012-6020.

[101] Li, C., Moon, J., Yun, J.-H., Kim, H., Cho, M., “Influence of external loads on structure and photoactuation in densely crosslinked azo-incorporated liquid crystalline polymers”, *Polymer*, Vol. 129, 2017, pp.252-260.

[102] Lee, Y., Lee, H., Hwang, T., Lee, J.-G., Cho, M., “Sequential folding using light-activated polystyrene sheet”, *Scientific Reports*, Vol. 5, 2015, 16544.

[103] Lee, Y., Moon, J., Choi, J., Cho, M., “Self-folding structural design using multiscale analysis on the light-absorption folding behaviour of polystyrene sheet”, *Scientific Reports*, Vol. 7, 2017, 14277.

[104] Dunn, M. L., “Photomechanics of mono- and polydomain liquid crystal elastomer films”, *Journal of Applied Physics*, Vol. 102, 2007, 013506.

[105] Felippa, C. A., Haugen, B., “A unified formulation of small-strain corotational finite elements: I. Theory”, *Computer Methods in Applied Mechanics and Engineering*, Vol. 194, 2005, pp.2285–2335.

[106] Yang, J. S., Xia, P. Q., “Finite element corotational formulation for geometric nonlinear analysis of thin shells with large rotation and small strain”, *Science China Technological Sciences*, Vol. 55, No. 11, 2012, pp.3142-3152.

[107] Batoz, J.-L., Bathe, K.-J., Ho, L.-W., “A study of three-node triangular plate bending elements”, *International Journal for Numerical Methods in Engineering*, Vol. 15, 1980, pp.1771–1812.

[108] Corbett, D., Warner, M., “Bleaching and stimulated recovery of dyes and of photocantilevers”, *Physical Review E*, Vol. 77, 2008, 051710.

[109] Sung, H., Kim, H., Choi, J., Kim, H., Li, C., Cho, M., “Structural design of soft robotics using a joint structure of photo responsive polymers”, *Smart Materials and Structures*, Vol. 29, No. 5, 2020, 055032.

Abstract in Korean

구조 시스템에 대한 모델 갱신 방법이 다양한 해석에 도입되고 있습니다. 갱신 방법을 개선하려면 프로세스에 정확한 분석과 최소화된 실험적 불확실성이 필요합니다. 유한 요소 모델을 사용하여 구조 시스템을 구현했습니다. 평판 모델의 구조적 진동 거동은 구조의 초기 상태 거동과 그와 관련된 섭동의 조합으로 표현됩니다. 제한된 수의 가능한 위치와 그에 해당하는 자유도에서 얻은 동적 거동은 섭동과 일치하는 구조적 변화를 감지하는 데 사용됩니다. 등가 모델은 측정 및 측정되지 않은 모드 데이터의 관점에서 설명됩니다. 측정되지 않은 정보는 반복적인 개선된 축소 기법을 사용하여 추정됩니다. 시스템 식별 문제는 측정된 정보에 의존하기 때문에 측정된 데이터의 정확도는 식별된 모델의 정확성과 식별 문제의 수렴성을 결정합니다. 시스템 식별의 정확성은 측정 및 센서의 위치에 따라 달라집니다. 최적의 센서 위치를 선정하는 방법을 사용하여, 보다 정확한 식별 방법을 제안합니다. 실험 예제는 시스템 식별의 역 해석 문제에 적용된 제안된 방법의 수렴성과 정확성을 조사하기 위해 선정되었습니다. 실험 데이터를 고려하여 모델의 정확성을 높이려면 모델 갱신 방법이 중요합니다. 여기서 자유도 기반 축소 기법과 역 섭동 방법을 적용하여 구조 시스템 식별을 수행했습니다. 센서 위치 선정 방법을 사용하여 양질의 실험 데이터를 얻을 수 있었습니다. 실험 모델과 해석 모델을 비교하고 갱신하기 위해 실험 데이터와 축소 기법의 변환행렬을 사용하여 전체 유한 요소 모델로 복원되었습니다. 반복적으로 적용되는 개선된 축소 기법은 전체 모델 복원 과정에서 모델의 정확도를 높여줍니다. 그러나 반복 계산으로 인해 시간이 많이 걸립니다. 적합 직교 분해와 함께 반복 계산이 필요 없는 자유도 축소 기법의 변환행렬을 사용하여 계산 효율을 향상시켰습니다. 합성 곱 인공 신경 회로망을 학습하여 모델 갱신 방법에 적용되었습니다. 본 연구를 통해 계산 시간을 줄일 수 있는 합성 곱 인공 신경 회로망을

사용하는 효율적인 모델 갱신 방법의 사용을 제안합니다. 합성 곱 인공 신경 회로망을 사용하는 모델 갱신 방법의 효율성과 정확성을 조사하기 위해 실험 및 수치 예제를 선정하고 검증했습니다. 또한 제안된 방법의 검증을 위해 보다 복잡한 모델이 모델 갱신 방법에 적용되었습니다. 검증된 방법을 볼트 결합 모델링에 도입하고 실험을 통한 모델 갱신으로 더욱 단순화된 모델링을 제안합니다.

주요어: 모델 갱신 기법, 자유도 기반 축소 기법, 시스템 식별, 센서 위치 선정 방법, 인공 신경 회로망

학번: 2014-21558